CANADIAN THESES ON MICROFICHE

THÈSES CANADIENNES SUR MICROFICHE

National Library of Canada
Collections Development Branch

Canadian Theses on
Microfiche Service

Ottawa, Canada
K1A 0N4

Bibliothèque nationale du Canada
Direction du développement des collections

Service des thèses canadiennes
sur microfiche

NOTICE

The quality of this microfiche is heavily dependent upon the quality of the original thesis submitted for microfilming. Every effort has been made to ensure the highest quality of reproduction possible.

If pages are missing, contact the university which granted the degree.

Some pages may have indistinct print especially if the original pages were typed with a poor typewriter ribbon or if the university sent us an inferior photocopy.

Previously copyrighted materials (journal articles, published tests, etc.) are not filmed.

Reproduction in full or in part of this film is governed by the Canadian Copyright Act, R.S.C. 1970, c. C-30. Please read the authorization forms which accompany this thesis.

AVIS

La qualité de cette microfiche dépend grandement de la qualité de la thèse soumise au microfilmage. Nous avons tout fait pour assurer une qualité supérieure de reproduction.

S'il manque des pages, veuillez communiquer avec l'université qui a conféré le grade.

La qualité d'impression de certaines pages peut laisser à désirer, surtout si les pages originales ont été dactylographiées à l'aide d'un ruban usé ou si l'université nous a fait parvenir une photocopie de qualité inférieure.

Les documents qui font déjà l'objet d'un droit d'auteur (articles de revue, examens publiés, etc.) ne sont pas microfilmés.

La reproduction, même partielle, de ce microfilm est soumise à la Loi canadienne sur le droit d'auteur, SRC 1970, c. C-30. Veuillez prendre connaissance des formules d'autorisation qui accompagnent cette thèse.

THIS DISSERTATION
HAS BEEN MICROFILMED
EXACTLY AS RECEIVED

LA THÈSE A ÉTÉ
MICROFILMÉE TELLE QUE
NOUS L'AVONS REÇUE

NL 339 (r. 85/09)

Canada

INVESTIGATION OF SOME CHALCOPYRITE SEMICONDUCTOR ALLOYS

by

MIGUEL A. QUINTERO T.

Thesis

presented to University of Ottawa

in partial fulfillment of the

requirements for the degree of

Doctor of Philosophy

Department of Physics

Faculty of Science and Engineering

University of Ottawa

OTTAWA, ONTARIO, 1985

UNIVERSITÉ D'OTTAWA
UNIVERSITY OF OTTAWA

ABSTRACT

Various chalcopyrite alloy systems of the type $I-III-VI_2:I-III-VI_2$, $I-III-VI_2:2(II-VI)$, $I-III-VI_2:2(MnTe)$ and $I-III-VI_2:2(II-VI):2(MnTe)$ have been investigated and the alloying of II-VI compounds with $I-III-VI_2$ chalcopyrite compounds as well as the introduction of paramagnetic manganese ions into these $I-III-VI_2$ has been studied. Crystallographic, optical and magnetic properties of these materials have been investigated.

X-ray powder photographs were taken for the alloys to indicate equilibrium conditions and values of lattice parameters determined for each case. These were plotted as a function of composition and the range of single phase solid solution thus obtained. In the case of the systems involving manganese, ordering lines were observed in the X-ray photographs and these line indicate that the manganese ions are ordered on the cation sublattice giving a body centered cubic symmetry with a lattice parameter twice that for the zincblende structure (84W1).

Optical absorption measurements were made on single phase polycrystalline samples of these alloys and values of energy gap, E_o, determined. In the case of the chalcopyrite alloy system $CuIn(S_x Se_y Te_z)_2$, absorption measurements were made at 300K and 70K. For each temperature, the variation of E_o was fitted to a power series in x and z (x+y+z=1) and hence contours of constant E_o plotted. In the case of the manganese alloys, the variation of the fundamental energy

gap E_o with composition shows an interesting behavior as compared with that of other manganese alloys. It appears in the present alloys that the values of E_o extrapolate at z=1.0 to a value different from that of the pseudobinary section Cd_{1-z} Mn_z Te. It is suggested that the difference in these results is due to the ordering of the Mn on the cation sublattice.

Single crystal specimens of the alloy system $CuGa(S_{1-y}$ $Se_y)_2$ were prepared using the iodine vapour transport technique. Measurements of wavelength modulated reflectance (WMR) were made on these samples, and values of the energy gaps E_A, E_B and E_C between the three valence bands and the conduction band were determined. Values of the spin-orbit and crystal field splittings were calculated for each temperature using the Hopfield model (60H1), and these were analyzed in terms of p-d linear hybridization between the p-like valence band and the noble metal d-levels. It was found that the Hopfield model does not apply in the present case, since this analysis gives a negative value for the temperature coefficient β of the ratio c/a, in disagreement with the known positive values from X-ray analysis (79Y1) (80B1). Further analysis of the experimental results was made using a model developed by Yoodee et. al. (84Y1). The resulting variation of the ratio E/M, which determines the fractional d character in the valence band, with composition was explained in terms of atomic energy level differences between anion p states and Cu d levels. It appears that the value of E/M is constant with temperature for alloys with

low values of y. However, for samples with high values of y ($CuGaSe_2$) there is a small variation of E/M with temperature. It was found that the coefficients dE/dT and dM/dT both have negative values.

Low-field measurements of magnetic susceptibility χ have been made as a function of temperature in the range 4-100K on samples of the alloy systems involving manganese. Values of the spin-glass transition temperature, T_g, have been obtained from the cusp in the χ vs. T curves, and these values are analyzed in terms of an empirical equation proposed by Escorne et. al. involving an exchange interaction of the form $J(R_{ij})=J_o \exp(-\alpha R_{ij})$ (81E1). The results suggest that below the nearest neighbour (n.n) percolation limit of 0.18, other interactions than the n.n interaction should be considered. It appears that the exponent α of the Escorne et. al. equation is independent of crystal structure, of Mn concentration, of distribuction of the Mn, of the configuration of the non-magnetic cations and of anion composition. For the random alloys, i.e. samples where the manganese ions are in a random configuration, the exchange parameter J_o seems to depend on the configuration of the non-magnetic cations. In the case of the ordered alloys, for low values of z, J_o appears to depend on the Mn configuration, and for the highest Mn concentrations it is observed that the value of J_o is very close to that given by the random alloys.

ACKNOWLEDGEMENTS

I would like to thank Dr. J. C. Woolley for the opportunity to work with him and for his assistance, encouragement and patience throughout the course of this work. I have benefited from his great competence in the field of semiconductors.

I would like to thank Dr. Gilles Lamarche for his assistance in the magnetic susceptibility measurements, for his great friendship, encouragement and the many discussion with him. I also whish to thank Dr. E. Fortin for his friendship and the discussions.

I wish to thank Dr. A. Manoogian for his assistance in the ESR measurements, eventhough these results are not shown here, also for the discussions.

I also would like to thank Kajornyod Yoodee for his friendship and valuable discussions; Tom Donofrio for his friendship and the discussions of the experimental work.

I wish to thank Prf. Jesus Gonzales for providing some single crystal samples of the $CuIn(S_{1-y}Se_y)_2$; Mr. Javier Ruiz for his assistance in the growth of some of the samples; Mr. Carlos Alarcon for his assistance in the preparation of some of the quartz tubes for the vapour transport experiments.

I would like to thank my wife for her patience, for entering some of the data in the computer and for typing some of the thesis.

Finally, I would like to thank University of Los Andes for financial support.

TABLE OF CONTENTS

LIST OF FIGURES

$Cd_{2x}(CuIn)_y Mn_{2z} Te_2$ and $Cd_{2x}(AgIn)_y Mn_{2z} Te_2$. The dash-dotted line is an effective line which represents the values for the section y=0, i.e. $Cd_{1-z}Mn_z Te$.

LIST OF TABLES

CHAPTER I

GENERAL INTRODUCTION AND ARRANGEMENT

I-1 GENERAL INTRODUCTION

Semiconductor research was started in the 1940's on group of IV elements such as Si and Ge. These crystallize in the diamond structure which is one of the simplest and most symmetrical arrangements of atoms known in crystallography. In the early 1950's, investigations (52W1) indicated that the III-V compounds are also semiconductors with properties close to the group IV materials. These binary compounds which may be obtained by substituting in the diamond structure the cations into one sublattice, and the anions into another sublattice resulting in two ordered interpenetrating face centered cubic sublattices with tetrahedral coordination and covalent sp^3 hybrid bonds. This is known as the zincblende structure. Many of the II-VI materials also have the same ordered structure.

Further investigation in the field of semiconductors was made by preparing alloy semiconductors such as those of the II-VI and of the III-V compounds.

These alloys semiconductors are of considerable interest for technological uses, since they are essentially designable materials in which the semiconducting properties can be adjusted for a particular application by controlling the alloy composition.

Also, an extension in the search for new semiconductor compounds and alloys was to examine ternary materials exhibiting diamond-like structure, in which there are equal number of cations and anions, and in which the electron to atom ratio is maintained at four. Examples of such materials are the I-III-VI_2 and II-IV-V_2 compounds which crystallize in the chalcopyrite structure (74S1). These semiconductors can be regarded as the ternary analogs of the II-VI and III-V binary compounds respectively, i.e. $CuGaSe_2$ is the ternary analog of ZnSe and $ZnGeP_2$ is the ternary analog of GaP.

The I-III-VI_2 materials are of both academic and technological interest. In the former case, the experimental data may be analyzed using the theoretical models proposed in the literature, and information about the physical properties of the materials may be obtained. In the latter case, the interest lies in increasing the range of applications of opto-electronic and non-linear devices. For example, visible and infrared detectors,

light emitting diodes, solar cells, etc. can be made from these compounds, and by use of alloys, devices may be designed to operate in specified wavelength ranges.

Recently, there has been considerable interest in alloy semiconductors which also show magnetic behavior. These semimagnetic semiconductor alloys (SMSA) can be obtained by the replacement of nonmagnetic ions in a semiconductor material by a magnetic ion such as Mn, Fe, Cr, etc. Most of the work on this type of materials has been carried out on the II-VI compound semiconductors with manganese as the magnetic ion. In this case group II elements are replaced substitutionally by the paramagnetic Mn ions. As a result, an alloy semiconductor with interesting optical and magnetic properties is obtained. The magnetic properties of these SMSA are related to the d-levels occurring in the manganese ions. The random distribution of these manganese spins gives rise to the formation of clusters and spin-glass behavior at low temperature (80G1).

With regard to the I-III-VI_2 chalcopyrite alloys, some investigations have been made on these materials involving trivalent Fe as the magnetic ion. However studies (84Q1) showed that the range of single phase behavior in these alloys is very small. As a consequence

these materials are limited to, at most, several percent of magnetic Fe ions. At the present time, no studies are reported in the literature on $I-III-VI_2$ materials with Mn as the magnetic substitutional ion.

In view of the importance of new alloy semiconductors, indicated above, in the present work a number of semiconductor alloy systems such as $I-III-VI_2$:$I-III-VI_2$ and $I-III-VI_2$:2(II-VI):2(MnTe) were prepared, and some physical properties were measured as a function of composition and temperature.

I-2 ARRANGEMENT OF THE MATERIAL OF THIS THESIS

The work carried out is part of a group program of research into alloy semiconductors, particularly the chalcopyrite materials and semimagnetic alloys. At various places in the thesis, results obtained by other workers in the research group must be quoted where they are relevant to the problems considered here. In every case, the corresponding reference is indicated.

The material of the present thesis is arranged as follows:

Chapter II deals with the crystal and energy band

structures of zincblende and chalcopyrite materials. A description of the two structures will be presented. The energy band structure at the Γ-point of these I-III-VI_2 chalcopyrite crystals as derived from the band structure of the II-VI analogs will be illustrated. The Hopfield model (60H1) and the linear p-d hybridization of these I-III-VI_2 materials will be discussed.

The method of preparation of the specimens used in this work will be given in Chapter III. Section III-1 is concerned with the production of polycrystalline samples. In Section III-2 the experimental details of the preparation of single crystal specimens obtained by using the method of chemical vapor deposition (CVD) will be considered.

In Chapter IV, the x-ray and optical experimental measurements made in this work are described. The main features in the calculation of accurate lattice parameter values by x-ray Powder Photograph are indicated. Optical absorption measurements as well as wavelength modulated reflectance measurements (WMR) are described.

It was indicated previously that these I-III-VI_2 alloys are of academic and technological importance. In particular the pseudobinary alloys systems $CuIn(S_{1-y}Se_y)_2$

and $CuGa(S_{1-y}Se_y)_2$ are of interest as possible materials for solar cell production and improvements in performance can be obtained by addition of some tellurium. Thus Knowledge of the crystallography and energy gap values of the systems $CuIn(S_x Se_y Te_z)_2$ and $CuGa(S_x Se_y Te_z)_2$, with $x+y+z=1$, is required. These systems are dealt with in Chapter V, where the range of single phase behavior, lattice parameter values and optical energy gap values at 300 and 70 K for these chalcopyrite alloys are discussed. The experimental energy gap data obtained are compared with predictions of an interpolation equation suggested by Williams et. al.(78W1).

In Chapter VI, the results of WMR measurements as a function of temperature on the pseudobinary system $CuGa(S_{1-y}Se_y)_2$ will be presented. The variation of the three energy gap values E_A, E_B, E_C as a function of temperature is described. From these experimental data, values of spin-orbit and crystal field splittings of the valence bands for these materials are calculated. These values are analyzed in terms of p-d hybridization. As an extension of the investigation of the valence band of these I-III-VI_2 chalcopyrite materials, an equation very recently developed by Yoodee K. et. al.(84Y1) is given and used in the analysis of the experimental results.

The alloying of II-VI compounds with $I-III-VI_2$ compounds as well as the introduction of the paramagnetic Mn ions in these $I-III-VI_2$ compounds are dealt with in Chapter VII. Samples of the systems $Cd_{2x}(CuIn)_y Mn_{2z} Te_2$ and $Cd_{2x}(AgIn)_y Mn_{2z} Te_2$ were prepared, and ranges of single phase solid solution were determined. The variation of the lattice parameter values as a function of alloy composition is presented. Optical energy gap values at room temperature, in the single phase field, were measured by optical absorption for each of the systems investigated here. X-ray powder photograph and the energy gap results show that there is a partially ordered field in each of these alloy systems, the X-ray powder photographs showing the presence of ordering lines. The energy gap results show an interesting behavior as compared with the usual SMSA such as $Cd_x Zn_y Mn_z Te$ (83B1). It is suggested that the difference in these results is due to the ordering of the Mn on the cation sublattice showing body centered cubic symmetry (84W1).

Finally as described in Chapter VIII, some low field measurements of magnetic susceptibility were made as a function of temperature in the range 4 to 100 K on these $Cd_{2x}(CuIn)_y Mn_{2z} Te_2$ and $Cd_{2x}(AgIn)_y Mn_{2z} Te_2$ SMSA. Values of T_g and θ, the spin-glass temperature and Curie-Weiss constant are presented. The values of T_g are analyzed in

terms of an equation proposed by Escorne et. al.(81E1).

CHAPTER II

CRYSTAL AND BAND STRUCTURES OF ZINCBLENDE AND CHALCOPYRITE MATERIALS

II-1 INTRODUCTION

In this chapter, the crystal structures of zincblende and chalcopyrite materials are discussed. Analysis of the band structures at the Γ-point of the Brillouin zone of these materials are presented. The valence band of the I-III-VI_2 semiconductors is discussed in terms of the Hopfield model and linear p-d hybridization of spin-orbit as well as crystal field splittings.

II-2 CRYSTAL STRUCTURES OF ZINCBLENDE AND CHALCOPYRITE MATERIALS

It was indicated above that the II-VI materials are the closest analogs of the I-III-VI_2 semiconductors. Hence the crystal structures of these materials are expected to be very similar. The crystal structure of the II-VI compounds is derived from the tetrahedrally bonded diamond structure in such a way that one of the fcc

sublattices is occupied by the cations (II), while the other sublattice by the anions (VI) with an average of four valence electrons per site. Figure II-1 shows a perspective drawing of the zincblende structure. The tapered arrows indicate the tetrahedral bonding to the four nearest neighbors. The shaded circles represent atoms of the group (II), and the open circles which are displaced by a vector $a(\hat{i}+\hat{j}+\hat{k})/4$ represent the (VI) atoms. If all the atoms in Fig. II-1 were identical, then the diamond structure would be obtained. Hence the symmetry would be higher and an inversion center between nearest neighbors would appear. Consequently the main difference between these two structures is that the zincblende is composed of two different kind of atoms, and the ordering of the atoms reduces the symmetry with the loss of the inversion center. The point group of these materials will be indicated latter.

In the case of the I-III-IV_2 compounds and alloys, the structure is also adamantine. However because of the ordering of the constituent cations, the unit cell symmetry is no longer cubic as in the above cases. These materials have a body centered tetragonal structure with c/a ratios equal to or a little less than 2. The structure involved is identical with that of $CuFeS_2$, commonly known as chalcopyrite. The unit cell of this structure contains

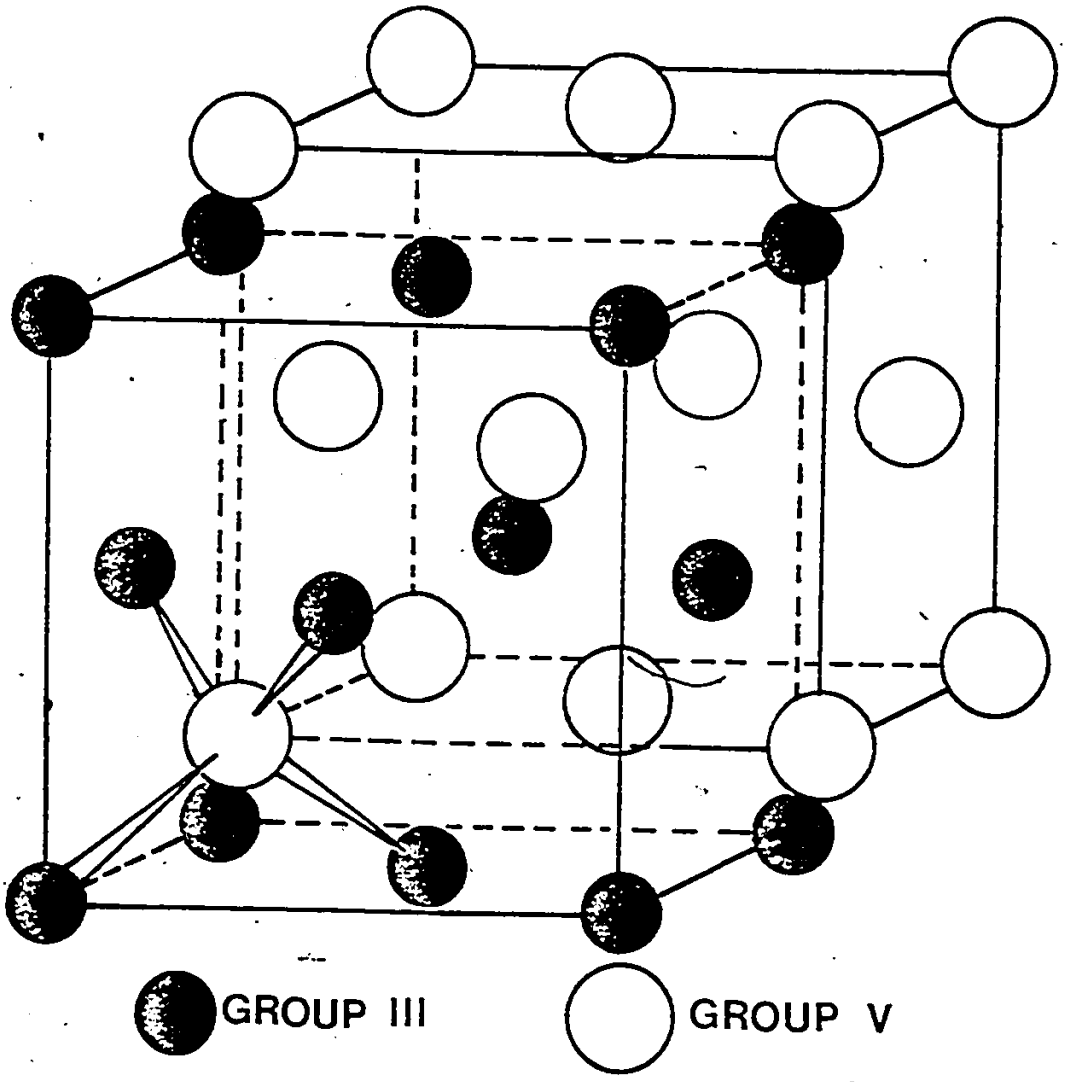

Fig. II-1 Perspective drawing of zincblende structure.

sixteen atoms as compared to eight atoms for the zincblende structure discussed above. Examples of such materials are $CuInS_2$, $CuGaS_2$, $CuInTe_2$, and $AgInTe_2$, etc., which are of direct concern in this thesis.

In the chalcopyrite structure there are two cation sub-lattices, each occupied by one type of cation, and one anion sub-lattice. Figure II-2 shows the planar maps of the lattice sites projected on the c and b faces. The shaded and open circles represent the two cation sub-lattices and the crosses the anion sub-lattice. In this structure each of the (I) and (III) atoms is tetrahedrally coordinated by four (VI) atoms, while each (VI) atom is tetrahedrally coordinated by two I and two III atoms in an ordered manner as is shown in fig. II-3 by the tapered arrows.

Due to the tetragonal compression along the z axis ($c<2a$) and the difference in bond strengths, which shifts the anion sites away from the ideal (1/4,1/4,1/4) and symmetrically related positions towards one of the pairs of cations, there is a noncubic crystalline field of tetragonal symmetry in these chalcopyrite materials (74S1). This noncubic field may affect the band structure of these materials as compared with their zincblende analogs.

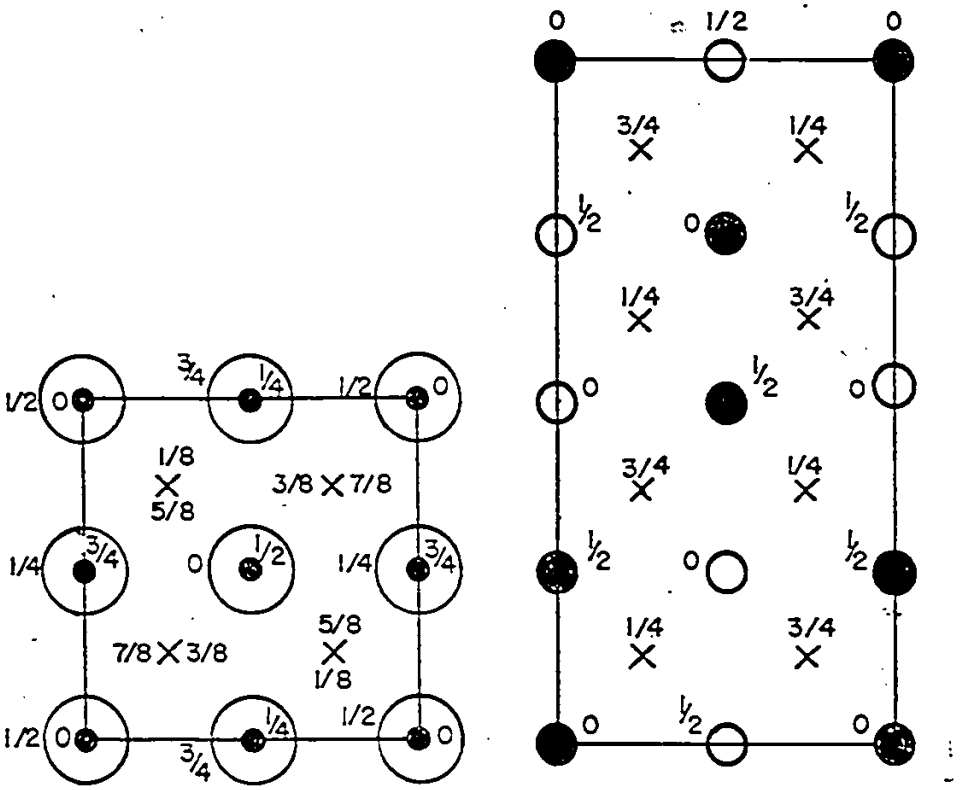

Fig. II-2 Chalcopyrite structure: a) projection of atomic positions on c face. b) projection of atomic positions on b face.

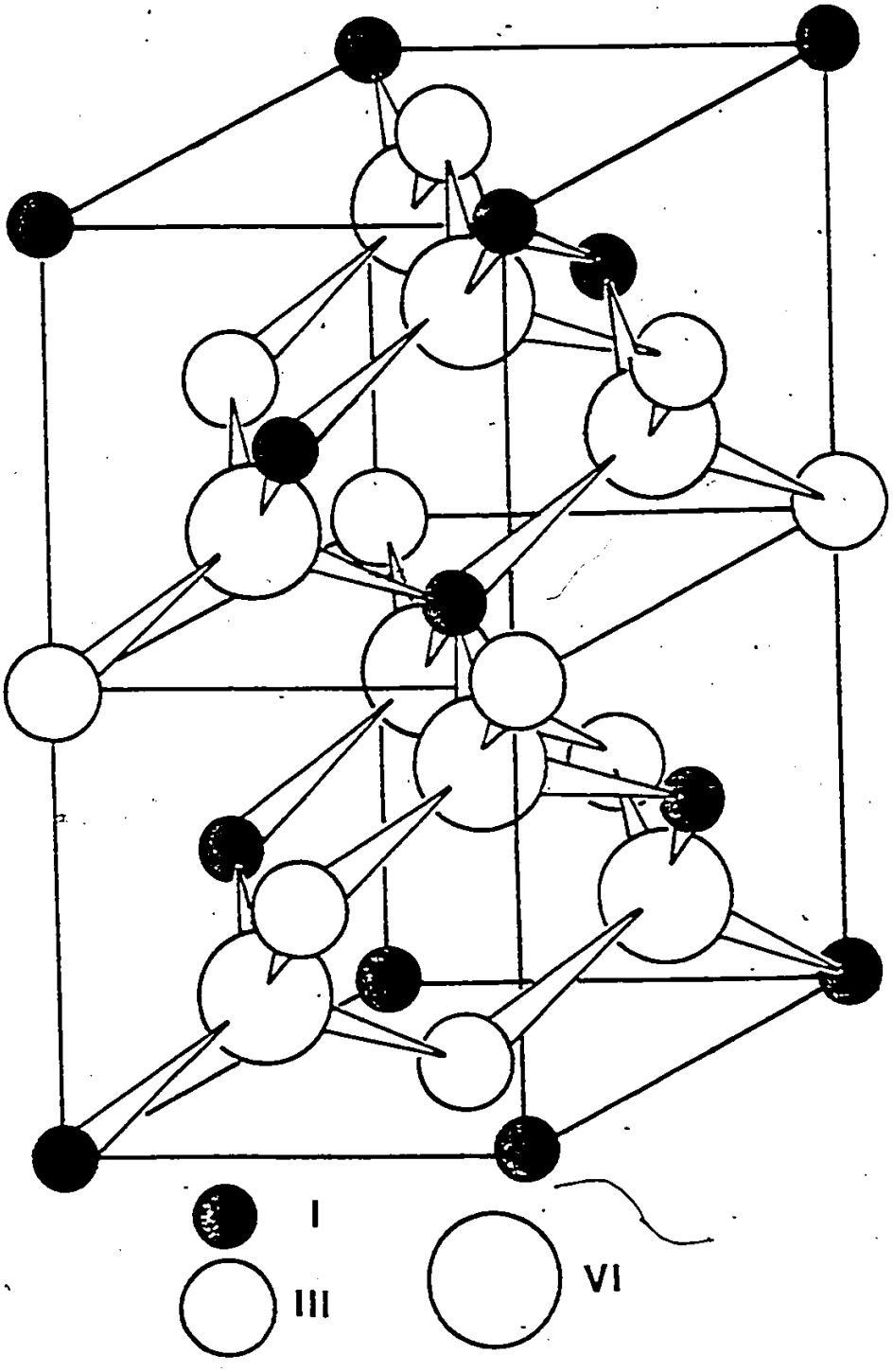

Fig. II-3 Perspective drawing of chalcopyrite structure.

II-3 ENERGY BAND STRUCTURES OF ZINCBLENDE AND CHALCOPYRITE SEMICONDUCTORS

Band structure calculation is an important subject in the field of semiconductor research. Since the full development of this is beyond the scope of the present work, because this thesis is mainly experimental, only some general ideas are presented here. The approach by symmetry considerations of the crystal structure using group theory can give a qualitative idea of the band structure, such as the degeneracy of various energy bands in the vicinity of some symmetry points or along certain symmetry directions in the Brillouin zone. These symmetry considerations will be used in the present section in order to obtain a qualitative understanding of the splitting of the bands and of the selections rules for zincblende and chalcopyrite structures at the Γ-point.

As was mentioned previously, the I-III-VI_2 chalcopyrite semiconductors are the simplest structural analogs of II-VI zincblende materials. It is therefore to be expected that the energy band structure of a chalcopyrite sample is related to that of its binary analog. The concept of a binary-ternary analogy of

electronic properties has been proved to be very useful in understanding the physical properties of these I-III-VI_2 materials.

The simplest approximation to the energy band structure of a chalcopyrite crystal is obtained from the band structure of the zincblende binary analog by comparing the chalcopyrite Brillouin zone with that of the zincblende Brillouin zone. In Fig. (II-4) a comparison of the Brillouin zones for the two structures is shown.

The correspondence between some symmetry points of these Brillouin zones of the two structures can be established by mapping the chalcopyrite Brillouin zone into that of zincblende. This is seen on the sections of the two (embedded) zones on the $k_y - k_z$ plane and on the $k_z - k_{xy}$ plane as is shown in figure (II-5). It can be seen from that figure that the correspondence between the points of high symmetry is:

Zincblende.	Chalcopyrite.
$\Gamma(0,0,0)$, $X(0,0,\frac{2\pi}{a})$, $W(0,\frac{2\pi}{a},\frac{2\pi}{a})$	$\Gamma(0,0,0)$
$L(\frac{\pi}{a},-\frac{\pi}{a},-\frac{\pi}{a})$	$N(\frac{\pi}{a},\frac{\pi}{a},0)$
$X(0,\frac{2\pi}{a},0)$	$T(0,0,\frac{\pi}{a})$

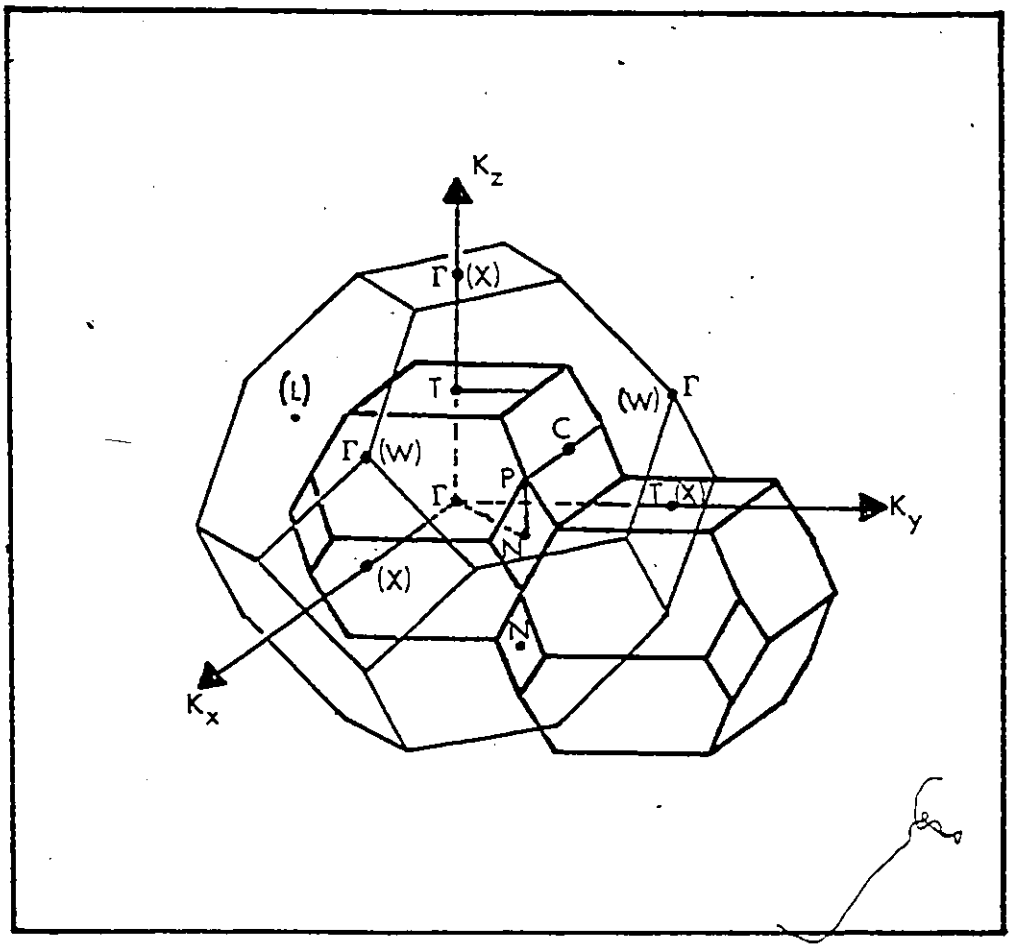

Fig. II-4 Comparison of the Brillouin zones of the zincblende (thin line) and chalcopyrite (thick line) lattices.

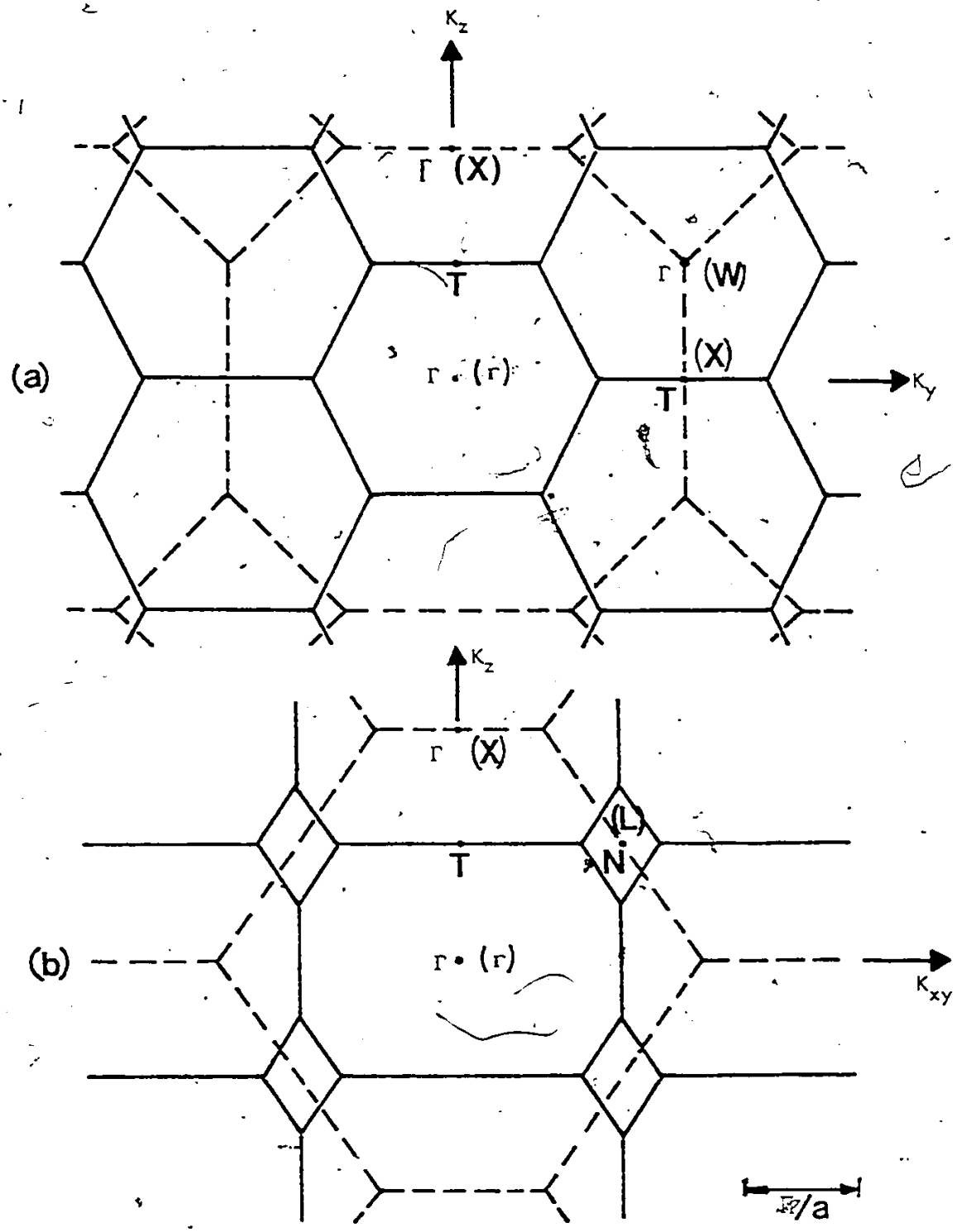

Fig. II-5 Sections of the first Brillouin zones of the chalcopyrite (solid line) and zincblende (dashed line) lattices.

There are two main approaches to the study of the energy band structure of a solid by using group theory. One of them is the empty lattice model, which consist of a fictitious lattice that has the translational periodicity of the actual crystal but in which the periodic potential is vanishingly small. The other one is to follow how the crystal energy levels form as the lattice is constructed by bringing a collection of isolated atoms together taking into account the crystal potential. In the former case information about the band structure along several symmetry directions is obtained, and by knowing the original atomic states the degenerancies and shapes of the empty lattice bands are obtained. In the later case, information about the band structure is obtained mainly at the Γ point in the Brillouin zone. As the present work is concerned with the center of the Brillouin zone of the materials under investigation the second approach will be indicated here.

When a specific crystal structure is formed from the original atomic states, such as s, p or d levels, the group of full rotations of the free atoms is restricted to the symmetry operations of the group of the crystal structure concerned. This means that the atoms or ions which build up the material are under the action of the crystal field and spin-orbit interactions in the

structure. Thus, the splittings of the energy bands due to the crystal field and spin-orbit interactions near to a point of high symmetry in the Brillouin zone of a material can be obtained.

With regard to the materials under investigation, it was indicated above that these crystallize in the zincblende and chalcopyrite structures. The bands of most zincblende materials are composed of s and p-like orbitals (sp^3 hybridization). The band structure at the Γ-point of a chalcopyrite material may be derived from the zincblende binary analog. It can be shown that in absence of spin-orbit interaction, in a zincblende material, the s and p states have Γ_1(s) and Γ_{15}(p) symmetries which form the conduction and valence bands respectively of these materials. The Γ_1 (s) band is singly degenerate and the Γ_{15} (p) band is triply degenerate. When the tetragonal crystal field of chalcopyrite is applied to the triply degenerate Γ_{15}(p) valence band of zincblende, the result is a non-degenerate band of Γ_4 (z) symmetry and a doubly degenerate band of Γ_5 (x,y) symmetry. The inclusion of spin-orbit effects changes the symmetry of the Γ_4 band to one of Γ_7 and lifts the degeneracy of the Γ_5, resulting in bands of Γ_6 and Γ_7 symmetry. The Γ_6 conduction band of chalcopyrite corresponds to the Γ_1 band of zincblende. This is illustrated in fig.(II-6) where the selection rules for

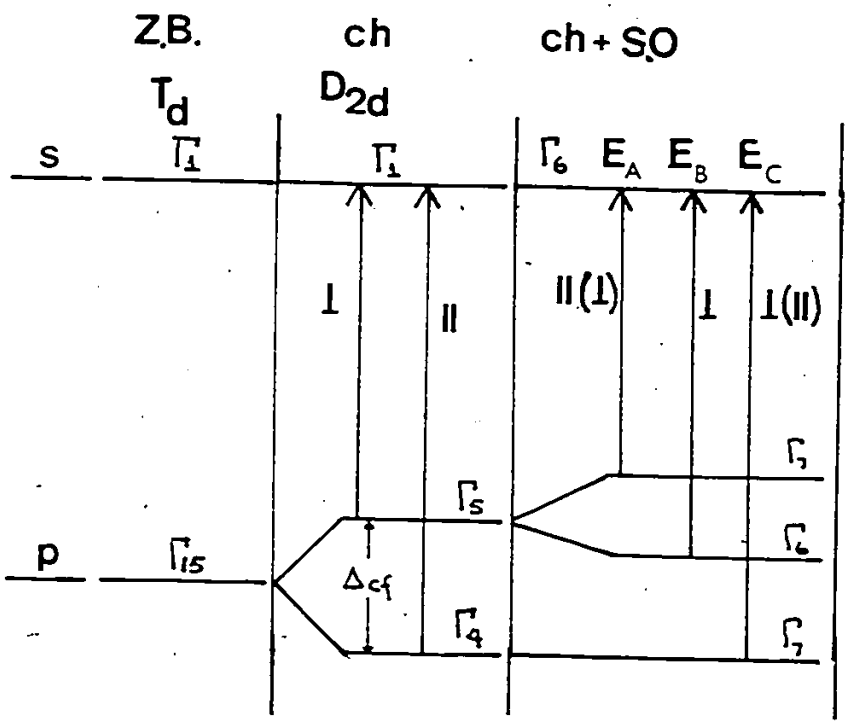

Fig. II-6 Band structure and selection rules for the transitions in a chalcopyrite material derived from the Γ_{15} ----> Γ_1 energy gap in a zincblende crystal.

dipole transitions are also indicated.

The values of the the three transitions E_A, E_B and E_C observed in these noncubic materials, such as I-III-VI_2 and II-IV-V_2 compounds, have been analyzed using Hopfield's quasi-cubic model for a p-like valence band(60H1).

The quasi-cubic model was originally proposed by Hopfield to explain the observed splitting of the valence band in compounds such as ZnO, CdS and ZnS. The model suggests that the splitting is due to two contributions. The first is a small amount of spin-orbit coupling (such that the spin-orbit splitting is small compared with Eg) which mixes the p valence bands. The second is a small strain occurring in the crystal in the z-direction, this being the largest contribution to the crystal field splitting of the valence band and the result is a shift in the energy of the p_z states from that of the p_x and p_y states. The eigenvalues of the resulting Hamiltonian yield values of spin-orbit and crystal field splittings which are represented by the following equations,

$$\Delta_{so}=-1/2(E_1 + E_2) + 1/2[(E_1 + E_2)^2 - 6E_2E_1]^{\frac{1}{2}} \quad \text{(II-1)}$$

and

$$\Delta_{cf}=-1/2(E_1 + E_2) - 1/2[(E_1 + E_2)^2 - 6E_1E_2]^{\frac{1}{2}} \quad \text{(II-2)}$$

where Δ_{cf} is the Γ_4 to Γ_5 spacing due to crystal field effects in the absence of spin-orbit interaction, fig.(II-6), and Δ_{so} is the corresponding splitting of the valence band due to spin-orbit interaction in the absence of crystal field effects. For materials having wurtzite structure E_1 and E_2 are the energies of the Γ_7 valence band relative to the Γ_9 valence band. In the case of CdS very good agreement was found between the experimental data and the predictions of the model. However, the model was only qualitatively successful in the case of ZnO.

Rowe and Shay (71R1) extended the quasi-cubic model to ternary chalcopyrite materials. In this case, E_1 and E_2 of the above equations are the energies of the Γ_7 valence bands relative to the Γ_6 valence band. The model gives an adequate description of the valence bands of the II-IV-V_2 compounds, which are simply related to the corresponding bands in their III-V analogs. However, in the case of the I-III-VI_2 the contributions from the d-levels have to be considered.

Two effects of the hybridization of anion p-levels and noble metal d-levels have been observed. The direct energy gaps measured in I-III-VI_2 materials are smaller than the energy gaps in their II-VI analogs by about 1.0

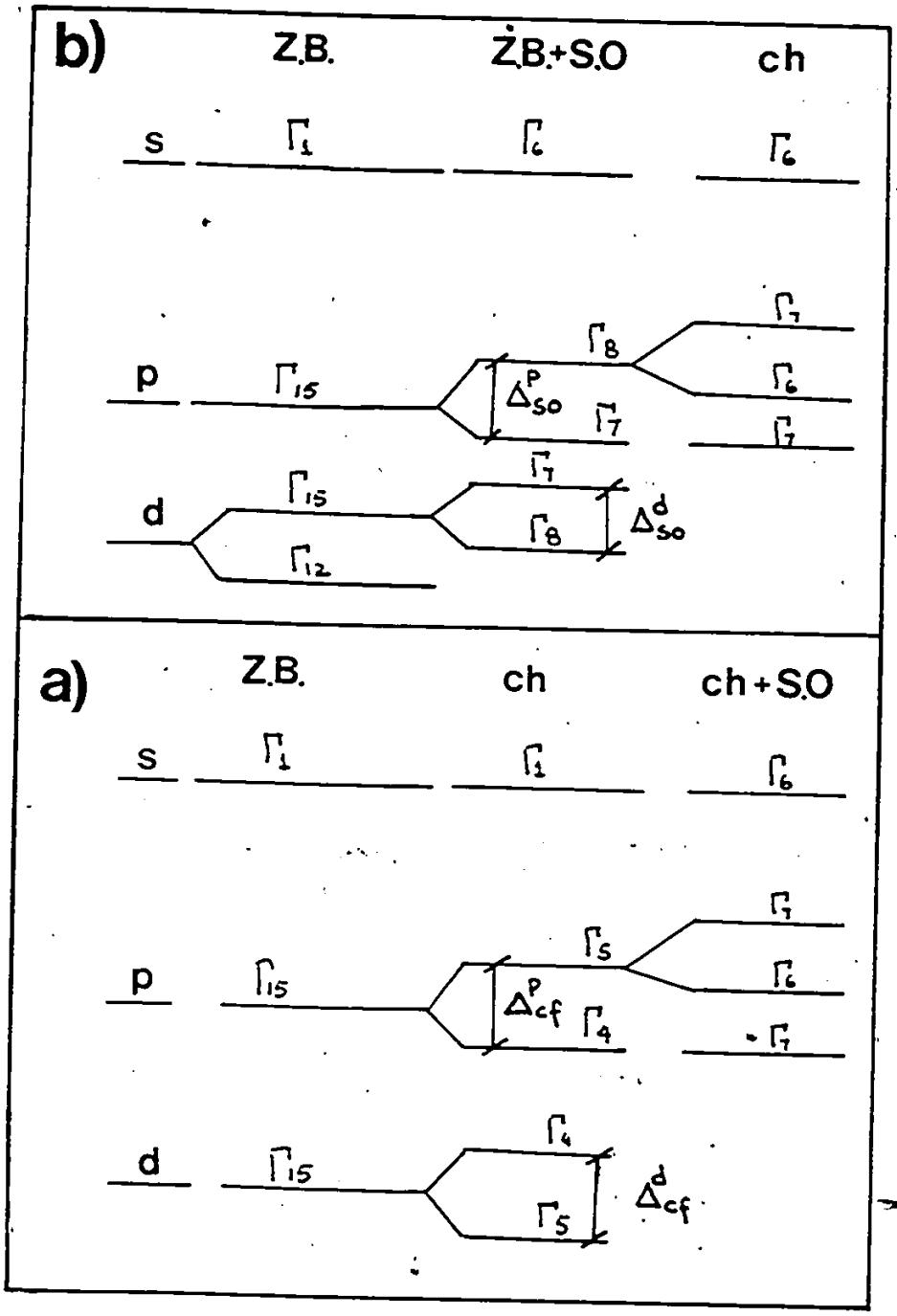

Fig. II-7 Band structure of a chalcopyrite crystal derived from the Γ_{15}(p) and Γ_{15}(d) bands of a zincblende material, the Γ_{12} (d) band having been neglected. In a), the crystal field interaction due to the chalcopyrite crystal is applied first followed by the spin-orbit effect. In b), the spin-orbit effect is applied first and the crystal field effect is applied afterwards.

eV (in the case of $CuGaSe_2$), and the spin-orbit splittings are considerably smaller than those of their II-VI analogs (74S1). Also, X-ray photoemission studies (73L1) (74K1) have shown strong p-d hybridization of the valence bands, with stronger p-d interaction in the case of Cu-III-VI_2 than in the Ag compounds.

The effects from d-levels have been taken into account by using the concept of linear p-d hybridization in these materials (77Y1) (82L1). Thus as has been indicated previously (82L1), if α is the fractional p character in the valence band and $(1-\alpha)$ the fractional d character, it has been assumed that the values of Δ_{so} and Δ_{cf} can be written as a linear sum of p and d contributions in the form

$$\Delta_{so} = \alpha \Delta^{p}_{so} + (1-\alpha) \Delta^{d}_{so} \qquad \text{(II-3)}$$

$$\Delta_{cf} = \alpha \Delta^{p}_{cf} + (1-\alpha) \Delta^{d}_{cf} \qquad \text{(II-4)}$$

where Δ^{p}_{so}, Δ^{d}_{so}, Δ^{p}_{cf}, and Δ^{d}_{cf} are the spin-orbit and crystal field splittings of the p and d levels respectively. These parameters are illustrated in fig. (II-7a,b), where in fig. (II-7a) the crystal field interaction has been turned on before the crystal field interaction, while in fig. (II-7b) the spin-orbit interaction has been applied first.

It has been indicated (82L1) that the crystal field Δ^{p}_{cf} and Δ^{d}_{cf} are related to the lattice parameter ratio c/a in the form

$$\Delta^{p}_{cf} = 3b_{p}(2-c/a)/2 \qquad \text{(II-5)}$$

$$\Delta^{d}_{cf} = 3b_{d}(2-c/a)/2 \qquad \text{(II-6)}$$

where b_{p} and b_{d} are the deformation potentials associated with the p and d orbitals respectively, and (2-c/a) is the tetragonal distortion.

The above results will be used to analyze the energy gap data as a function of temperature in chapter VI. Thus, values of the spin-orbit and crystal field splittings obtained using the quasi-cubic Hopfield's model are analyzed in terms of contributions from d-orbitals of the noble metal to the valence band.

With regard to recent theoretical calculations of the valence band of these I-III-VI_2 materials, K. Yoodee, J. C. Woolley and V. Sa-yakanit (84Y1) have proposed a model which includes the effects of the p-d hybridization in the Hamiltonian of the system. They have applied the model to a large number of I-III-VI_2 compounds and it was found that a dimensionless parameter E/M is a measurement of the fractional d character in the valence band of these

materials. This recently proposed model will be discussed and used to analyze the experimental results in chapter VI.

CHAPTER III

GROWTH OF SAMPLES

III-1 PREPARATION OF POLYCRYSTALLINE SAMPLES

The method of preparation of the polycrystalline samples used in this thesis was the same that used by Woolley et. al (66W1). The components of 1 gram samples were sealed in small segments of quartz tubing under vacuum. Care was taken to minimize the length of the sealed ampule in order to eliminate losses up the sides of the tube. The ampules were placed in a melting furnace and heated to 1150 °C at an average rate of about 200°C per hour. They were left at that temperature for 1 to 2 hours, during which time the tubes were shaken periodically in order to ensure good mixing of the components. The furnace was then turned off and the samples left to cool to room temperature in approximately 5 hours. This rate was sufficiently slow to avoid breakage of the quartz upon solidification of the alloys. Then, the samples were placed in an annealing furnace. The choice of annealing temperature was guided by the melting point of the compounds involved in the several systems investigated. The annealing temperatures used in this work will be given for each of the alloy system prepared.

For samples including manganese, it was found necessary to carbonize the quartz tubes in order to prevent the manganese attacking the quartz at high temperature. This was accomplished by using the following process. A piece of absorbent paper was impregnated with acetone and inserted into the open end of a quartz tube whose other end had been previously sealed. Then, the sealed end was heated over an open flame. When the concentration of acetone vapor was high enough, a layer of red hot carbon would begin to accumulate at the hot end of the tube. This process was repeated until the carbon layer was sufficiently thick that the tube became opaque under a strong light.

Debye-Scherrer x-ray powder photographs were used to check the homogeneity condition of each sample and to determine whether single phase solid solution was obtained. The films so obtained were used to calculate lattice parameter values for the alloys. This will be discussed in chapter IV.

III-2. CRYSTAL GROWTH

In the present work, it was decided to prepare some single crystal specimens of the pseudobinary section

$CuGa(S_{1-y}Se_y)_2$, for which it is well known that a chalcopyrite single phase occurs at all compositions (75R1). The method of preparation of these crystalline samples was chemical vapor deposition (CVD) with iodine as transport agent (64S1)

In its static form, the method involves a solid-gas reaction with a proper transporting agent such as iodine. This reaction will give rise to the formation of a gaseous phase of limited stability. By applying an adequate temperature gradient in a closed tube these phases can travel from one zone to the other. The form of such a reaction is

Reaction

$$2MX_2(s) + 2I_2(g) \rightleftharpoons 2MI_2(g) + 2X_2(g)$$

Growth

$$2MI_2(g) + 2X_2(g) \rightleftharpoons MI_4(g) + MX_2(s) + X_2(g)$$

where M may be CuIn, CuGa, AgIn, etc., and X is S, Se, Te, etc.. The consumption of solid material from the source zone end and the formation of crystalline material in the growth zone is the result of this process.

Ampules were prepared for the vapor transport experiments from standard quartz tubing. The length of the

ampule was 20 cm and the bore was 2cm with a wall thickness of 0.2cm. In order to reduce impurities and active sites on the wall of the tube, careful cleaning and quartz treatment were required. The quartz tubes were vigorously washed with deionized water and acetone, and then were left in a mixture of $HCl-HNO_3$ (3:1) in some cases, and in $HF-HNO_3$ (1:1) in others, for six hours. After being washed and dried, a systematic flame polishing was applied along the ampules. The importance of this flame polishing is that it helps to close micropores or striations on the surface of the quartz, which can act as nucleation sites. The ampules were washed again with deionized water, dried and held for 8 hours at 900°C under a vacuum of 10^{-5} Torr to remove any traces of acids or water.

For each composition, 3 gms of polycrystalline sample annealed for 10 days were used as starting material. The starting sample was inserted together with 5-10mg/cc of iodine into a tube with a constriction previously prepared at 20cm from the bottom.

Another source of undesirable nucleation sites is the charge material itself. In the process of charging the ampule, the walls usually come in contact with the powder of the starting material which can act as polycrystalline

seeds. This difficulty could be avoided almost completely by taking the following precautions. The first was to use a funnel when loading the starting material. The second was to place the ampule after sealing and before growth in reverse-transport. This reverse-transport consists in the inversion of the direction of the temperature gradient so that transport of material takes place in the opposite direction, i.e. from the deposition zone to the growth zone. This temperature inversion gives a final cleaning on the quartz walls in the deposition zone.

As the iodine is volatile, the end of the tube containing the reactants was cooled to liquid nitrogen temperature during evacuation. The tubes were sealed when the vacuum was better than 10^{-5} Torr. After sealing the ampule at the constriction, the deposition zone was again vigorously flame polished for several minutes. The sealed tubes were then placed in a Lindberg furnace, which was initially set up for reverse-transport conditions. The growing conditions were set up 72 hours after the reverse-transport, and in fig. (III-1) a typical furnace profile used to grow these chalcopyrite samples is shown.

The growth times were in the range from 7 to 30 days. The ampules were then furnace cooled to room temperature. In each case, needle-like single crystal

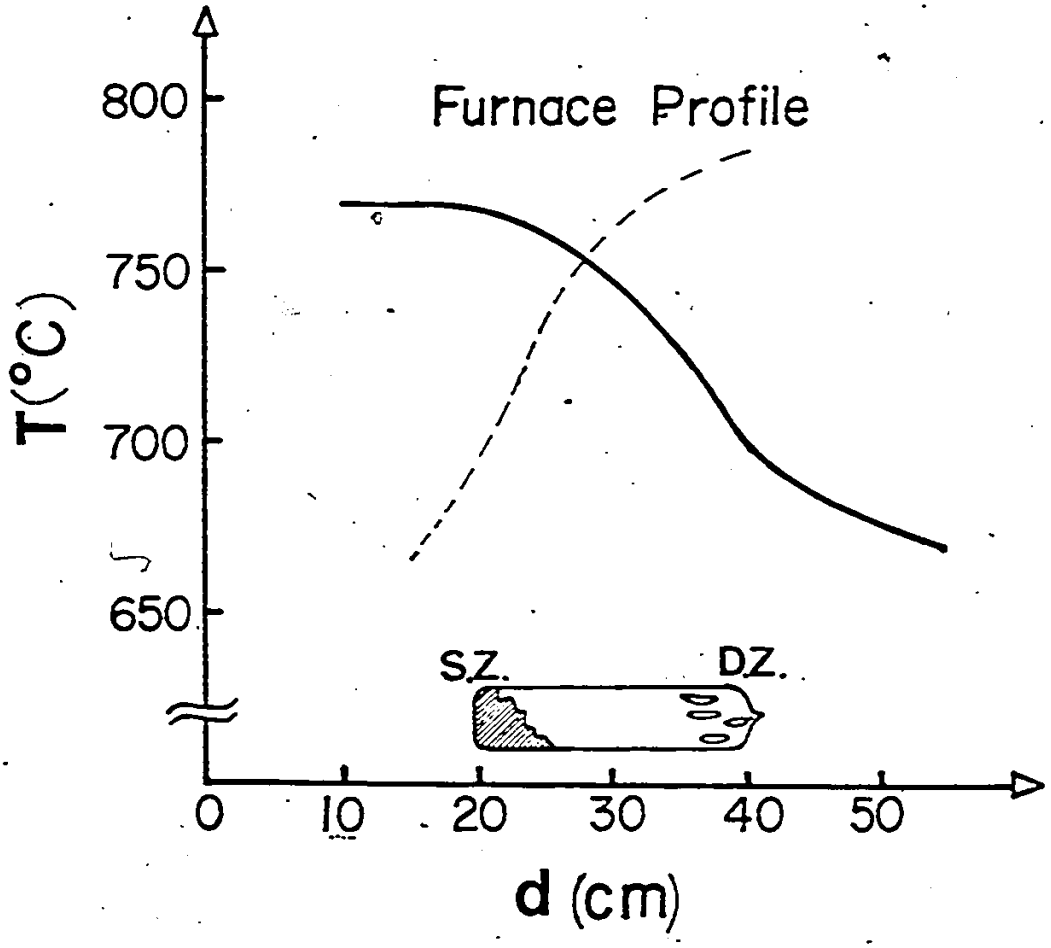

Fig. III-1 Typical temperature profile used in the CVD experiments. Dashed line, reversed transport conditions. Solid line, growth conditions.

specimens were obtained at the deposition zone. The samples were washed in warm alcohol. Those resulting specimens which were suitable for optical experiments, were of dimensions of about 10X4X2 mm and presented good natural surfaces.

CHAPTER IV

EXPERIMENTAL MEASUREMENTS

INTRODUCTION

The X-ray and optical experimental techniques used in the present investigation are presented in this chapter. The methods used to correct for absorption effect the Bragg angle in the X-ray work are indicated. Optical absorption and wavelength modulated reflectance measurements are discussed.

IV-1 X-RAY MEASUREMENTS

Debye-Scherrer x-ray powder photographs were used to check the homogeneity condition of each sample and to determine whether single phase solid solution was obtained. The films that indicated good equilibrium conditions for the samples were used to calculate lattice parameter values for the alloys.

With regard to the x-ray measurements, there are several effects such as absorption that cause the lines to be displaced from their true positions, so that the measured angles will not be the true Bragg angles. Two

methods were used to correct for absorption effects. these being the Nelson-Riley extrapolation (45N1). and the internal calibration technique.

In the case of samples with c/a=2. the Nelson-Riley method was used to obtain accurate parameters values. The Nelson-Riley technique involves a plot of the lattice parameter a against a function of the measured Bragg angle given by

$$F(\theta) = (\mathrm{Cos}^2\theta/2\mathrm{Sin}\theta + \mathrm{Sin}^2\theta/2\theta)$$

The best straight line is drawn through the points. and the value of a is obtained by extrapolating to $F(\theta)=0$.

For specimens with c/a≠2. the Nelson-Riley technique becomes a method of continuous approximation whereby the a and c parameters are plotted against the above error function and adjusted until the resulting lines are parallel. This method has proved to be tedious, thus the internal calibration method was chosen here as the method to determine accurate parameter values for samples with c/a≠2.

The internal calibration method involves intimately mixing an internal standard of accurately known

lattice parameter with the sample being x-rayed. Then the Bragg angles for the two substances are determined and effects due to absorption are calculated for the standard sample. from these a correction curve of $\Delta\sin^2\theta$ Vs $\sin^2\theta$ may be plotted. Hence corrected values of $\sin^2\theta$ for the working substance are obtained allowing an accurate determination of the lattice parameter a to be made for these alloys with $c/a \neq 2$.

IV-2 ANALYSIS OF X-RAY POWDER RESULTS

In the case of cubic zincblende materials, analysis was approached using the well known Bragg condition for cubic crystals, given by

$$\sin^2\theta = \lambda^2(h^2 + k^2 + l^2)/4a^2 \qquad (IV-1)$$

as the zincblende is face centered cubic, the indices h, k and l satisfy the conditions

$$h + k + l = 4n$$

$$h + k + l = 4n + 2$$

$$h + k + l = 2n + 1; \quad n \text{ integer}$$

for reflection to occur. These conditions give strong lines for $N = h^2 + k^2 + l^2 = 3, 11, 16, 19, 24, 27, 32$, etc.

and weak for N= 4, 12, 20, etc.. Thus, these values of N were used to obtain the lattice parameter values for the cubic samples.

In addition to the lines expected from the zincblende structure, for some of the cubic alloys, extra lines were observed in these photographs but at lower intensity. These lines are due to the presence of an ordered cubic structure which is shown by some of the materials investigated in the present work. This will be discussed in chapters VII and VIII.

For tetragonal materials, the Bragg condition is given by

$$\sin^2\theta = \lambda^2[(h^2+k^2)/a^2 + l^2/c^2)]/4 \qquad (IV-2)$$

Since the atomic sites in chalcopyrite have the same positions as in the zincblende structure, all the zincblende diffraction lines must occur in the chalcopyrite diffraction pattern. These chalcopyrite diffraction lines may be indexed by doubling the Miller index l of zincblende, i.e. the reflection N=11 corresponding to the 311 diffraction line in zincblende will correspond to the 312 and 116 diffraction lines in the chalcopyrite case, and for materials with c/a=2 these

reflection will occur at exactly the same angle. However, for samples with c/a<2 the 312 and 116 lines will split into two diffraction line. Possible combinations of the values of h, k and l are listed in table IV-1. In the case of chalcopyrite alloys, in addition to these zincblende derived diffraction lines, weak extra lines due to the ordering of the cations also occur. These ordering lines were used, in some cases, to estimate the limit of chalcopyrite single phase behavior for tetragonal samples with ratio c/a=2.

To determine lattice parameter values for alloys with c/a<2, once the effects of absorption were determined and the Bragg angles corrected, values of $\sin^2\theta$ were calculated and the Miller indices of the diffraction lines were determined. It was found that the indexing of the lines for low angle reflection was clear, thus using these lines of low angle, values of a and c were calculated using a least squares fit to equation IV-2. These values of a and c were used to determine the indices of the higher angle reflections. After all the lines were indexed, values for a and c were finally calculated using all of the lines obtained by a least squares fit to eq. VI-2.

TABLE IV-1 Possible combinations of h,k,l for zincblende and chalcopyrite materials.

N	zincblende (hkl)	chalcopyrite (hkl)
3	111	112
4	200	200
		004
8	220	220
		204
11	311	312
		116
12	222	224
16	400	400
		008
19	331	332
		316
20	420	420
		404
		208
24	422	424
		228
27	511	512
	333	336
		1110
32	440	440
		408
35	531	532
		516
		3110
36	600	600
		0012
40	620	620
		604
		2012
43	533	536
		3310
44	622	624
		2212
48	444	4416
51	551	552
	711	712
		5110
		1114
56	642	644
		628
		4212
59	553	556
	731	732
		5310
		716
		3114

IV-3 ORIENTATION OF SAMPLES

In the single crystal work, some of the samples were oriented by back reflection Laue X-ray photograph (56C1). The angular coordinates γ and δ of each diffraction spot on the film, corresponding to each plane normal, were measured by using a Greninger chart for a specimen-to-film distance of 3cm, these parameters being illustrated in fig. (IV-1). Then, the angle ζ between the plane normals was calculated using the equation.

$$\text{Cos}\,\zeta = \text{Cos}(\gamma_1 - \gamma_2)\,\text{Cos}(\delta_1 - \delta_2)$$

The planes were identified by comparison with a list of calculated interplanar angles for these samples give by

$$\text{Cos}\,\zeta = \frac{h_1h_2 + k_1k_2 + l_1l_2(a/c)^2}{\{(h_1^2 + k_1^2 + l_1^2\,(a/c)^2)\,(h_2^2 + k_2^2 + l_2^2\,(a/c)^2)\}}$$

The results obtained from the back reflection analysis showed that the surface of these samples corresponds to the (112) plane. This result is in agreement with earlier data (74S1), which showed that these chalcopyrite crystals have this growth habit.

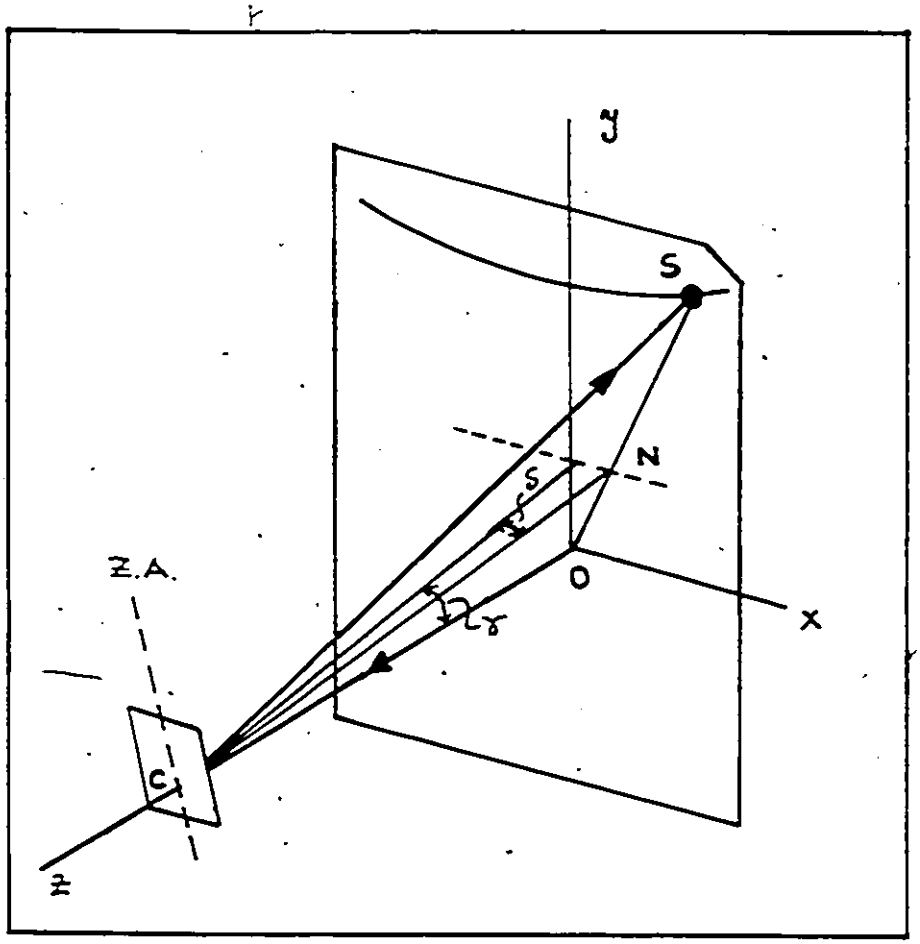

Fig. IV-1 Location of back reflection Laue spot S of an (hkl) plane.

IV-4. OPTICAL MEASUREMENTS

IV-4a OPTICAL ABSORPTION

The determination of the optical constants of a semiconductor can provide a wealth of information about their band structure. The most common methods to determine optical properties are reflection and absorption, which can be greatly enhanced by means of modulation or derivative techniques. At short wavelengths, the photons can excite electrons from the valence band to the conduction band giving origin to the so-called interband transitions. In this optical region, the process takes place at a wavelength corresponding to the fundamental energy gap of the semiconductor. The results are the observation of a weak maximum in the reflectivity spectrum and of an absorption edge in the absorption spectrum corresponding to a rise in the value of the absorption coefficient above the background as the energy of the incident radiation increases.

Two possible cases must be considered for interband absorption. If transition occurs between band extrema situated at the same point in the Brillouin zone, the process is called a direct transition. The

absorption in this case is characterized by a steep rise in the value of the absorption coefficient over several tens of milli electron-volts in the value of $h\nu$. The second case arises when the transition is between band extrema situated at different points in the zone, then phonons must be involved to provide the needed change of momentum. This phonon assisted transition is referred to as an indirect transition. The absorption curve in this case is shallow and spread over a range of $h\nu$ of several hundred milli electron-volts and the reflectivity structure corresponding to this type of interband transition is practically not detectable.

The problem of interband transitions has to be approached from quantum mechanical considerations. The absorption coefficient associated with this process depends on the probability per unit time of an electron being promoted from the valence band to the conduction band. Thus, the absorption coefficient is given by the number of quanta absorbed per unit time per unit volume divided by the flux density. For simple parabolic bands, the absorption coefficient α due to direct allowed transitions has been shown to be given by (67J1)

$$(\alpha h\nu)^2 = A(h\nu - E_o) \qquad \text{(IV-3)}$$

where A is a slowly varying function of the energy and E_o is the energy gap of the material.

Allowed transitions take place, for example, if the valence band wavefunction are derived from p-states of the individual atoms, and the conduction band wavefunction from s-states. If the former were derived, for example, from d-states, then since d----->s is a forbidden atomic transition the transition would be called forbidden or non-allowed for a semiconductor material. In this case it may be shown (67J1) that the absorption coefficient is give by

$$(\alpha h\nu)^{2/3} = B(h\nu - E_o) \qquad \text{(IV-4)}$$

The absorption curve given by this type of transition is shallow and spread over several hundred of milli electron-volts as in the case of an indirect transition indicated above.

When the transition is indirect, the matrix elements between the valence band to conduction band through a virtual state as well as the absorption and emission of phonons have to be considered. In this case, the absorption coefficient is given by (67J1)

$$(\alpha h\nu)^{\frac{1}{2}} = C(h\nu - E_o) \qquad \text{(IV-5)}$$

The above equations will be used to analyze the experimental data obtained from the absorption measurements.

IV-4b. PREPARATION OF SAMPLES FOR OPTICAL ABSORPTION

The sample preparation was undertaken immediately after the x-ray analysis was completed. It was found that most of the polycrystalline alloys were brittle and in some cases tiny voids were distributed at random through the ingots. These tiny voids were probably due to the occurrence of small pockets of unreacted sulfur or selenium or tellurium gases as the alloys froze at high temperature.

All samples were sliced into thin discs with thicknesses between 0.5mm and 1.0mm. The slices were reduced in thickness as much as possible by lapping on a glass plate covered with a slurry of methanol or water and alumina powder from 5 to 1 micron mesh sizes. The samples did not react with water, methanol or acetone.

The samples were mounted on a brass rod using molten paraffin wax and polished on a polishing machine

down to thicknesses of about 100μm in most cases. The next step was to mount the sample on a small thin copper plate with an aperture in the center which was covered by the prepared sample.

In the case of the $CuIn(S_x Se_y Te_z)_2$ system the plates were mounted in a CTI-Cryogenics model 21Sc Cryodyne Cryostat with a Lake Shore cryotronics model drc-80c Digital temperature control, so that optical measurements could be recorded at low temperature also.

IV-4c. OPTICAL ABSORPTION MEASUREMENTS

The optical system used for the transmission measurements was the same as the one used by earlier workers (82G1), with the exception of an aluminum mirror that was placed near the exit slit of the spectrometer as is shown in fig. (IV-2). The advantage of this mirror, driven by a motor, is that besides the fundamental optical measurements one can have easy access to the very useful wavelength modulation techniques such as modulated absorption (WMA), modulated reflectance (WMR), modulated photoconductivity (WMPC), etc. The WMR technique will be discussed in the next section.

Due to the mechanical properties of the

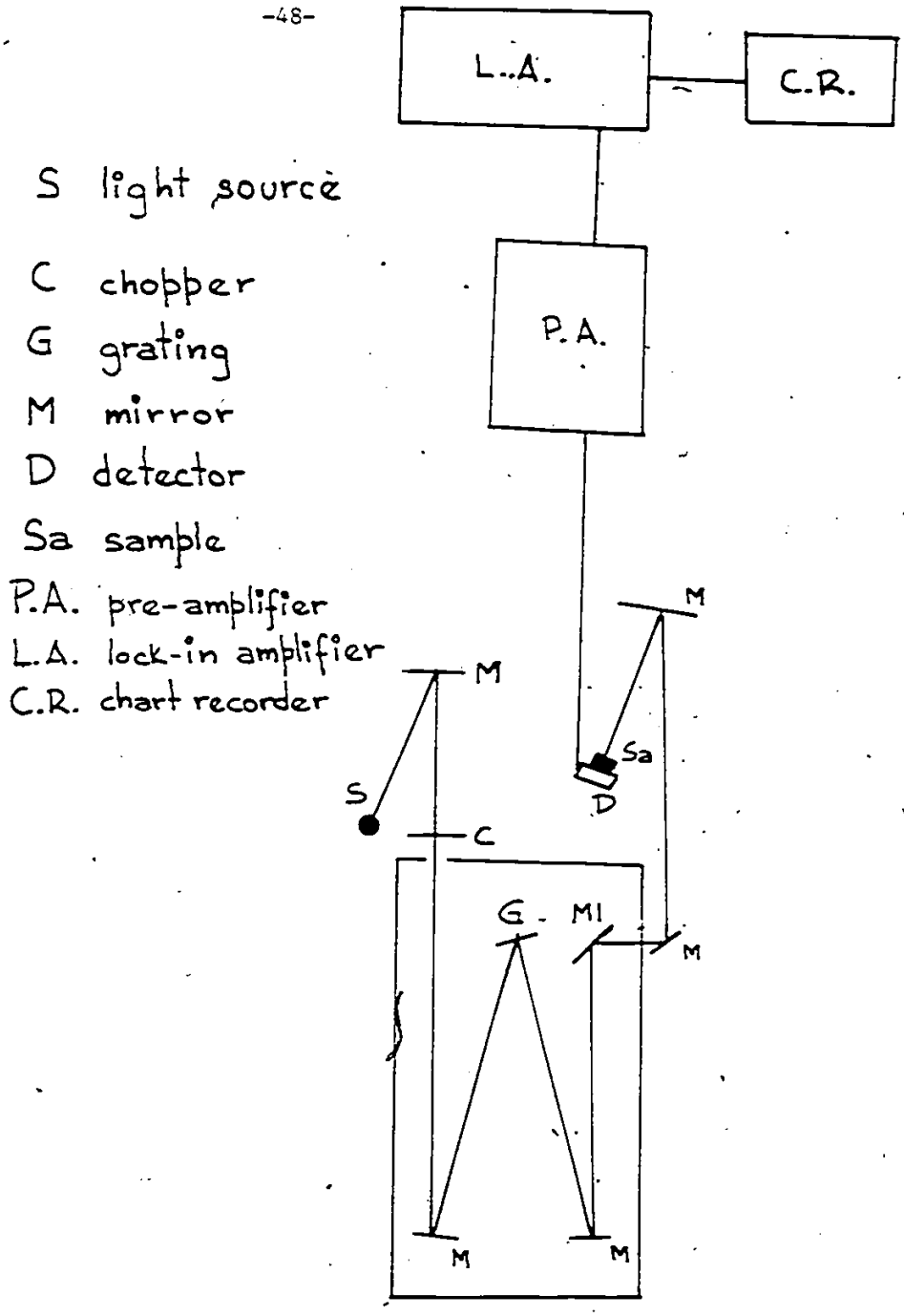

Fig. IV-2 Block diagram of the optical experimental set-up used in the absorption experiments.

polycrystalline samples discussed above, and as no contacts are required, transmission measurements were chosen as a method which was applicable for all of the polycrystalline materials investigated here. This method has been long used to study the fundamental absorption edge of semiconductor materials (67J1) (84A1).

For energies near the absorption edge and if the sample is sufficiently thick that no interference fringes are observed, it can be shown that the transmitted intensity for a material can be taken as (68G1)

$$I = I_o (1-R^2) \exp(-\alpha d) \qquad (IV-6)$$

where α is the absorption coefficient, d the thickness of the sample and R is the reflectivity which is a slowly varying function of photon energy and has a maximum possible value of one. Thus the $(1-R^2)$ term may be treated to a good approximation as a constant. Taking the natural logarithm of both sides of eq.(IV-6) one obtains

$$\text{Ln } (I/I_o) = -\alpha d - \text{Ln } K \qquad (IV-7)$$

In order to determine α from the above equation, it is necessary to find a value for Ln K. Thus (1/d)Ln K form part of a "background" that must be subtracted from

the value of $(1/d)Ln(I_o/I)$ before proceeding with any further analysis. In fig.(IV-3) the absorption coefficient values are shown as a function of photon energy for a typical sample of the system $CuIn(S_x Se_y Te_z)_2$ with y=0.5 z=0.4 at 300K. That graph shows that a straight line extrapolation of the background absorption can be subtracted from the measured value of $(1/d)Ln(I_o/I)$ to give the required values of α. It was found that the linear variation of the background was followed for most of the samples. Thus, in the calculation of α, a straight line extrapolation of the background absorption was subtracted from the measured value of $(1/d)Ln(I_o/I)$.

With regard to the $I-III-VI_2$ compounds, since reflectance and absorption measurements have previously shown (74S1) that the transition is direct, equation (IV-3) was used for the analysis of the absorption data in the next chapter and a graph of $(\alpha h\nu)^2$ Vs $h\nu$ is also shown in fig.(IV-4) at 300K and 70K. The value of the energy gap was then given by the intercept on the $h\nu$ axis as is illustrated in that figure.

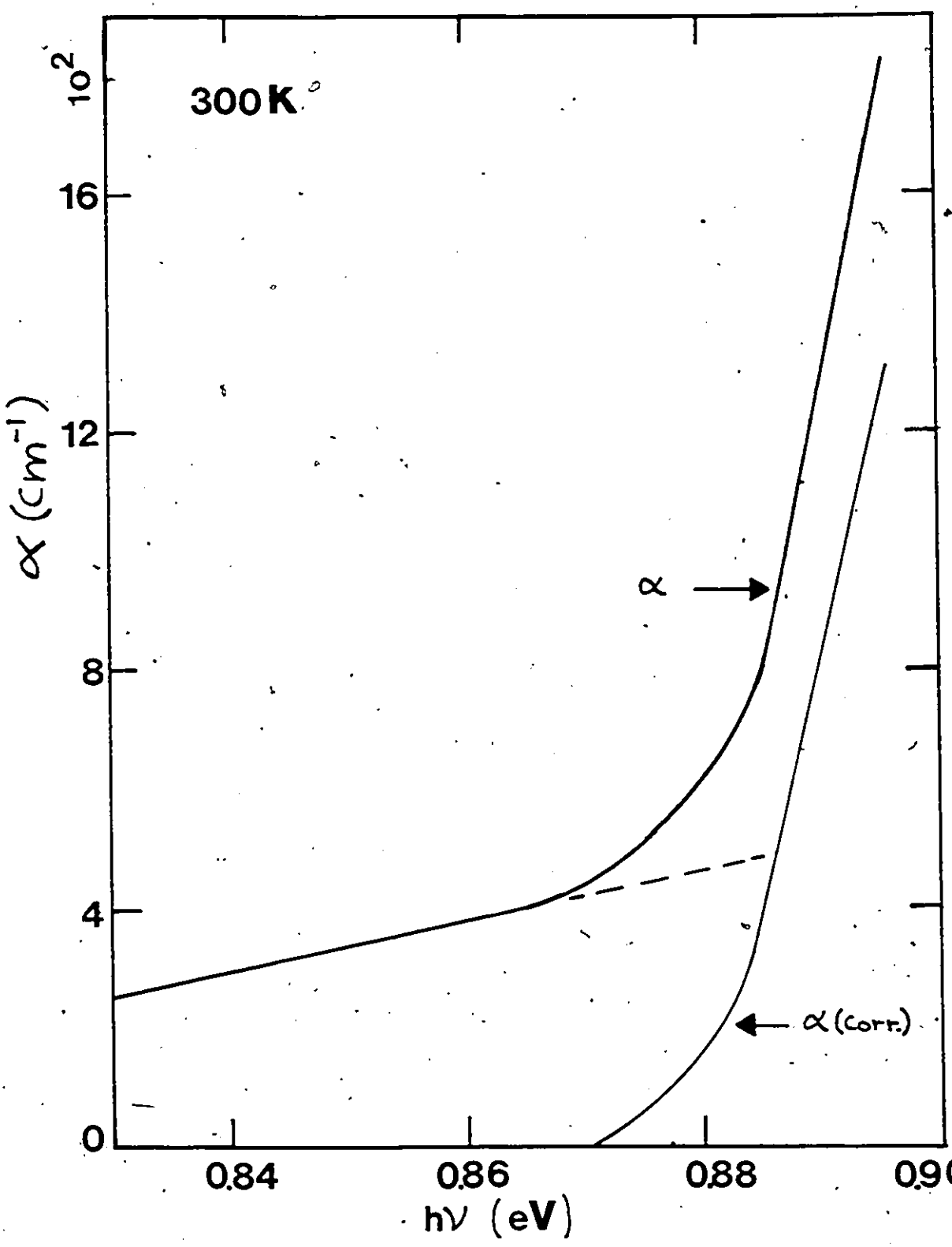

Fig. IV-3 $CuIn(S_x Se_y Te_z)_2$. Absorption coefficient α vs. $h\nu$ for the sample $x=0.1$ $y=0.5$. A straight line extrapolation of the background, dashed line, was subtracted from experimental values to give absorption coefficient α.

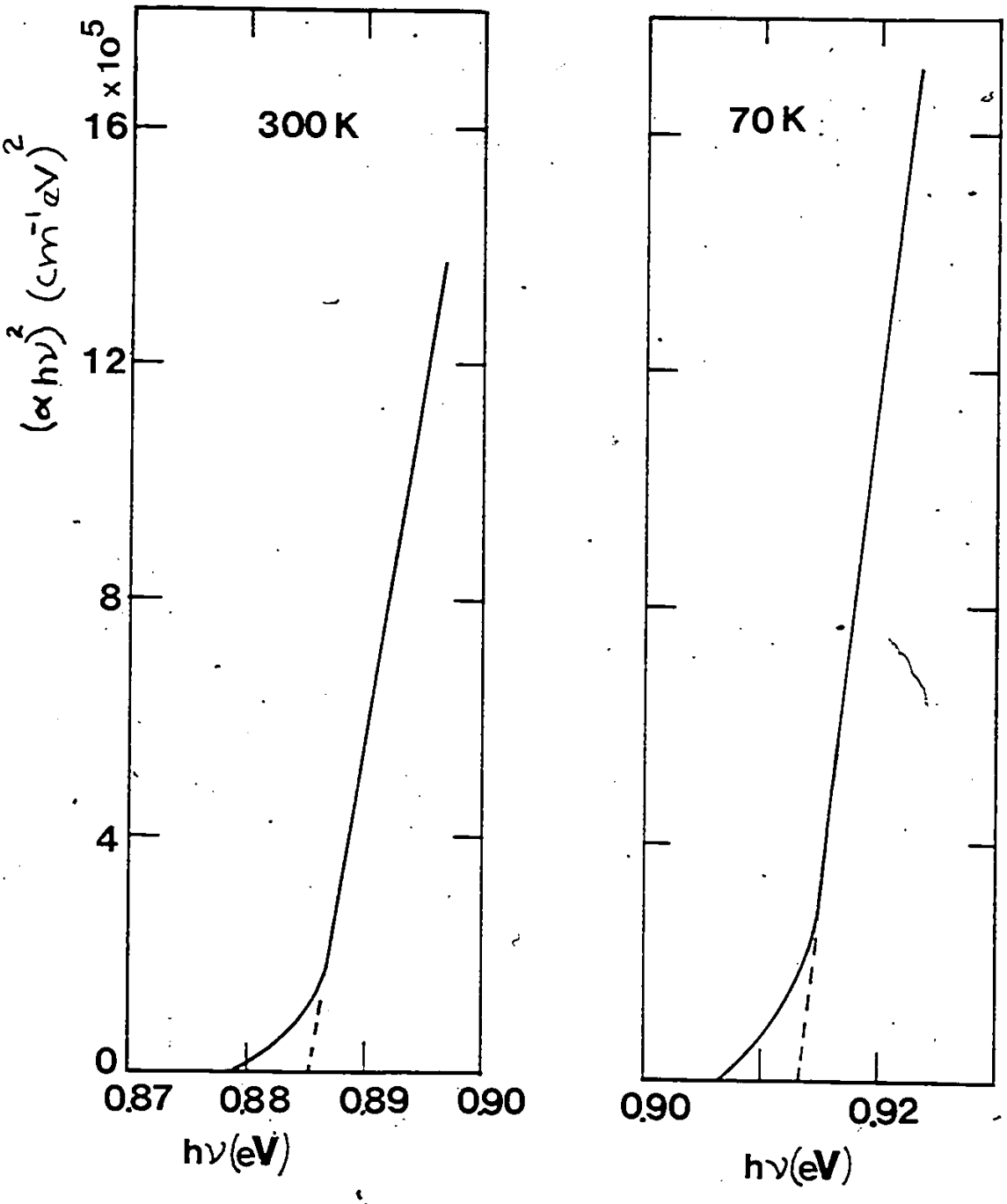

Fig. IV-4 $CuIn(S_x Se_y Te_{2-x-y})_2$. $(\alpha h\nu)^2$ vs. $h\nu$ curves for the sample x=0.1 y=0.5 at 300K and 70K.

IV-4d WAVELENGTH MODULATION REFLECTANCE

The common feature of all modulation spectroscopy techniques is the measurement of the derivative of some optical property such as absorption or reflectance with respect to some parameter. Hence the optical structures associated with critical points are greatly enhanced, and by using phase sensitive detection techniques the sensitivity in the measurement of this derivative can be made very large (69C1).

The various methods that have been used can be divided into two general classes, according to the choice of the parameter of differentiation: the energy gap of the sample or the wavelength of the incident light. In the former case the variable of differentiation is an external perturbation applied to the sample such as electric field, temperature, stress, etc. In the latter case the wavelength is modulated by vibrating either the slit, or the grating, or a mirror in the monochromator or another suitable arrangement. Thus, the modulated transmission or reflectivity is measured.

In reflectance experiments, the reflected light

intensity is given by (69C1)

$$I = I_o R$$

where I_o is the intensity of the incident light, and R is the sample reflectivity. Then the measured derivative in wavelength modulation reflectance is

$$dI/d\lambda = I_o (dR/d\lambda) + R(dI_o/d\lambda)$$

The first term of the above equation contains the derivative of the sample reflectivity and is the quantity that gives the required information. The second term contains the derivative of the incident light intensity which can make undesirable contribution to the wavelength modulation signal. Such spurious peaks in $dI/d\lambda$ can be eliminated by using the double beam detection system. In that configuration the values of $I^{-1}(dI/d\lambda)$ and $I_o^{-1}(dI_o/d\lambda)$ can be simultaneously measured and electronically subtracted, giving as a result the normalized derivative of the sample reflectivity.

$$R^{-1}(dR/d\lambda) = I^{-1}(dI/d\lambda) - I_o^{-1}(dI_o/d\lambda)$$

In the present experimental work, most of the single crystal samples showed sufficient WMR signal to be

detected in most regions of the spectrum without either normalization or subtraction, except in and around certain strong unidentified peaks. It was found, after adjustment of the different optical components (sources, detectors, gratings, polarizers, etc), that most of these peaks were due to either gratings or light sources used in the optical system. However, in two cases the peaks were found to be probably due to a mirror inside the spectrometer which could not be replaced. Thus to avoid these wavelength, a grating was calibrated using a mercury lamp in the region corresponding to the second order harmonics of the optical spectrum of interest. The wavelength was obtained using a calibration curve of wavelength of mercury lines Vs wavelength of the lines in the second harmonic region.

IV-4 e WMR MEASUREMENTS

The WMR measurements were made using the experimental arrangement depicted in fig.(IV-5). The mirror M1 placed near the exit slit was vibrated by a motor at about 20 Hz in order to produce adequate modulation. With the modulation mirror held stationary the system was used for the normal absorption measurements described above. The slit width was set to 1mm which gives a reciprocal linear dispersion of the monochromator in the

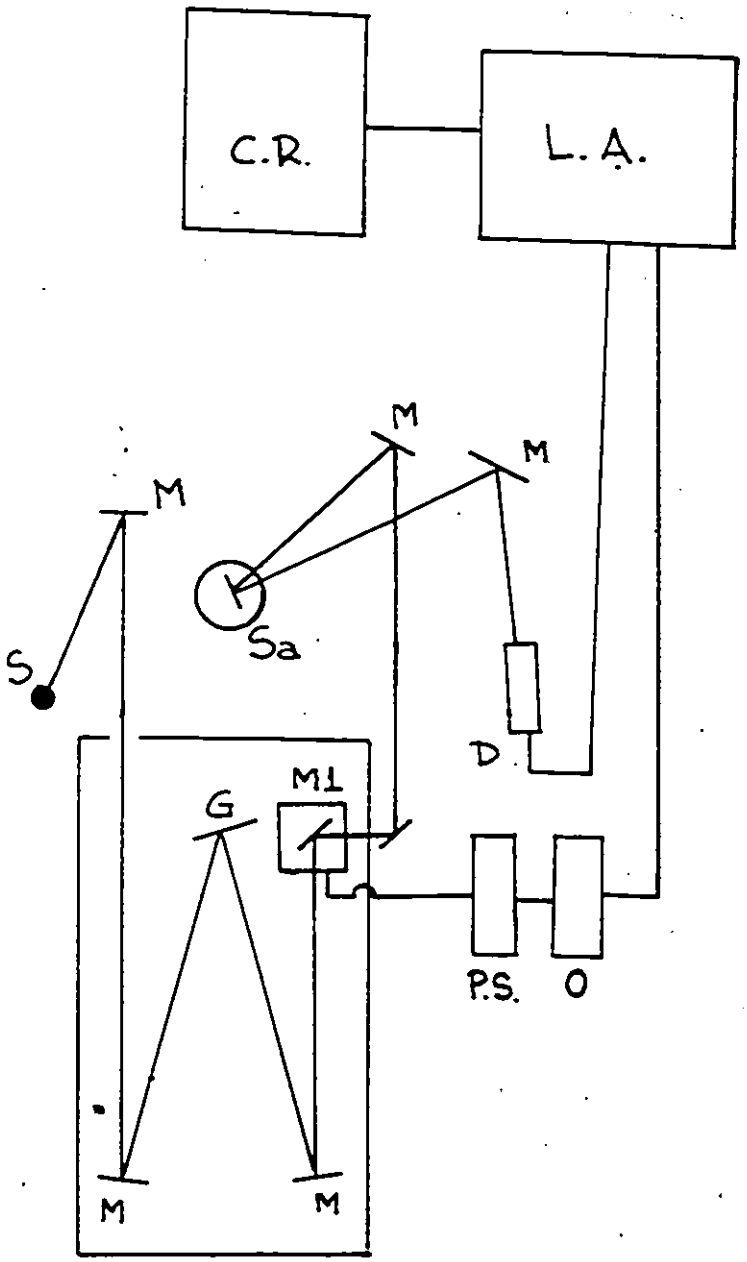

Fig. IV-5 Optical experimental set-up used in the wavelength modulated reflectance measurements. M1 is a mirror driven by a motor. P.S. power supply. O wave generator. S_a sample and cryostat.

region of interest of 10.5 Å/mm with a grating of 1200 gr/mm, so that the estimated depth of modulation was approximately 10 Å for an angular rotation of the mirror of about one degree when the mirror to exit slit distance was 20cm. The reflected modulated light from the sample was measured with a IP28 photomultiplier. The output from the photomultiplier was applied to a P.A.R 186 lock-in amplifier locked to the reference signal (20Hz) from the oscillator which drives the motor. The output from the lock-in was registered by an Electronik Model 19 strip chart recorder. Thus a WMR spectrum of the reflected crystal signal as a function of wavelength could be obtained at each temperature.

CHAPTER V

RANGES OF SOLID SOLUBILITY AND OPTICAL ENERGY GAP VALUES IN $CuIn(S_xSe_yTe_z)_2$ AND $CuGa(S_xSe_yTe_z)_2$.

V-1. THE $CuIn(S_xSe_yTe_z)_2$ SYSTEM.

V-1a INTRODUCTION

Most of the previous work on the I-III-IV_2 alloys has been carried out on pseudo-binary systems of the type $Cu_{1-x}Ag_xGaSe_2$ and $CuIn(S_{1-y}Se_y)_2$ etc. (75R1), with little work being done on materials involving tellurium. More recently Chapman et al. (79C1) have determined the lattice parameter and energy gap values of the $(Cu_{1-x}Ag_x)In(S_{1-y}Se_y)_2$ alloys and Avon et. al. have studied the $(Cu_{1-x}Ag_x)(Ga_{1-y}In_y)(Se_{1-z}Te_z)_2$ alloys, determining the ranges of single phase solid solution and lattice parameters values over the complete composition range (84A1) and finding optical energy gap values over certain sections of the alloy system (83A1).

The pseudo-binary alloys $CuIn(S_{1-y}Se_y)_2$ are of interest as possible materials for solar cell production and improvements in performance may be obtained by addition of some tellurium. Thus, knowledge of the

crystallography and optical energy gap values of the system $CuIn(S_xSe_yTe_z)_2$, with x+y+z=1, is required.

The main aim of the work described in this chapter was to determine the range of single phase behavior, lattice parameters and optical energy gap values of these alloys at 300K and 70K.

V-1b X-RAY RESULTS AND ANALYSIS

Samples representing 60 alloy compositions were investigated and all showed either single phase or two phase chalcopyrite structure. In all cases, it was found that c/a=2.0, and hence the value of a was determined for each phase as described in chapter IV. Figure V-1 shows for all single phase samples the variation of a as a function of z for various lines of constant y. It is seen that over the whole range available, within the limits of experimental error the lattice parameter a varies linearly with z for lines of constant y. If the values of a are plotted against other composition variables in a similar way, a similar variation is found; e.g., fig. V-2 shows the variation of a with y for lines of constant x. The limits of single phase solid solution can be determined by considering the lattice parameter values obtained for the two phase samples. This is illustrated in fig. V-3, which

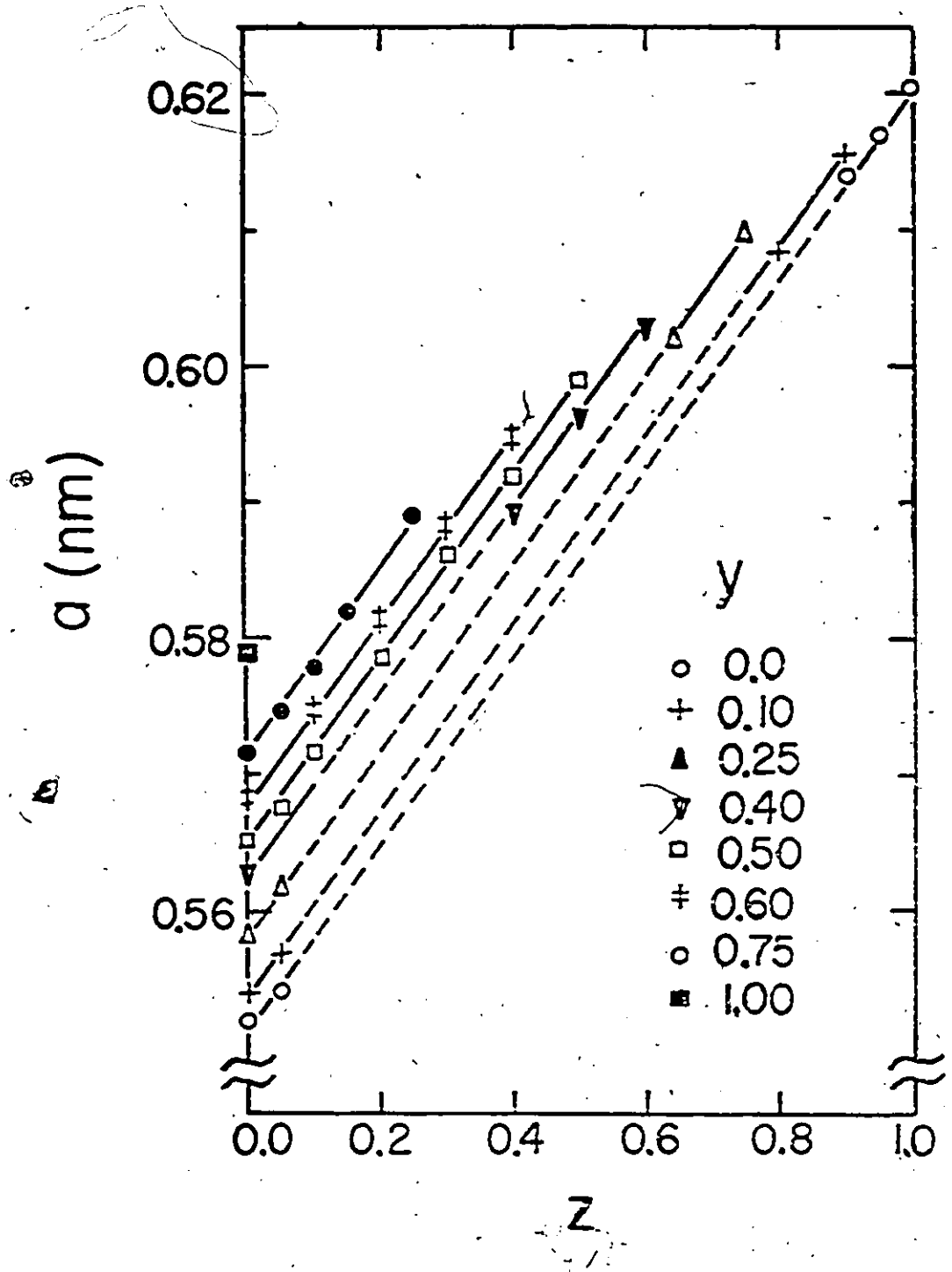

Fig. V-1 $CuIn(S_x\ Se_yTe_z)_2$. Variation of lattice parameter a with z for various constant values of y, for samples showing single phase behavior.

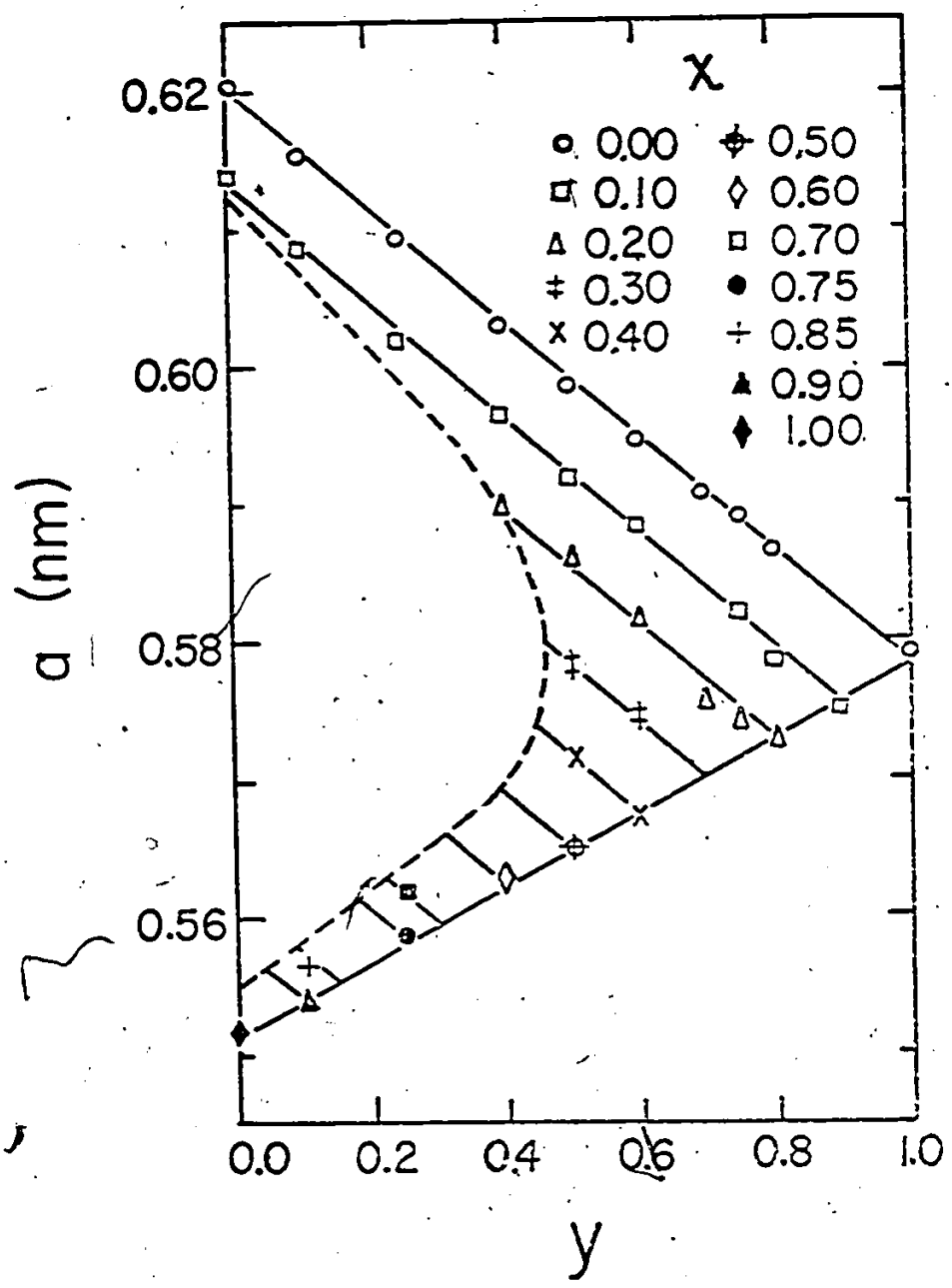

Fig. V-2 $CuIn(S_x\ Se_y\ Te_z)_2$ .Variation of lattice parameter a with y for various constant values of x, for samples showing single phase behavior.

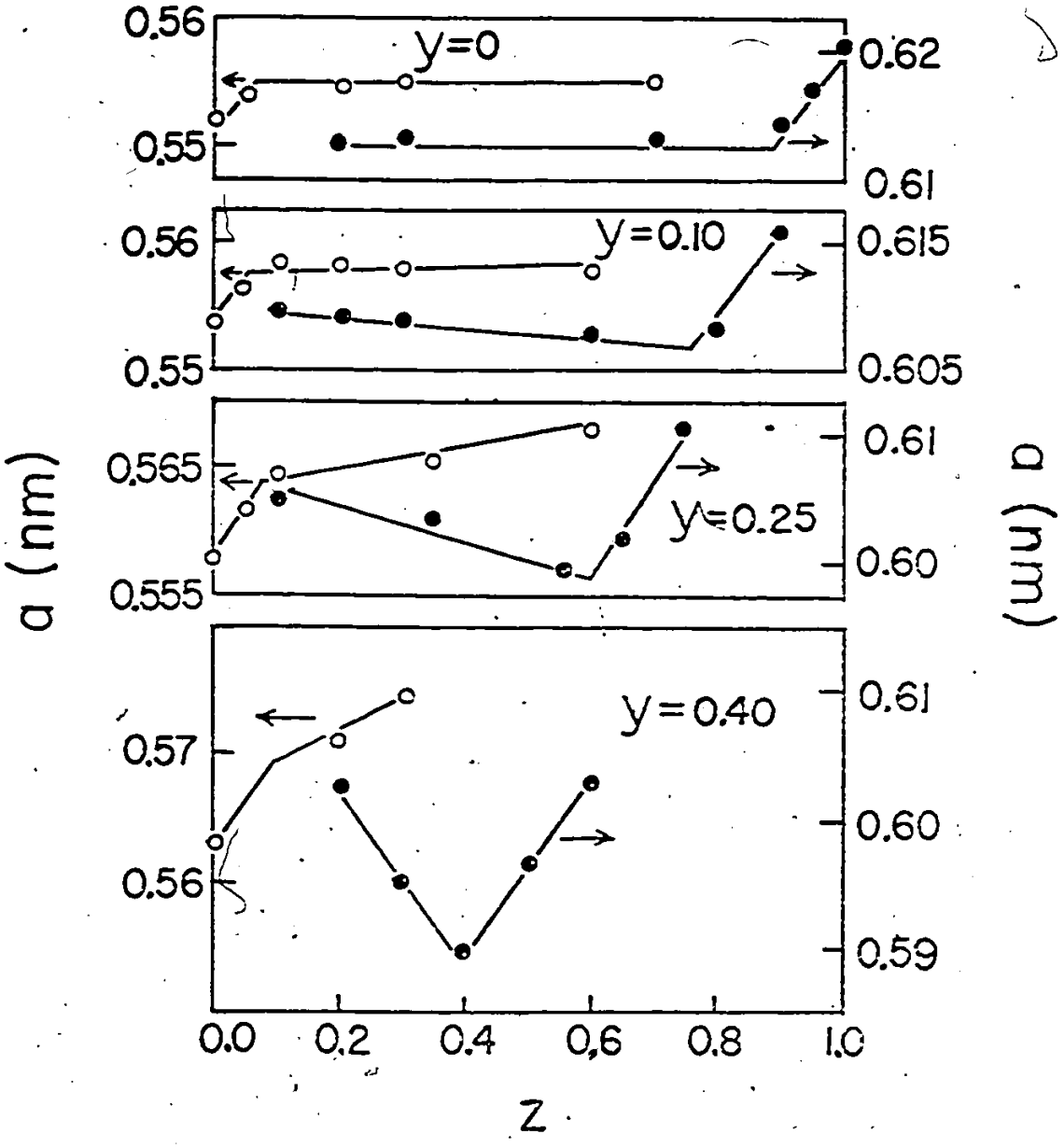

Fig. V-3 $CuIn(S_x Se_y Te_z)_2$. Variation of lattice parameter a with z for various constant values of y, for both single and two phases samples.

again shows values of a plotted against z for lines of constant y. In the case of y=0, this line is in the bounding section $CuIn(S_{1-z}Te_z)_2$ which is pseudo-binary and the tie lines in the two phase region lie in the section. This means that the lattice parameter values of the two phases are constant and independent of z, as is seen in fig. V-3, and the limits of solid solution are easily determined. For the other values of y, these lines of constant y are in general sections which need not contain the tie lines and, as is seen from fig. V-3, in these cases the lattice parameter values in the two phase field vary with z. Assuming that to a good approximation straight lines can be drawn through these points, the limits of solid solution are taken as the intersection of these lines with the line through the single phase points. These values can then be used to draw the limits of solid solubility shown in fig. V-4.

The variation of any physical parameter of an alloy semiconductor with composition, temperature, etc is of interest from both the academic and technological viewpoints, and much work have been carried out to determine the experimental variations of parameters such as lattice parameter, energy gap, resistivity, etc with temperature or composition. When values for these parameters have been determined they are fitted to some

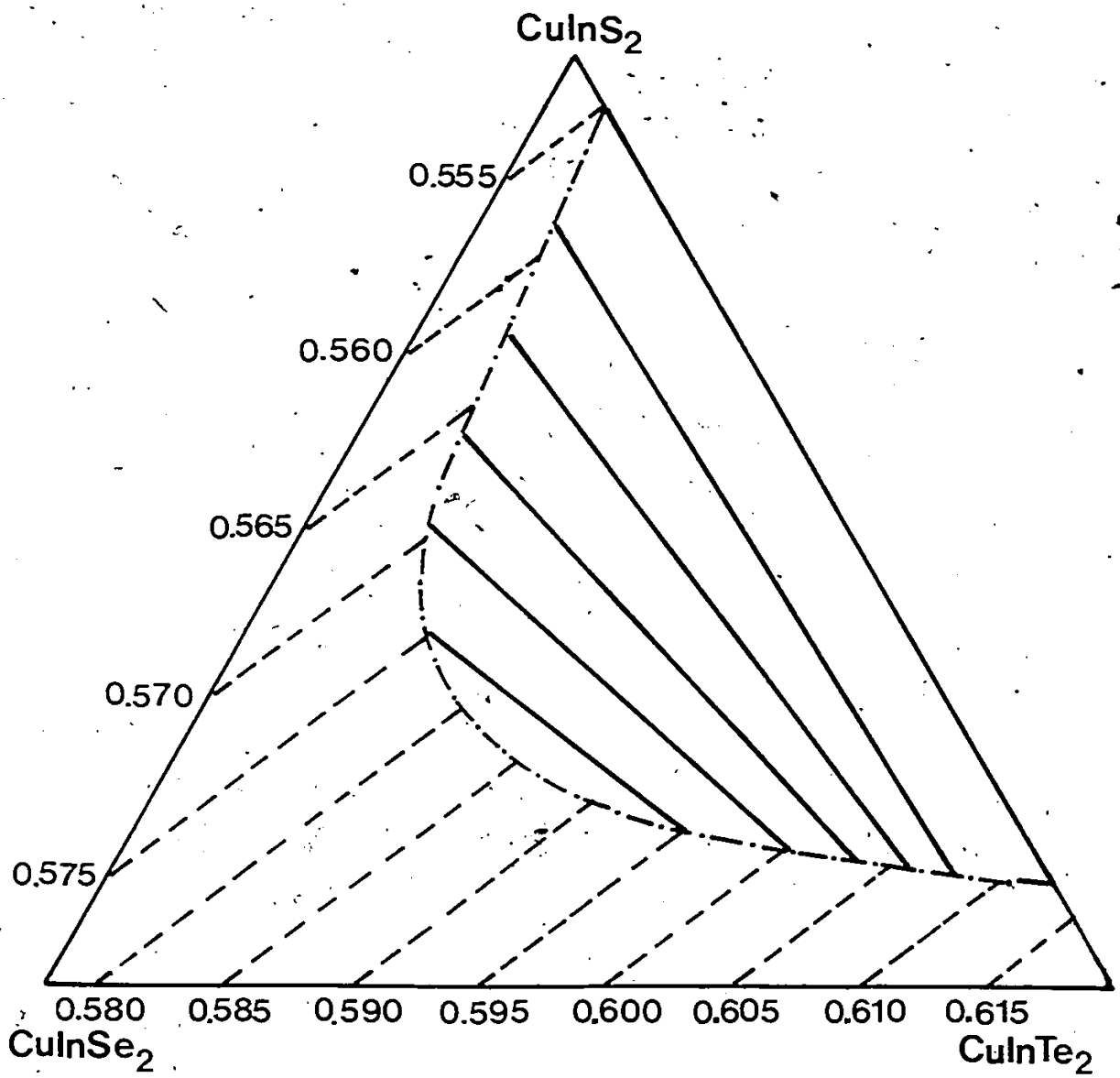

Fig. V-4 $CuIn(S_x\ Se_y\ Te_z)_2$. Isothermal section for samples annealed at 600 °C and quenched to room temperature. The dash-dotted gives the miscibility limit. The dashed lines are contours of constant a, value indicated in nm. The full lines are tie lines in the two phase field.

convenient equation, such as those discussed below. The reasons for these fits is that it may be of interest to find a mathematical form to represent the experimental data so that interpolation or some other computation can be carried out. In this case the physical significance of the parameters is of no interest and one merely requires the best and simplest fit to the experimental data. In a more fundamental investigation, the objective may be to obtain an understanding of the relevant theory or of the properties of the material concerned, and in this case the significance of the parameter values are the important factors.

In the rest of this analysis, as well as in the next section, a mathematical form to represent the present experimental results will be given. In all cases the aim is to provide a relation suitable for interpolation of the data.

Since, as is seen from figs. V-1 and 2, the lattice parameter a varies linearly with x at constant y and linearly with y at constant x, a general expression for a in the single phase region can be written as

$$a=A+Bx+Cy \qquad (V-1)$$

Values of a for 39 compositions in the single phase field were obtained and these were fitted to Eq. 1. The resulting relation was found to be

$$a=0.6201-0.0687x-0.0420y \text{ nm} \qquad (V-2)$$

and the standard deviation of the fitted points was $\sigma=0.0006$nm. The lines shown in fig. V-1 and 2 are the fitted values from eq. V-2. Using eq. V-2, contours of constant a were caltulated and these are shown in fig. V-4. Also from eq. V-2 it was possible to determine the values of a along the miscibility boundary and hence, from the two phase lattice parameter values given in fig. V-3, the positions of the tie lines were determined, and representative tie lines are shown in fig. V-4.

V-1c ENERGY GAP RESULTS AND ANALYSIS

Optical absorption measurements were made at 300K and 70K on most of the single phase samples and values of E_o determined as indicated above. The resulting variations at 300K of E_o with y at constant x and with z at constant y are shown in figs. V-5 and 6. Because of the range of the miscibility gap, it is seen that for some lines of constant x or of constant y very few values of E_o are available. However, for those cases where a number of points can be obtained over an extended range of composition, it is found that the variation of E_o with the appropriate composition parameter u can be expressed within the limits of experimental error by a parabolic form:

$$E_o = \alpha + \beta u + \gamma u^2 \qquad (V-3)$$

In particular, the variation along the $CuIn(S_x Se_{1-x})_2$ edge (i.e., z=0) and that along the $CuIn(Se_{1-z} Te_z)_2$ section (i.e., x=0) can be written, respectively, as

$$E_o = \delta + \varepsilon x + \zeta x^2 \qquad (V-4)$$

$$E_o = \eta + \theta z + \kappa z^2 \qquad (V-5)$$

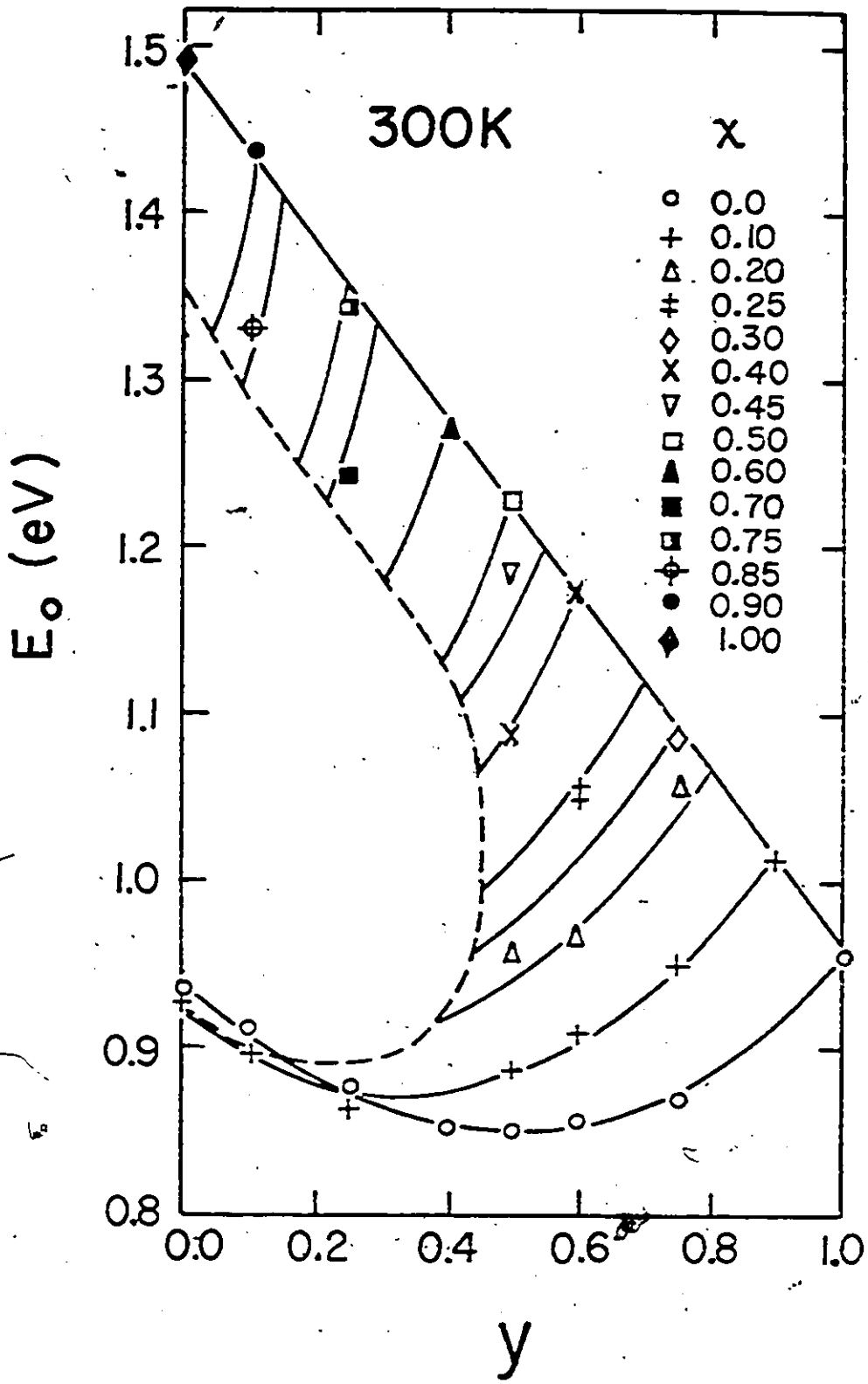

Fig. V-5 $CuIn(S_xSe_yTe_z)_2$. Variation of energy gap E_o at 300K with y for various constant values of x: Full lines are fitted curves. Dashed line is the miscibility limit.

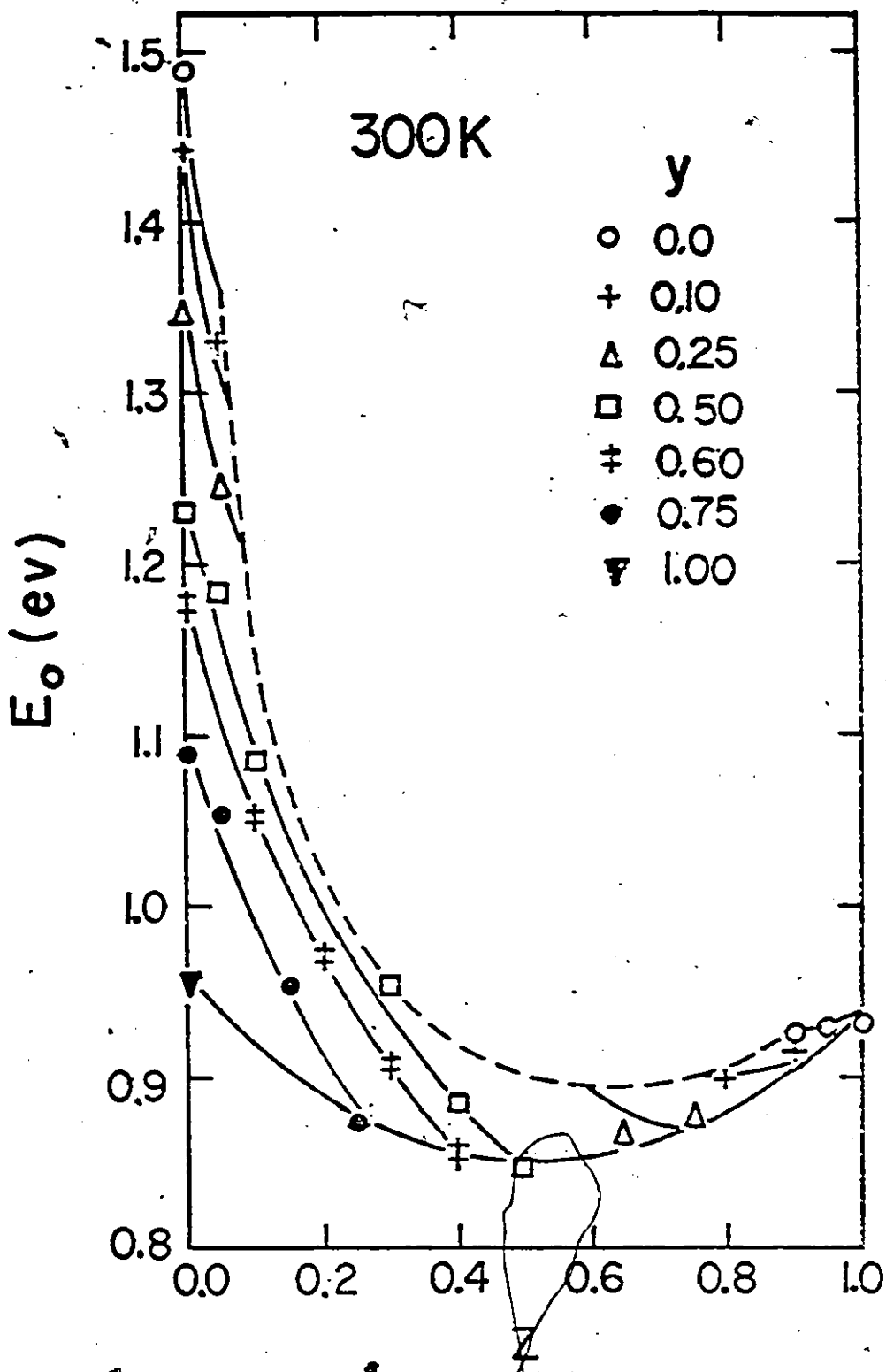

Fig. V-6 $CuIn(S_xSe_yTe_z)_2$. Variation of energy gap E_o at 300K with z for various constant values of y. Full lines are fitted curves. Dashed line, miscibility limit.

Again, for interpolation purposes, different mathematical relations will be discussed below. Firstly, the experimental data will be fitted to an empirical power series equation, and secondly comparison of the present energy gap data with predictions of an interpolation equation proposed by Williams et. al.(78W1) will be made.

Thus, to cover the general composition range, it is convenient to use the series equation

$$E_o = A + Bx + Cz + Dx^2 + Ez^2 + Fxz + Gx^2z + Hxz^2 + Jx^2z^2 \qquad (V-6)$$

since eq. V-6 reduces to eq. V-4 for the case z=0 and to eq. V-5 when x=0. Very little data can be obtained along the third edge (y=0) because of the miscibility gap and so no conditions are imposed in that case.

Values of E_o at room temperature for 33 different compositions were fitted to eq. V-6 by a standard least squares fit and the coefficients A to J determined. The resulting fitted equation is

$$E_o = 0.957 + 0.549x - 0.420z - 0.020x^2 + 0.403z^2 - 0.528xz - 1.516x^2z - 0.205xz^2 + 4.701x^2z^2 \qquad (V-7)$$

and the standard deviation of the experimental points from this equation was found to be σ =0.0098eV. The fitted curves from eq. V-7 are shown in fig. V-5 and 6 and the resulting contours of constant E_o are shown in fig. V-7.

Similar measurements and analysis were carried out at 70K for 25 different samples. The experimental values of E_o vs y for lines of constant x are shown in fig. V-8. The fitted equation in this case is

$$E_o = 1.009 + 0.457x - 0.428z + 0.023x^2 + 0.422z^2 + - 1.379xz + 1.217x^2z + 0.899xz^2 + 1.22x^2z^2 \qquad (V-8)$$

with a standard deviation in this case of σ =0.0083eV. The resultant fitted curves are shown in fig. V-8 and the calculated contours of constant E_o in fig. V-9.

If a linear temperature variation is assumed for E_o in the range 70-300K, i.e., $E_o = E_{300}(1-pT)$, values of the temperature coefficient p of the band gap can be determined for the various samples. However, the experimental scatter in E_o is not negligible compared with the change in E_o between 70 and 300K and hence there is appreciable scatter in the values of p so determined, these lying in the range 2×10^{-5} to 2.5×10^{-4} eV/K. The mean value of p over all alloy compositions investigated was found to be 1.6×10^{-5} eV/K.

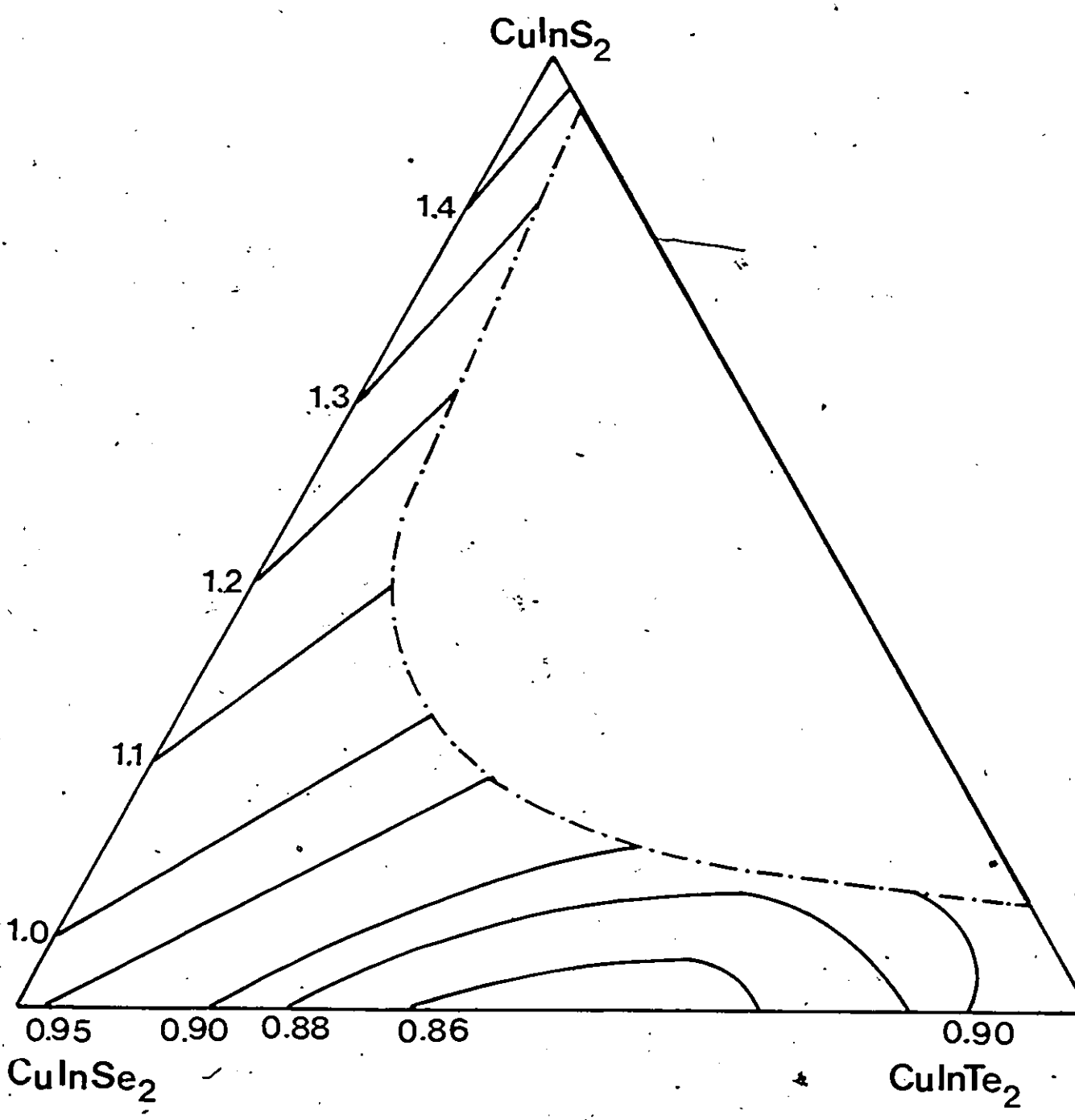

Fig. V-7 $CuIn(S_x Se_y Te_z)_2$. Isothermal section for samples annealed at 600°C and quenched to room temperature. Full line, contours of constant E_0 at 300K, values indicated in eV. Dash-dot line, miscibility limit.

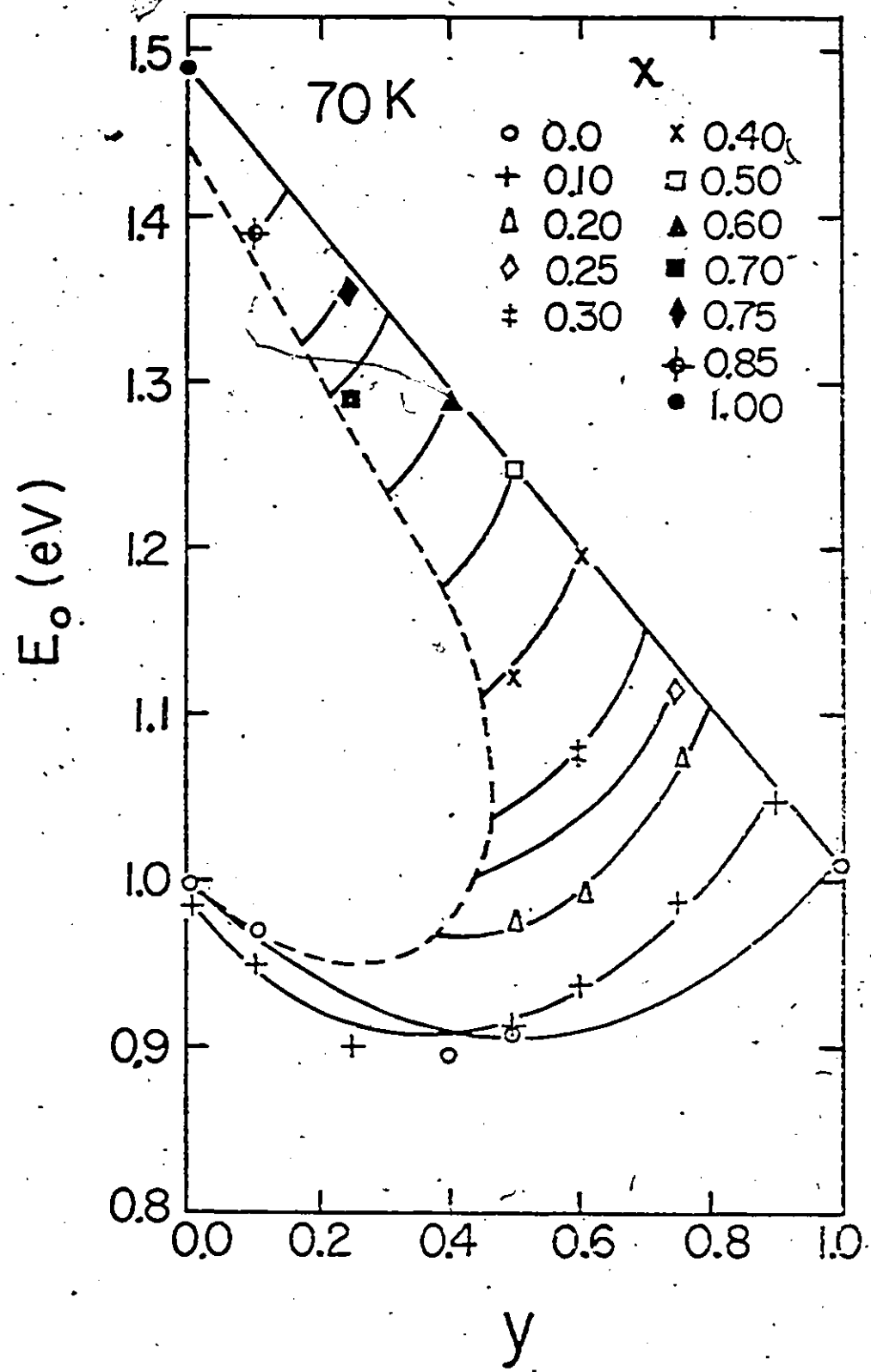

Fig. V-8 $CuIn(S_xSe_yTe_z)_2$. Variation of energy gap E_o at 70K with y for various constant values of x. Full lines, fitted curves. Dashed line, miscibility limit.

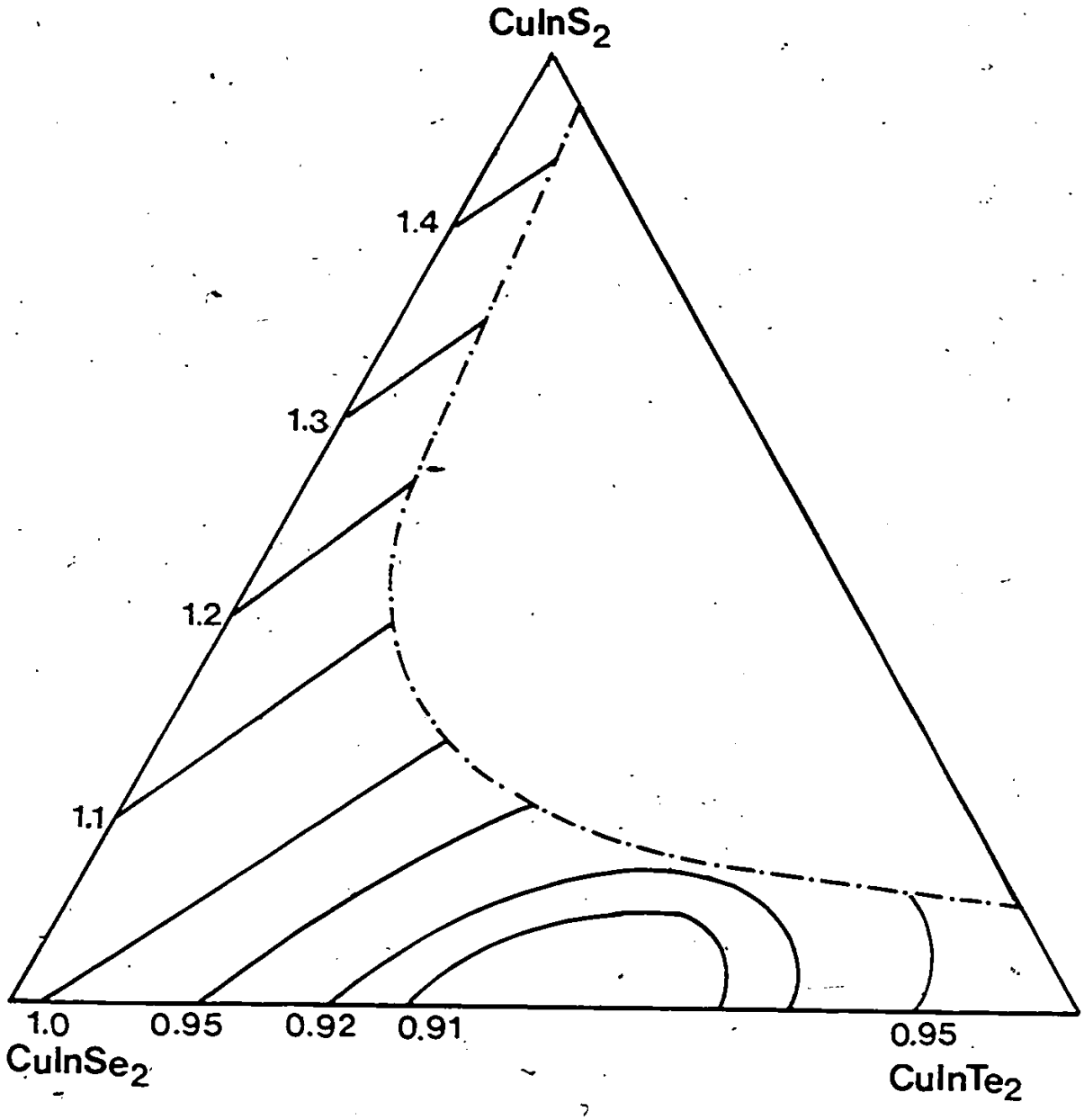

Fig. V-9 $CuIn(S_x\ Se_y\ Te_z)_2$. Isothermal section for samples annealed at 600 °C and quenched to room temperature. Full lines, contours of constant E_o at 70K, values indicated in eV. Dash-dot line, miscibility limit.

V-1d COMPARISON OF EXPERIMENTAL VALUES WITH PREDICTIONS OF AN INTERPOLATION EQUATION

For alloys of this type, Williams et al.(78W1) have proposed that parameter values for compositions inside the triangle may be predicted if the values for the three edges are known. This analysis was proposed for the case of complete solid solution in the diagram, but it is of interest to compare such predicted results with the present data for a system in which a large miscibility gap occurs.

Using the nomenclature of Williams et al., let a parameter Q have values of B_1 , B_2 , and B_3 for the compounds at the corners of the triangle and then the values along each edge may be written as $T_{ij}(s)$ where

$$T_{ij}(s) = sB_j + (1-s)B_i - s(1-s)C_{ij} \qquad (V-9)$$

Williams et al. then propose that the value of Q at any general point (xyz) is given by

$$Q(xyz) = [xyT_{12}(u)+yzT_{23}(v)+xzT_{31}(w)]/(xy+yz+xz) \qquad (V-10)$$

where

$u = (1-x+y)/2$, $v = (1-y+z)/2$

and $w = (1-z+x)/2$

For the case of the lattice parameter a, a linear variation is observed along the edges so that all C_{ij}'s are zero. Under this condition eq. V-10 reduces to the linear form of eq. V-1 and thus the equation of Williams et al. will clearly give the experimental values.

In the case of the energy gap E_o data, the room temperature experimental values show that E_o can be fitted to eq. V-9 for the S-Se edge (z=0) and for the Se-Te edge (x=0), but no result is possible for the S-Te edge (y=0) because of the very limited range of solid solubility in this case. Thus, eq. V-10 cannot be used directly to predict values of E_o at general compositions. For comparison purposes, eq. V-10 has been fitted to all of the experimental data using the present experimental values of $B_1(CuInS_2) = 1.490eV$, $B_2(CuInSe_2) = 0.954eV$, $B_3(CuInTe_2) = 0.928eV$, $C_{12} = 1.92$ 10 eV, and $C_{23} = -0.381eV$ while treating C_{31} as an adjustable parameter in the fitting process. The value of C_{31} so obtained is -1.184eV and the standard deviation for the fit is $\sigma = 0.020eV$. The values for the individual points show good agreement with the experimental values over most of the composition range but differ by up to 0.04eV for points close to the S-Te edge

(y=0) of the triangle, this being reflected in the larger value of σ in this case than in the case of the power law fit.

V-1e DISCUSSION

The results show that a miscibility gap occurs over an appreciable composition range in this alloy system. Such a gap is to be expected on the $CuIn(S_{1-z}Te_z)_2$ edge since the lattice parameters of the two compounds differ by over 12%, but the extension of the miscibility gap up to y=0.45 is perhaps larger than might be expected in terms of lattice mismatch. The linear variation of the lattice parameter a is to be compared with the parabolic variation found in a considerable range of the $(Cu_{1-x}Ag_x)(Ga_{1-y}In_y)(Se_{1-z}Te_z)_2$ alloys (84A1). It is to be noted that in that system, linear behavior occurs for alloys which are pseudocubic (i.e., c/a=2), while the deviations from linearly are seen in the cases where c/a<2.

The parabolic variation of the energy gap E_o with any chosen composition variable is typical of alloys of this type (75R1)(79C1)(84A1) and the use of a power series of the form in eq. V-6 was found to be very convenient for fitting the E_o values in the various sections of the $(Cu_{1-x}Ag_x)(Ga_{1-y}In_y)(Se_{1-z}Te_z)_2$ system. The application of

such a series in the present case is different in that the chosen variables x and z are not on orthogonal axes and also because of the presence of a large miscibility gap. It is thus of interest that a good fit to the experimental data was obtained. However, it is to be noted that the sets of parameters given in eqs. V-7 and 8 are not unique, since for the coefficients of the higher power terms, variations in one coefficient could be compensated with variations in others without making any appreciable difference to the fit or to forms of the calculated contours of constant E_o. Since the fitted equation is needed only for calculating E_o values at intermediate compositions and drawing the contours of constant E_o, etc., eq. V-7 and 8 are quite satisfactory for these purposes.

When the interpolation equation of Williams et al. is considered, it is seen that this requires a parabolic variation along the complete range of the $CuIn(S_{1-z}Te_z)_2$ edge. In eq. V-6, this implies that J must be zero and H=G. When these conditions were imposed on eq. V-6 and the power law fit made to all of the points, a much poorer fit was obtained as indicated by the increase in the standard deviation. This perhaps is to be expected, since with the very limited range of solid solution on the y=0

edge, there is less reason to expect a parabolic variation to apply. Thus, as indicated above, the equations of Williams et al. fit the data where a large area of the diagram shows single phase behavior, but give poorer values in the narrow single phase regions of the diagram with low values of y.

V-2 THE $CuGa(S_xSe_yTe_z)_2$ SYSTEM

Polycrystalline samples of 70 different composition were prepared as was described above. Initially all alloys were annealed at 700°C. However after a period of six month of annealing, the powder photographs given by most of the samples showed blurred X-ray lines, indicating that the specimens were in nonequilibrium condition for the annealing temperature and time indicated above. Thereafter the alloys were annealed in compressed powder form at a annealing temperature in the range 600 to 800°C for a period of 3 to 4 month at each temperature. Again the samples gave blurred X-ray lines, showing them to be in nonequilibrium condition, so that no quantitative results could be obtained for this alloy system.

A qualitative analysis of the X-ray powder photographs on some of the samples showed a chalcopyrite

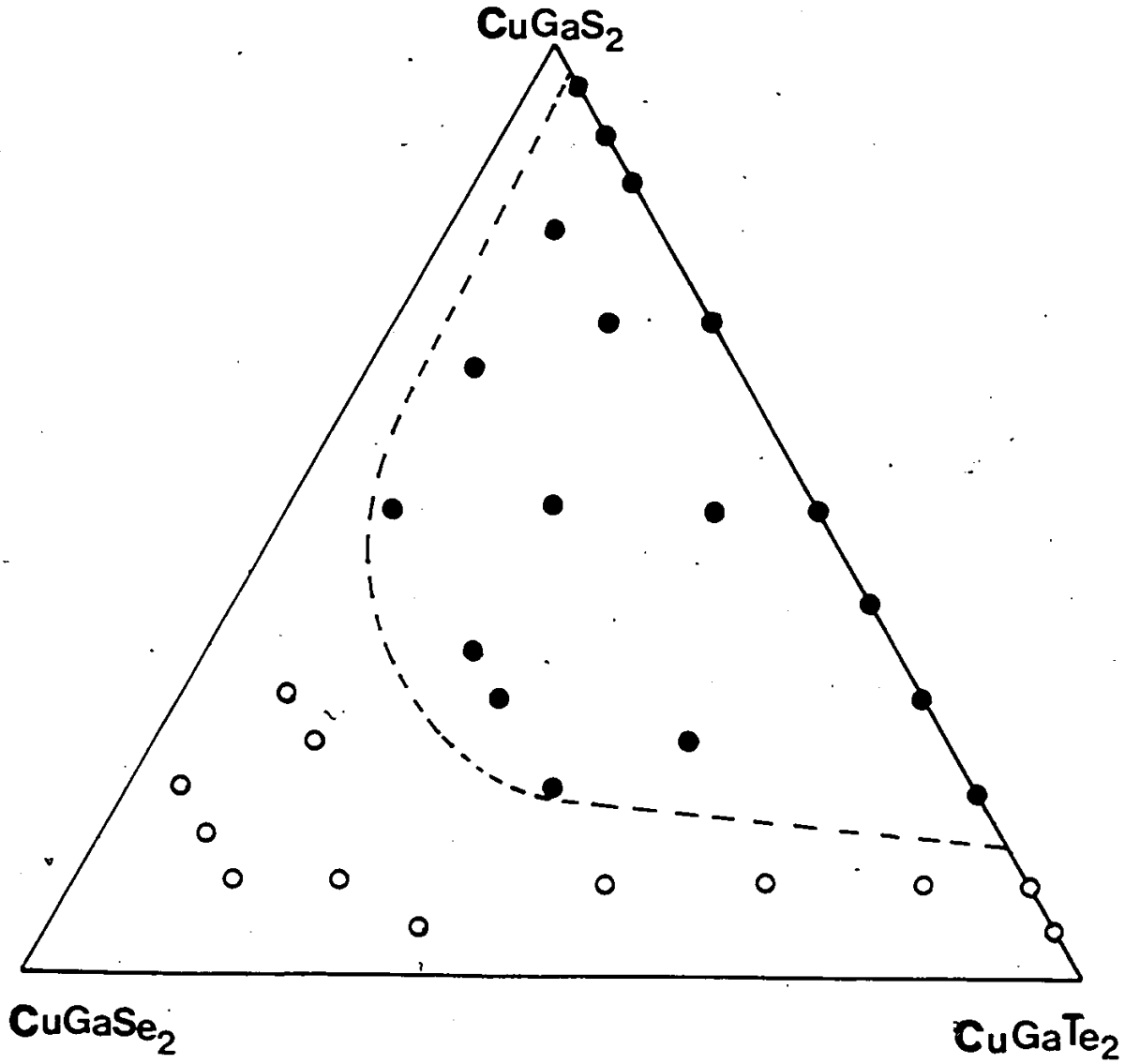

Fig. V-10 $CuGa(S_x Se_y Te_z)_2$. Isotermal section for samples annealed at 800 °C and quenched to room temperature. Open circles indicate the samples that showed blurred X-ray lines. Dark circles indicate two phase samples. Dashed line, estimated miscibility limit.

structure with c/a $\neq$ 2.0, and a miscibility gap composed of two chalcopyrite phases larger than in the case of $CuIn(S_x Se_y Te_z)_2$, which could go beyond the line y= 0.4 as is shown in fig.(V-10) which represent the estimated phase boundary for this alloy system. The dark circles represent the samples that were found to be composed of these two chalcopyrite phases. The open circles indicate the samples that although found to be single phase showed blurred X-ray lines and were in nonequilibrium conditions.

Some of the samples were prepared for optical transmission measurements, but these samples were found to be very brittle and showed a large number of pin holes. As a consequence of this, breakage of the specimen occurred when polishing down to a suitable thickness for absorption measurements, and it was apparent that single crystal work was necessary. As a first step, it was decided to grow single crystal samples of the pseudobinary section $CuGa(S_{1-y} Se_y)_2$. This work will be discussed in chapter VI.

CHAPTER VI

INVESTIGATION OF THE VALENCE BAND STRUCTURE OF THE SYSTEM $CuGa(S_{1-y}Se_y)_2$.

VI-1 INTRODUCTION

It was previously indicated in chapter II that the combined effects of the crystalline field and the spin-orbit interaction remove the triple degeneracy of the p-like valence. This gives rise to three valence to conduction band transitions E_A, E_B and E_C which are present in the chalcopyrite alloys.

As far as measurements of energy gap E_A, E_B and E_C are concerned, in the present work these have been limited to the system $CuGa(S_{1-y}Se_y)_2$, for which it is well known that a chalcopyrite single phase occurs at all compositions. Referring to previous work done on this pseudo-binary edge, earlier(80G2) normal reflectance measurements carried out on single crystal samples gave information about the position of the peaks A and B, but the position of the higher energy peak C could not be determined with any great accuracy. It was then not possible to find values of the spin-orbit and crystal

field splittings as a function of composition and temperature using the Hopfield model(60H1). A set of experimental values for these transitions as a function of alloy composition and temperature on this section are required. Thus, for the measurements described in this chapter, crystalline specimens of the pseudo-binary section $CuGa(S_{1-y}\ Se_y)_2$ were grown by iodine vapor transport technique.

In this chapter, the results of wavelength modulated reflectance measurements that have been made on these single crystal samples to determine the variation of these three transitions with composition and temperature are presented. From these values of E_A, E_B and E_C, values of the crystal field and spin-orbit splittings have been determined using the Hopfield relation. Thus the behavior of Δ_{so} and Δ_{cf} as a function of temperature has been determined. Also, the experimental data as a function of composition and temperature have been analyzed using an equation developed by K. Yoodee et. al.(84Y1).

VI-2 PREPARATION OF SAMPLES AND EXPERIMENTAL MEASUREMENTS

Initially samples of compositions y = 0, 0.25, 0.5 and 0.75 were grown by Prf. Jesus Gonzales at U.L.A (Vzla.), and given to the author for the present purposes.

The samples y = 0.75 and 0.25 were found to have damaged surfaces, probably due to the fact that the specimens were not fresh, and they may oxide in contact with air. As a result, the WMR signals were not clear and no reliable results could be obtained from these samples. However, the samples with y=0 and 0.5 presented very good WMR signals. Thus, in the present work specimens of composition y=1, 0.65, 0.75, 0.4 and 0.25 were grown by the method of static iodine vapor transport, details of the method having been given in chapter III. The surfaces of the crystals were very good and no polishing was necessary.

Small pieces of the final specimens were powdered and lattice parameter data obtained from X-ray powder photograph. These data showed that the required composition values were obtained to within $\pm$ 0.01 in y.

The sample y=0.5 was oriented by a back reflection

Laue X-ray photograph as was described in chapter IV. The results obtained from the back reflection showed that the surface of the sample corresponds to the (112) plane, and the calculations indicated that the c-axis was inclined at $35.8^{\circ} \pm 0.1^{\circ}$. Other samples were oriented and similar results were obtained. These results are in agreement with earlier data (74S1), which showed that these chalcopyrite materials have this growth-habit when they are prepared by the CVD method.

VI-3 ENERGY GAP RESULTS AND ANALYSIS

WMR measurements were made on most of the single crystal samples in the temperature range 10 - 300 K as was described in chapter IV. Figs. (VI-1) to (VI-4) show WMR curves as a function of wavelength for the samples y=1, 0.65, 0.5 and 0.25 at various temperatures. From such curves, the values of E_A, E_B and E_C were taken to be at the peaks. For each value of y, the energy value of each peak was plotted as a function of temperature and the resulting variations of E_A, E_B and E_C are shown in figs.(VI-5) to (VI-8). The variation of these transitions as a function of 1-y at 20 K is shown in fig.(VI-9).

As was done by earlier workers (82G1), the present experimental data were fitted as a function of temperature

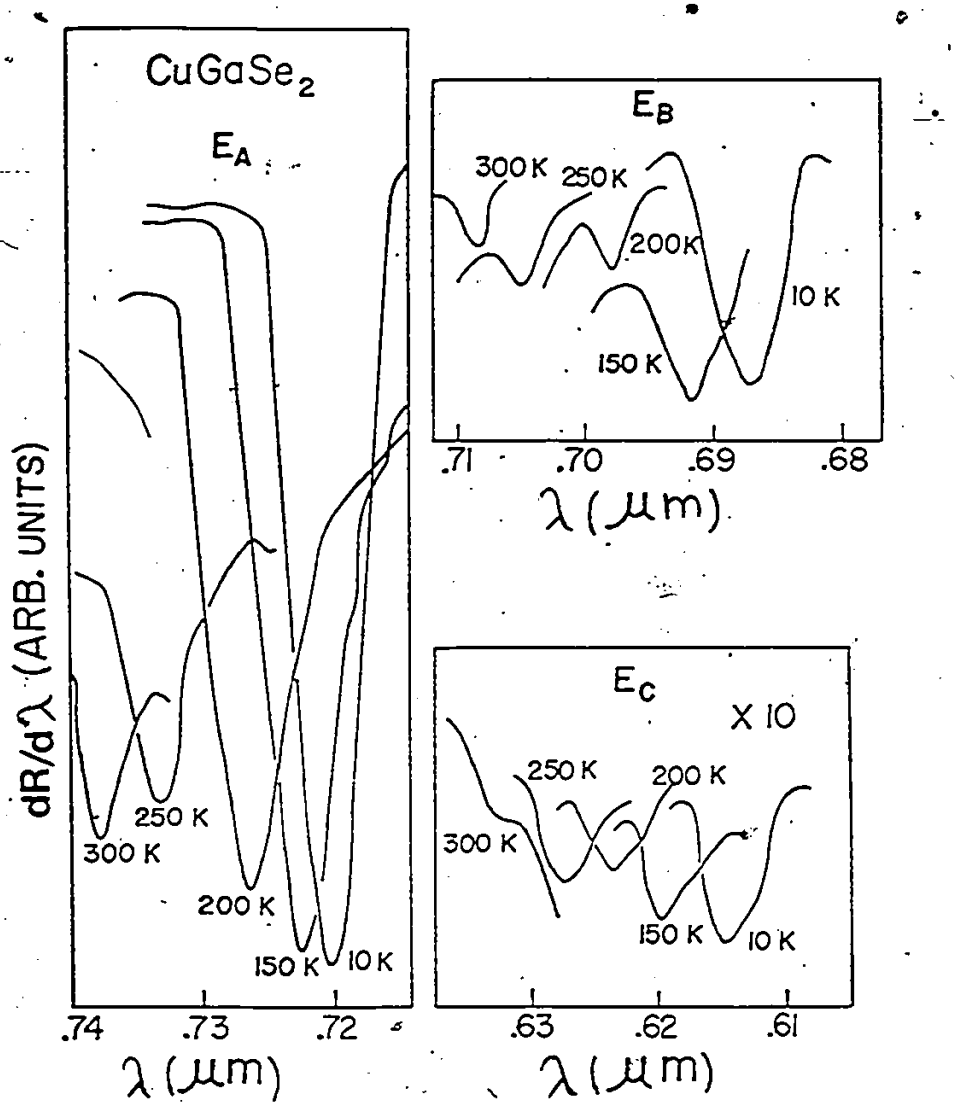

Fig. VI-1 $CuGa(S_{1-y}Se_y)_2$. Variation of $dR/d\lambda$ with photon wavelength λ for the sample y=1 at the temperatures indicated. Values of temperature indicated in K. E_A, E_B and E_C are Γ -point valence band to conduction band transitions.

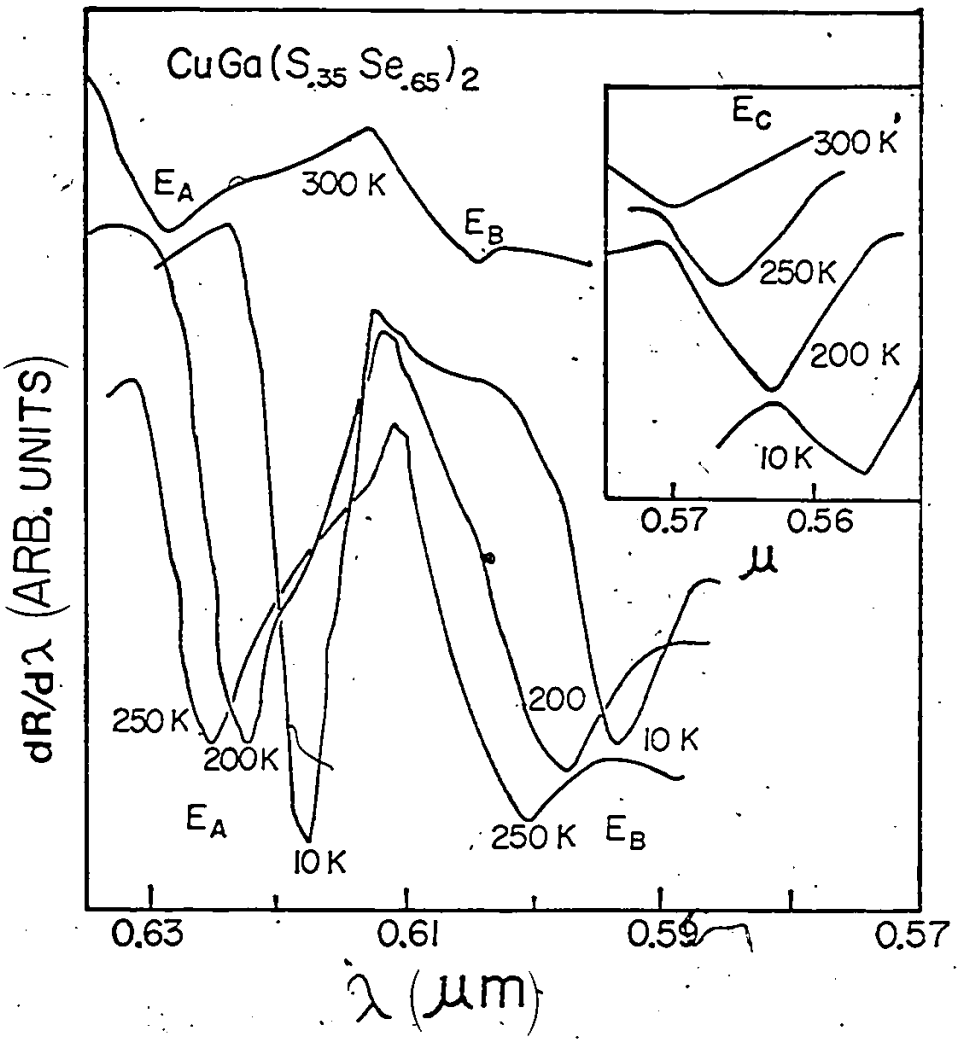

Fig. VI-2 $CuGa(S_{1-y}Se_y)_2$. Variation of dR/dλ with photon wavelength λ , for the sample y=0.65 at the temperatures indicated, values given in K. E_A, E_B and E_C are Γ-point valence band to conduction band transitions.

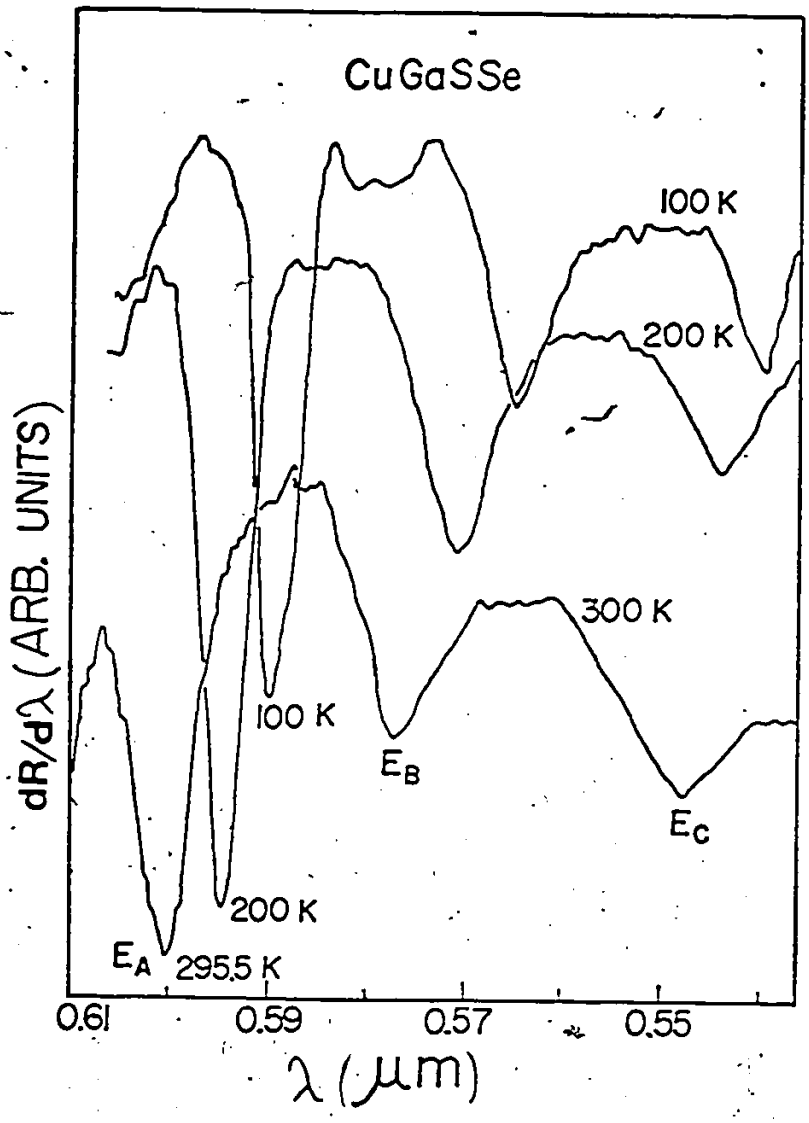

Fig. VI-3 $CuGa(S_{1-y}Se_y)_2$. Variation of dR/dλ with photon wavelength λ, for the sample y=0.5 at the temperatures indicated, values given in K. E_A, E_B and E_C are Γ-point valence band to conduction band transitions.

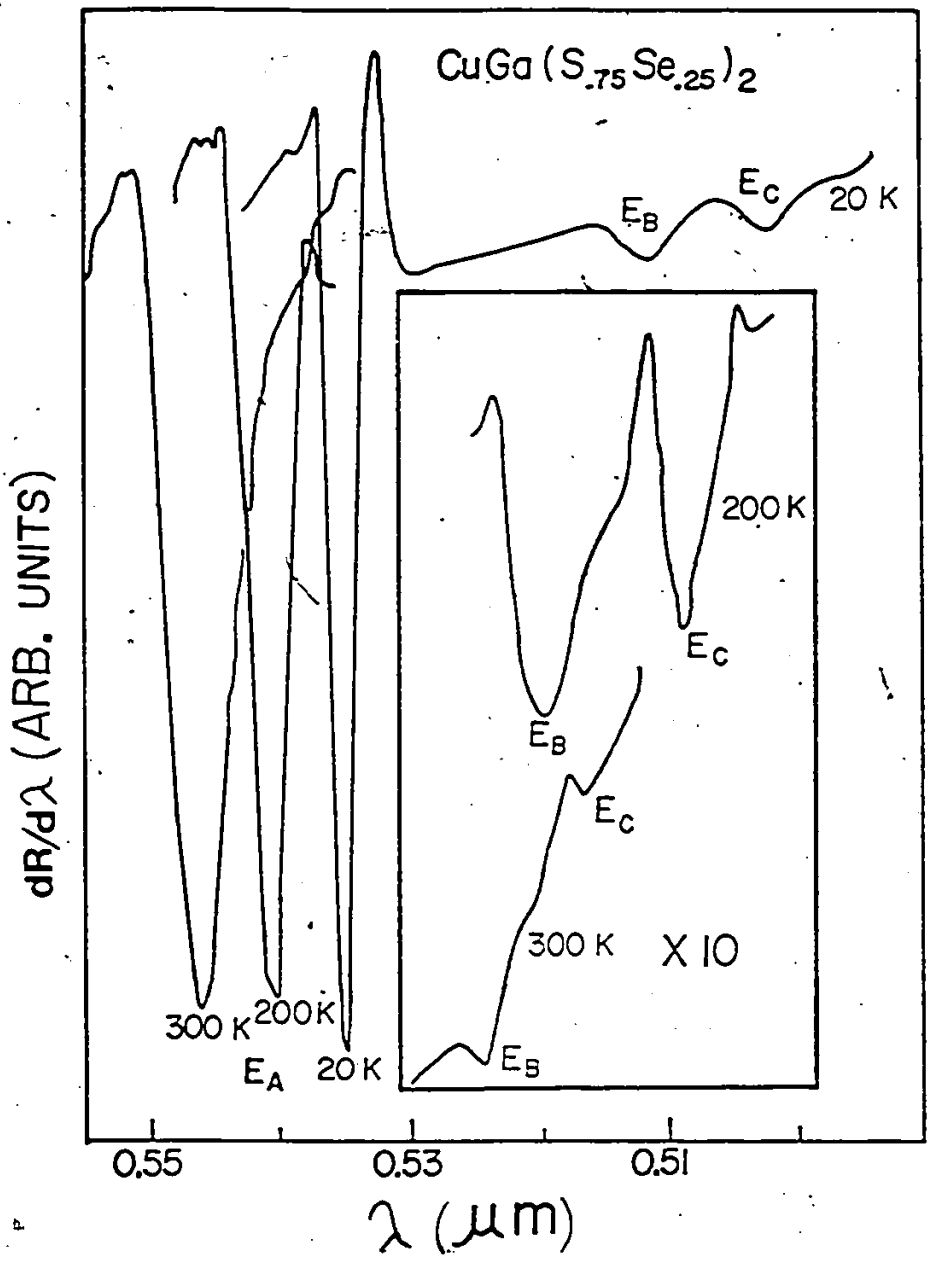

Fig. VI-4 $CuGa(S_{1-y}Se_y)_2$. Variation of $dR/d\lambda$ with photon wavelength λ, for the sample y=0.25 at the temperatures indicated. values given in K. E_A, E_B and E_C indicate Γ-point valence band to conduction band transitions.

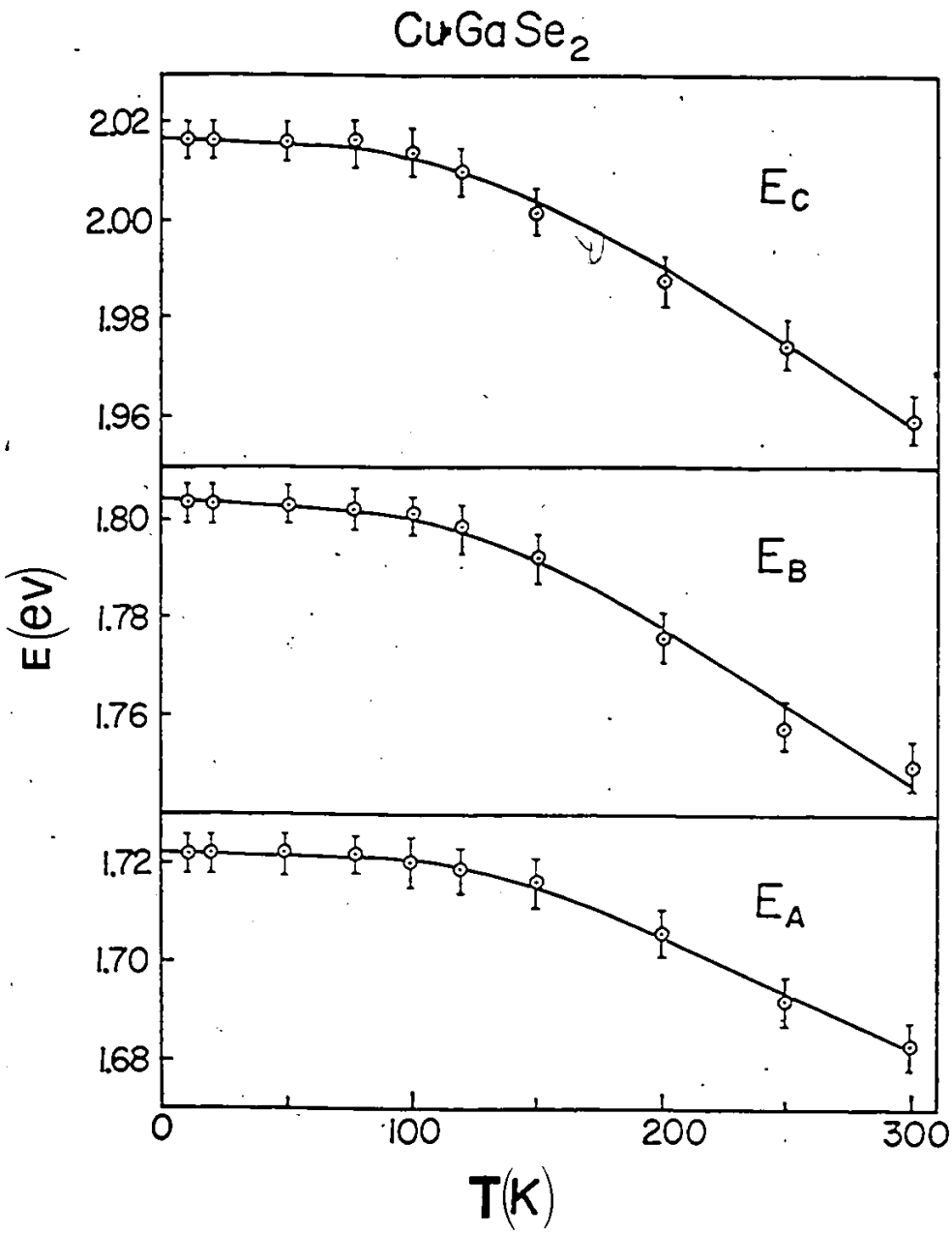

Fig. VI-5 $CuGa(S_{1-y}Se_y)_2$. Variation of Γ-point band gaps E_A, E_B and E_C with temperature, for the sample y=1.0. The solid lines are the fitted curves.

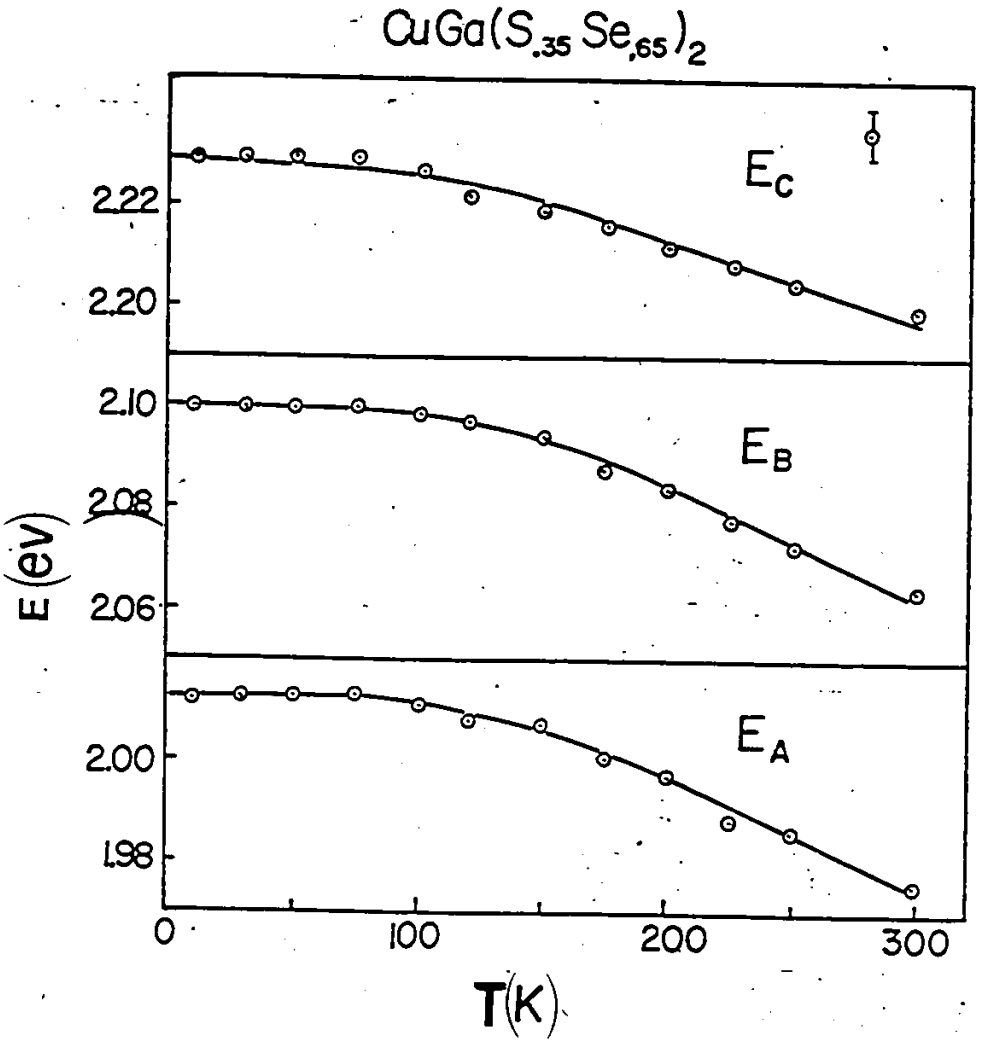

Fig. VI-6 $CuGa(S_{1-y}Se_y)_2$. Variation of Γ-point band gaps E_A, E_B and E_C with temperature, for the sample y=0.65. The solid lines are the fitted curves.

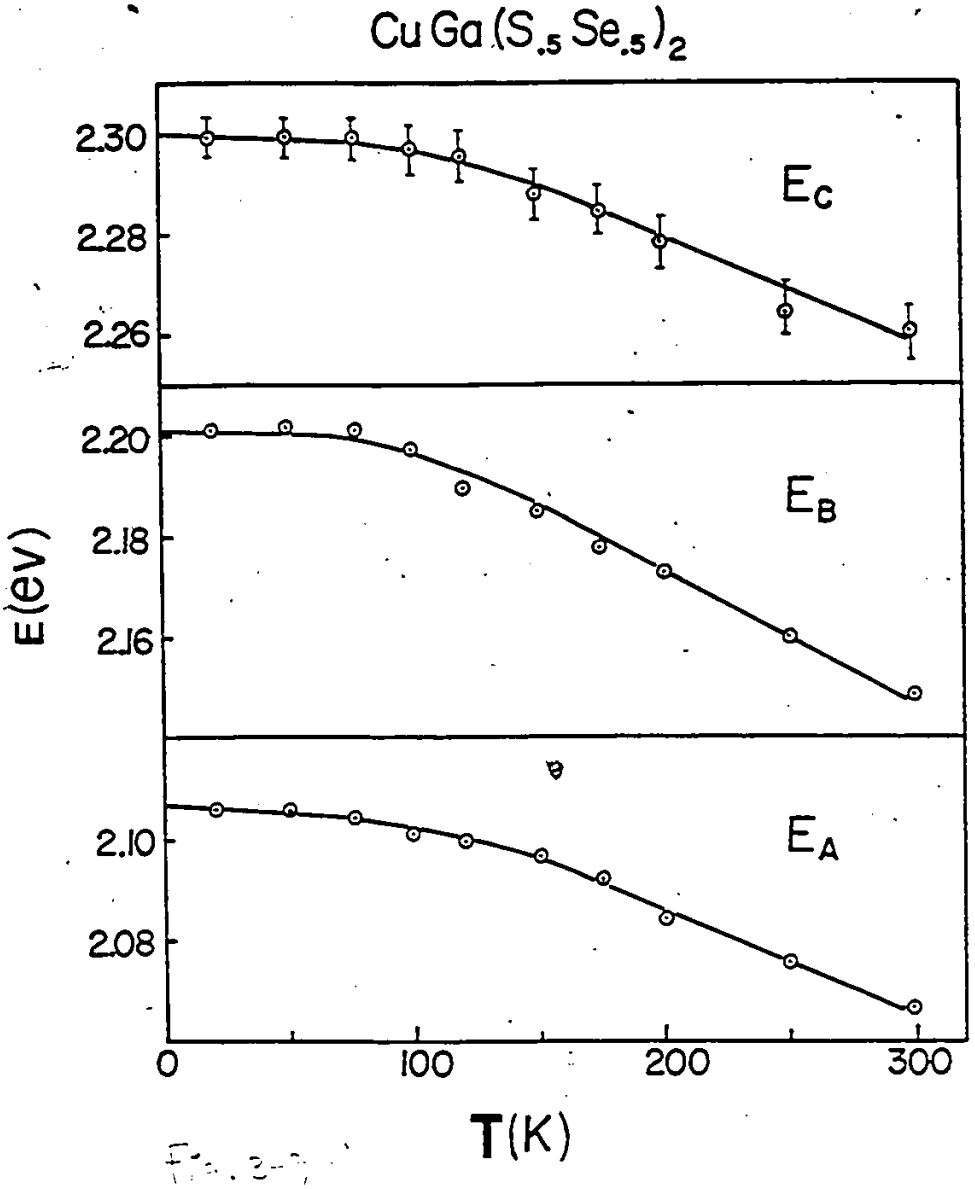

Fig. VI-7 $CuGa(S_{1-y}Se_y)_2$. Variation of Γ-point band gaps E_A, E_B and E_C with temperature, for the sample y=0.5. The solid lines are the fitted curves.

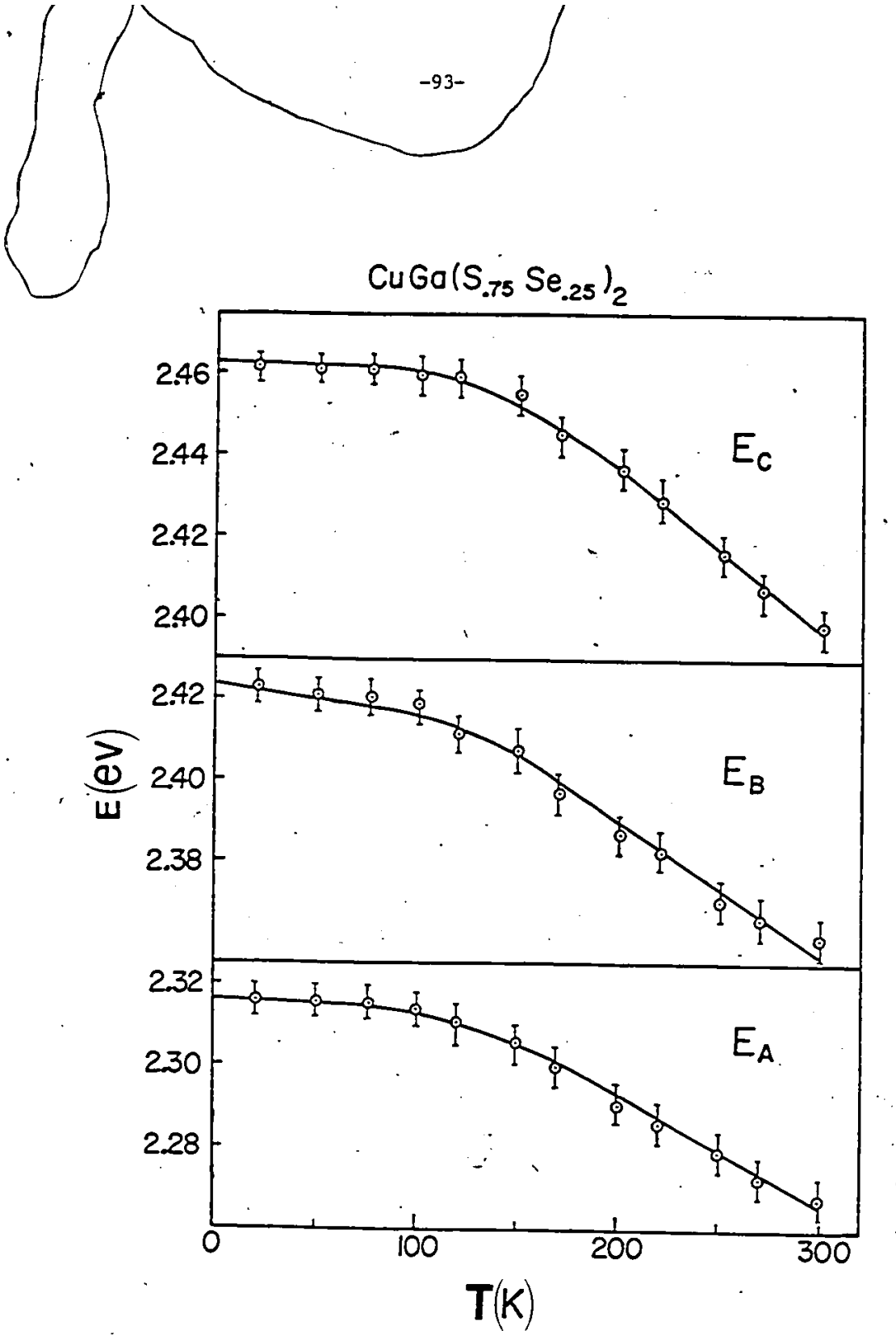

Fig. VI-8 $CuGa(S_{1-y}Se_y)_2$. Variation of Γ-point band gaps E_A, E_B and E_C with temperature, for the sample y=0.25. The solid lines are the fitted curves.

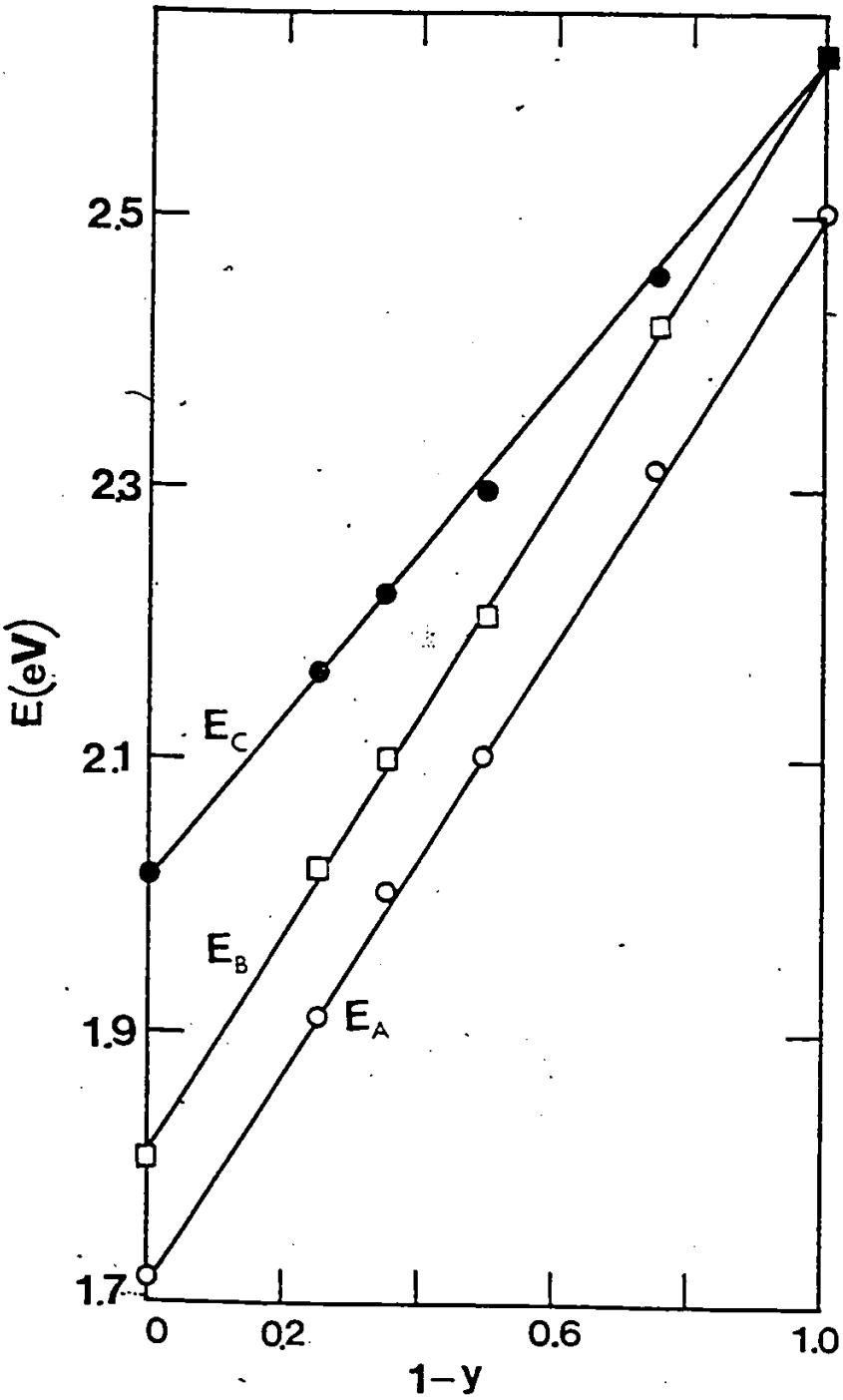

Fig. VI-9 $CuGa(S_{1-y}Se_y)_2$. Variation of Γ-point transitions E_A, E_B and E_C with composition 1-y at 20K.

to a simple Manoogian-Leclerc equation of the form

$$E_o - E(T) = UT^s + V\theta(\coth \theta/2T - 1) \qquad \text{(VI-1)}$$

where U, V, s and θ are constants independent of T. As has been shown previously (80G2), the main contribution to the change in the energy gap values is from the $V\theta$ dynamic term, the UT^s static term contributing only a small fraction over most of the temperature range. An empirical relation between θ and the molecular weight of the compounds(84M1) showed that the values of θ for these alloys could be taken to vary linearly between 360K for y=0 to 290K for y=1.0. Thus, the set of curves for each value of y were fitted to give values of U and V, and these values are summarized in table VI-1, and resulting curves are shown as solid lines in figs. VI-5 to VI-8.

The use of the two polarization orientations can give useful information since, as is shown in fig.(II-6) for these noncubic materials, the three valence to conduction band transitions are polarization dependent. Thus it is necessary to determined the valence band symmetry arrangement before relations II-1 and II-2 of chapter II can be applied.

In the case of the sample y = 0.5, which was

TABLE VI-1. Values of U, V and θ for various samples obtained using eq.(VI-1). A, B and C indicate the valence band to conduction band transitions.

y=1.0 θ =290K s=2/3

	A	B	C
U(eV/K$^{2/3}$)	$-1.28\ 10^{-4}$	$-9.39\ 10^{-5}$	$-7.76\ 10^{-5}$
V(eV/K)	$1.25\ 10^{-4}$	$1.71\ 10^{-4}$	$1.70\ 10^{-4}$

y=0.75 θ=312K s=2/3

	A	B	C
U(eV/K$^{2/3}$)	$-2.21\ 10^{-5}$	$-7.43\ 10^{-6}$	$4.62\ 10^{-5}$
V(eV/K)	$1.04\ 10^{-4}$	$1.13\ 10^{-4}$	$1.13\ 10^{-4}$

y=0.65 θ =314K s=2/3

	A	B	C
U(eV/K$^{2/3}$)	$-1.22\ 10^{-4}$	$-6.21\ 10^{-5}$	$9.17\ 10^{-5}$
V(eV/K)	$1.25\ 10^{-4}$	$1.17\ 10^{-4}$	$8.36\ 10^{-5}$

y=0.5 θ =324K s=2/3

	A	B	C
U(eV/K$^{2/3}$)	$7.85\ 10^{-5}$	$2.37\ 10^{-4}$	$-1.65\ 10^{-6}$
V(eV/K)	$1.14\ 10^{-4}$	$1.38\ 10^{-4}$	$1.25\ 10^{-4}$

y=0.25 θ =340K s=2/3

	A	B	C
U(eV/K$^{2/3}$)	$-1.01\ 10^{-5}$	$1.77\ 10^{-4}$	$-2.59\ 10^{-4}$
V(eV/K)	$1.58\ 10^{-4}$	$1.86\ 10^{-4}$	$2.32\ 10^{-4}$

oriented as indicated above, an H.R. polarizer was placed in the beam between the monochromator and the sample so that the WMR spectrum could be determined for different polarizations of the incident light. Fig. (VI-10) displays the WMR results obtained with $E \perp z$ and $E \| z$ for the sample y=0.5 at 20K. It reveals that E_A is stronger for parallel than for perpendicular polarization, E_B and E_C are very strong for $E \perp z$ and weak for $E \| z$. Comparing the above results with those of fig.(II-6) (chapter II), it is seen that the $\Gamma_7 \Gamma_6 \Gamma_7$ valence band ordering gives the closer resemblance to the experimental data. However due to the (112) orientation discussed earlier, the parallel configuration is only nominal and in this case one-third of the incident intensity is in fact polarized $\perp$ to the z-axis. This accounts for the appearance of a small peak B for $E \| z$ even though $\Gamma_6 \longrightarrow \Gamma_6$ transitions are allowed only for $E \perp z$. This valence band ordering has been found in most of the I-III-VI_2 including the case of $CuGaSe_2$ which is of direct concern here. Hence it is concluded that in the alloys investigated in the present chapter the valence band ordering is $\Gamma_7 \Gamma_6 \Gamma_7$.

Using the above result for the valence band ordering, equations II-1 and II-2 and the values of E_A, E_B and E_C obtained from the Manoogian fit, values of Δ_{so} and Δ_{cf} were calculated. The results so obtained for the

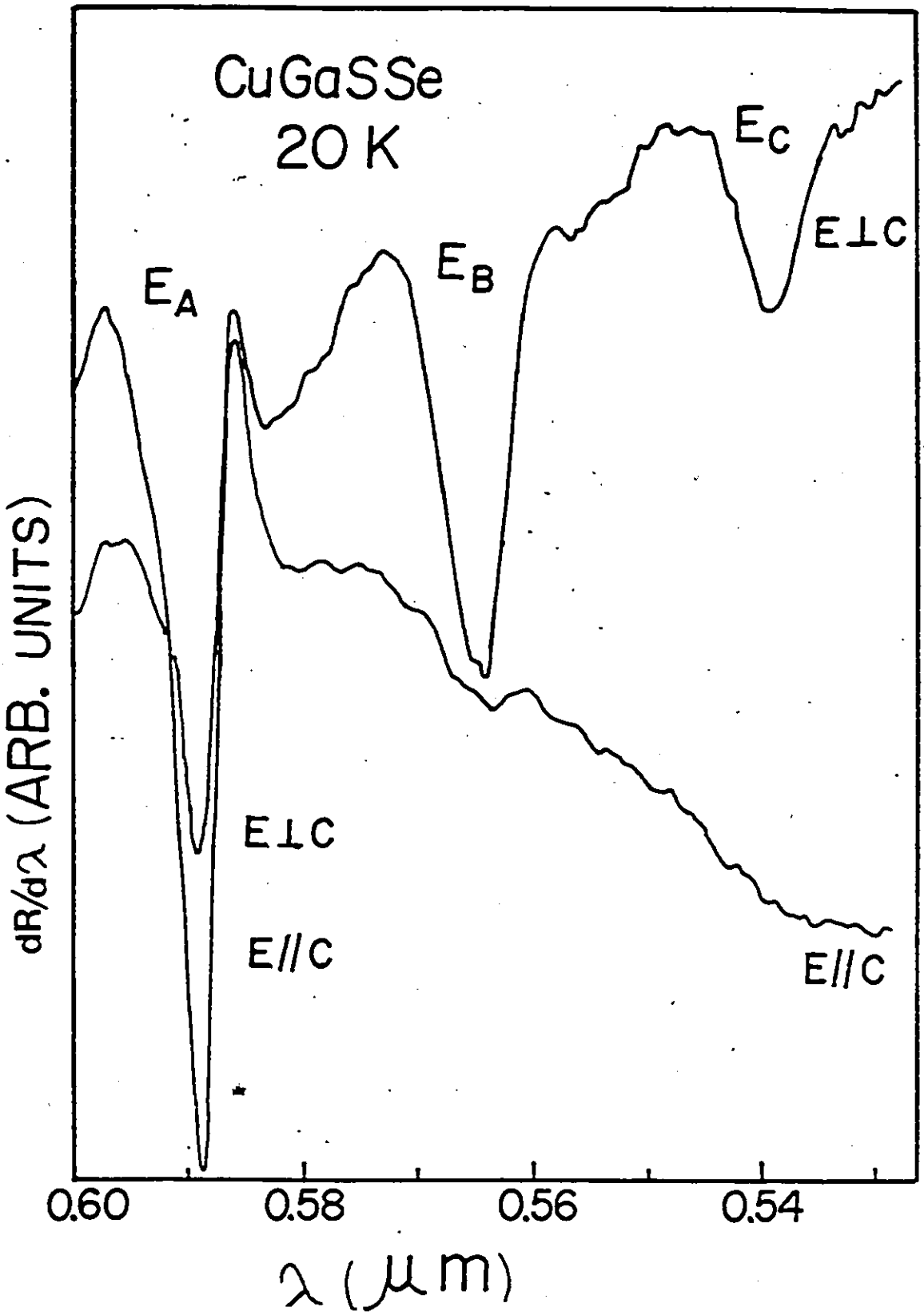

Fig. VI-10 $CuGa(S_{1-y}Se_y)_2$. Variation of dR/dλ with photon wavelength λ at 20K for light polarized parallel and perpendicular to the c axis of the sample y=0.5. E_A, E_B and E_C are Γ-point valence band to conduction band transitions.

samples y = 1.0 and 0.5 are presented in figs.(VI-11) and (VI-12) respectively, and in fig.(VI-13) the variations of spin-orbit and crystal field splitting with 1-y at 20K are shown.

In order to apply eqs.(II-3) to (II-6) to the present results, it is assumed that Δ^p_{so}, Δ^d_{so}, b_p and b_d are temperature independent, and that

$$\Delta^p_{so} = \frac{G_p}{16}\{\Delta^{Cu}_p + 3\Delta^{Ga}_p + 12\ (1-y)\ \Delta^S_p + y\ \Delta^{Se}_p\} \qquad \text{(VI-2)}$$

where Δ^{Cu}_p etc. are the atomic p spin-orbit splittings of the elements and G_p is an enhancement factor for the solid. For both zincblende(69C1) and chalcopyrite(71P1) structures, G_p has been taken to be 29/20. It is assumed also that the d contribution in Δ^d_{so} is due to the copper atoms only, the other d levels being too deep to contribute. Under these conditions, we can write(67S1)

$$\Delta^d_{so} = (29/20)\Delta^d_{so}(Cu) = -0.224\ eV. \qquad \text{(VI-3)}$$

With these values of Δ^p_{so} and Δ^d_{so} used with the experimental values of Δ_{so}, values of α as a function of temperature can be calculated from eq. II-3. In fig.(VI-14) the values of $(1-\alpha)$ as a function of composition at 20 K are shown.

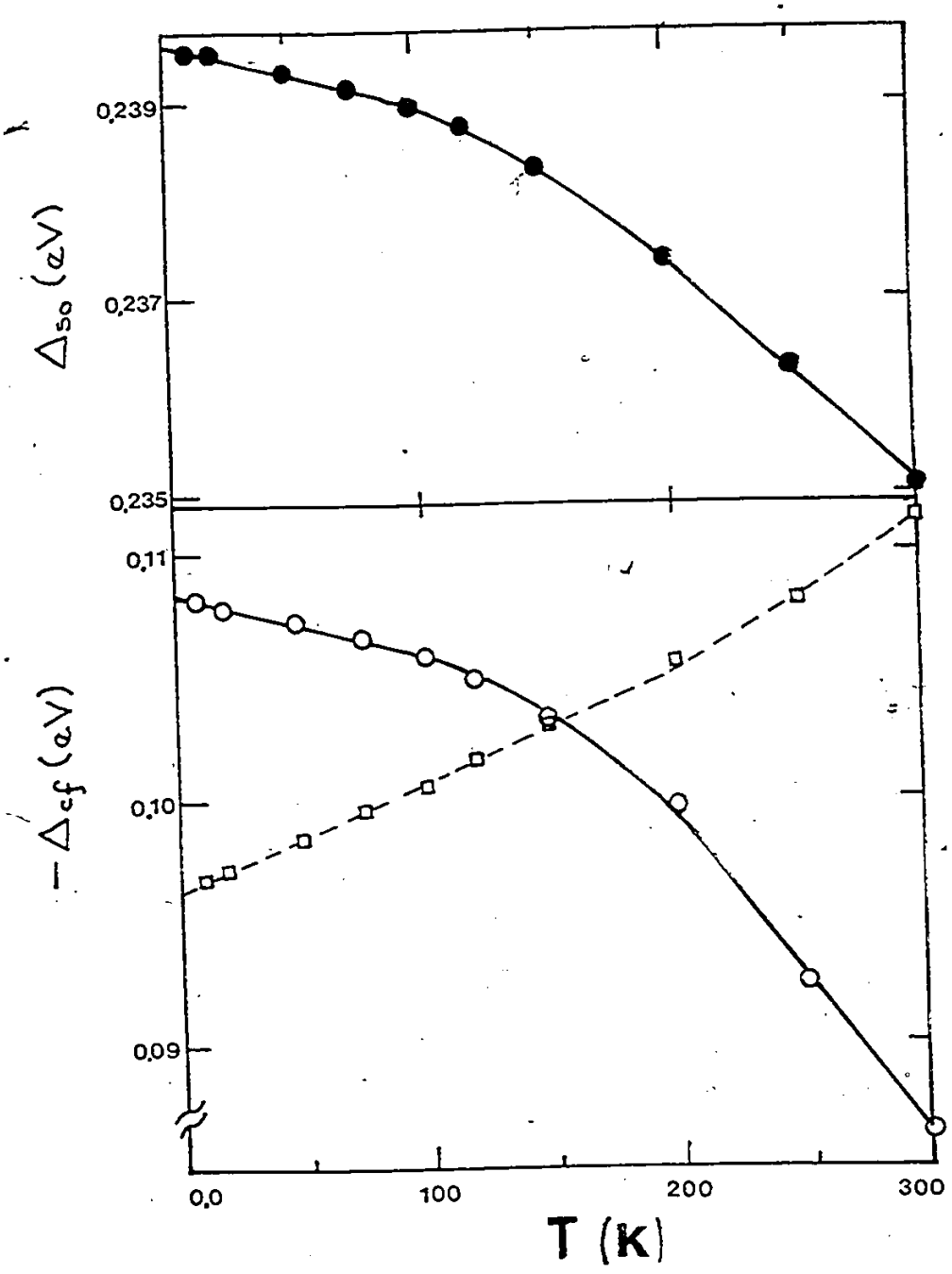

Fig. VI-11 $CuGa(S_{1-y}Se_y)_2$. Variation of spin-orbit splitting Δ_{so} (solid circles) and crystal field splitting Δ_{cf} (open circles) as a function of temperature T, for the sample y=1.0. The squares and the dash line indicate the values of crystal field splitting obtained using values of β from X-ray diffraction work.

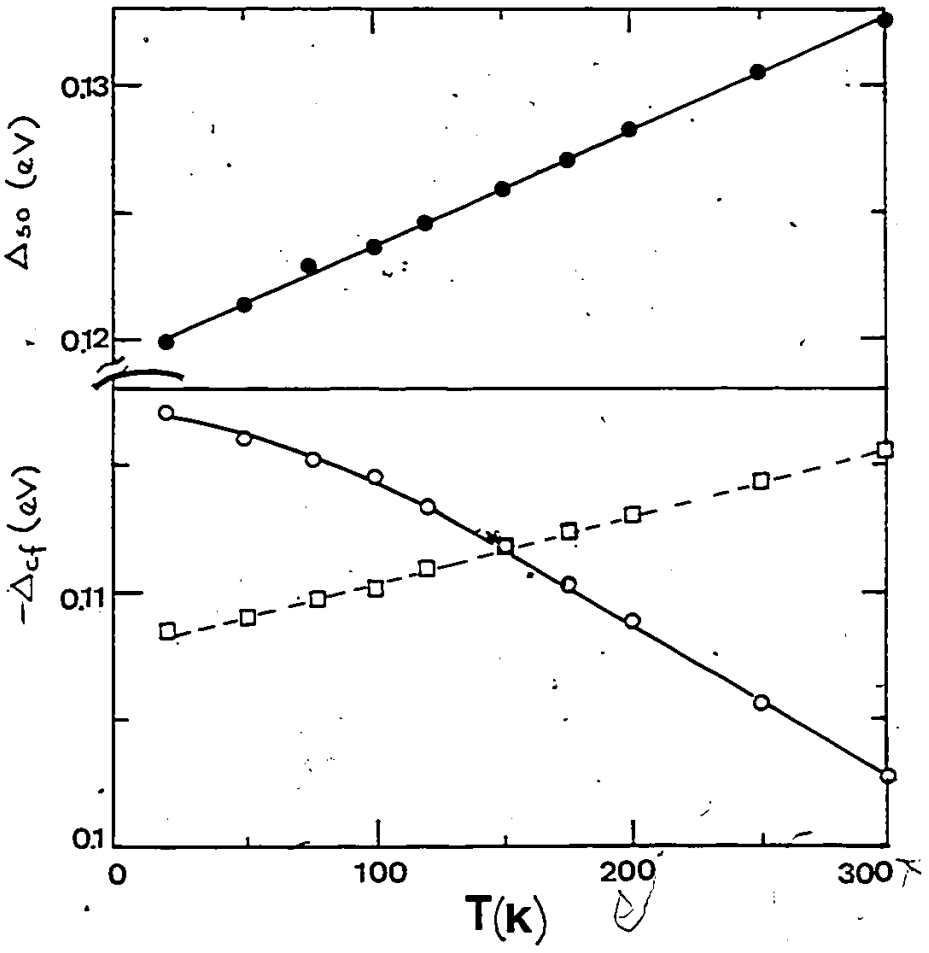

Fig. VI-12 $CuGa(S_{1-y}Se_y)_2$. Variation of spin-orbit splitting (solid circles) and crystal field splitting Δ_{cf} (open circles) as a function of temperature, for the sample y=0.5. The squares and the dashed line indicate the values of crystal field splitting obtained using values of β from X-ray diffraction.

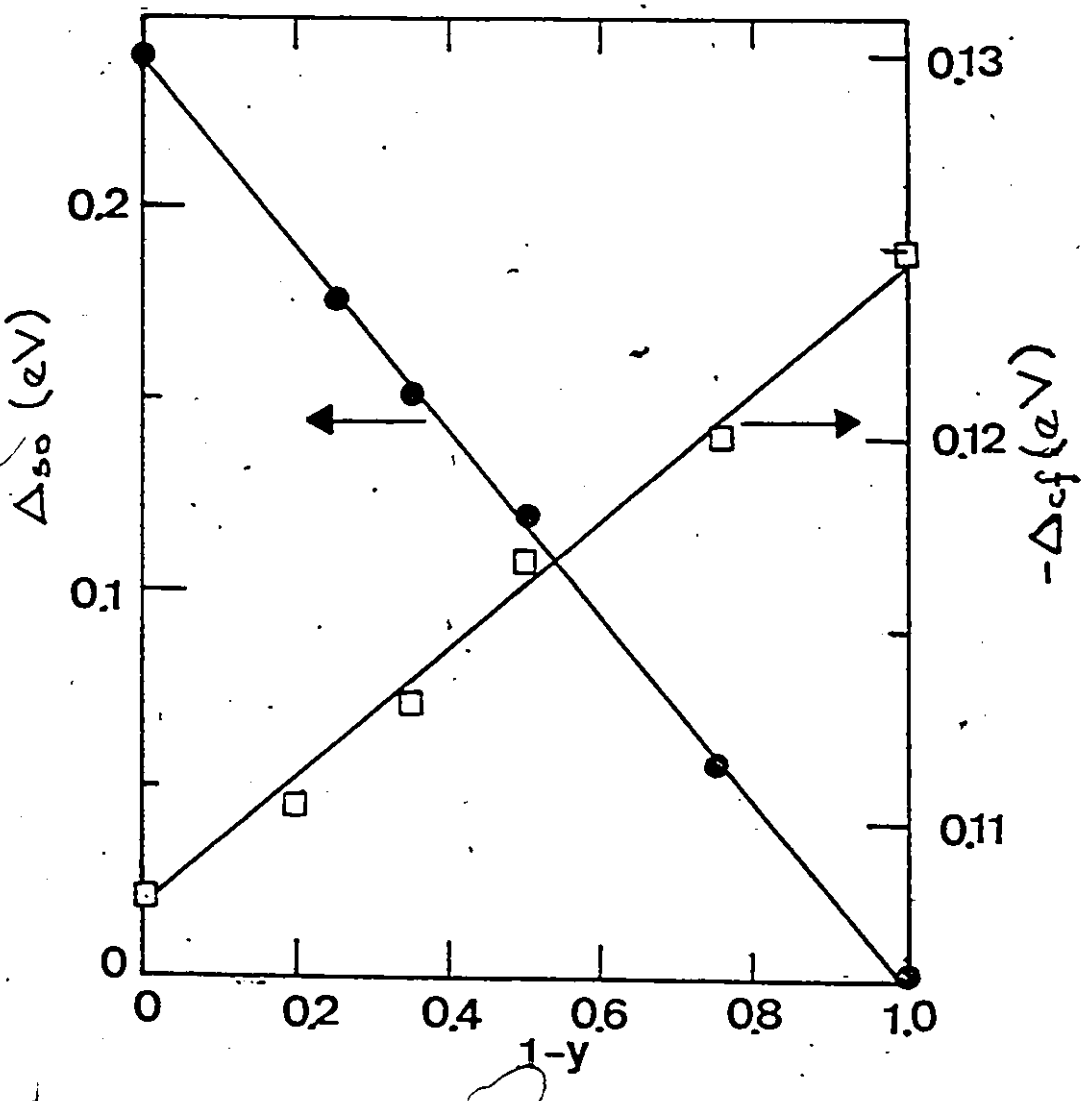

Fig. VI-13 $CuGa(S_{1-y}Se_y)_2$. Variation of spin-orbit Δ_{so} (solid circles) and crystal field splitting Δ_{cf} (squares) with composition 1-y.

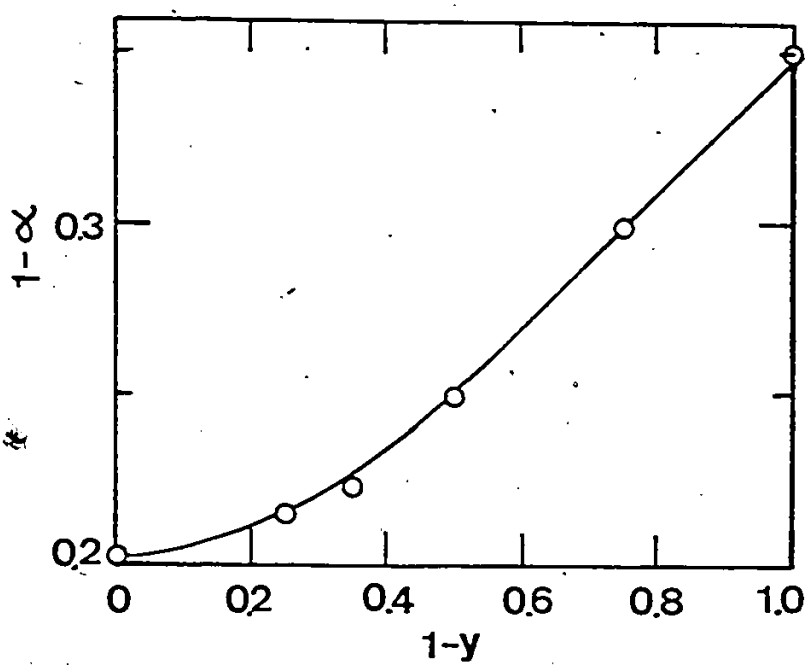

Fig. VI-14. $CuGa(S_{1-y}Se_y)_2$. Variation of d-like character 1-α with composition 1-y at 20K.

Now, assuming that the variation of the tetragonal distortion (2-c/a) may be taken as linear with temperature, the crystal field splitting may be represented, using eqs. II-5 to II-6, by the form

$$\Delta_{cf} = \{ \alpha\, b_p + (1-\alpha)\, b_d \} \{ \frac{3}{2} (2-c/a)_{300} + \beta(T-300) \} \qquad \text{(VI-4)}$$

where β is related to the temperature coefficient β' of the ratio c/a. Values of β for $CuGaS_2$ and $CuGaSe_2$ have been reported in the literature (79Y1) (80B1) from X-ray analysis, and it is assumed that the variation of β is linear with composition between 2.82×10^{-5}/K for $CuGaS_2$ and 2.32×10^{-5}/K for $CuGaSe_2$. A least squares fit to eq. (VI-4), with values of b_p in the range -0.8 to 0, was made in order to give the value for b_d from the experimental values of Δ_{cf}. It was found that, in all cases, eq. (VI-4) gave a poor fit to the values of Δ_{cf} as a function of temperature, as is illustrated in figs. (VI-11) and (VI-12). When the value of β was treated as an additional unknown parameter, it was found that, in practically all cases, a reasonable fit could be obtained but this fit gave a negative value for β, in disagreement with the known positive values from X-ray analysis given above.

In view of these results, the present experimental data were analyzed using a model proposed very recently by

K. Yoodee, J. C. Woolley and V. Sa-yakanit (YWS) (84K1). The model analyzes the effect of p-d hybridization on the uppermost valence band at the Γ-point of I-III-VI_2 chalcopyrite compounds. They consider the interaction between the p Γ_{15}(p) and the d Γ_{15}(d) bands. There are two important parameters in that model viz., the energy separation E between p- an d- levels before hybridization and the interaction matrix element M which contains the p-d hybridization interaction potential between these levels. Thus the valence band splitting within the context of that model are given by

$$E_o(\Gamma_6) = \lambda_o + \gamma_o \frac{\Delta^p_{cf}}{3} + (1-\gamma_o)\frac{\Delta^p_{cf}}{3} \qquad \text{(VI-5)}$$

$$E_{1,2}(\Gamma_7) = \frac{1}{2}\{\lambda_1+\lambda_2 - \frac{\Delta^p_{cf}}{3}\gamma_1 - (1-\gamma_1)\frac{\Delta^p_{cf}}{3}\} \pm \qquad \text{(VI-6)}$$

$$\pm\frac{1}{2}\left\{\left[\lambda_1 - \lambda_2 - \gamma_1\frac{\Delta^p_{cf}}{3} - (1-\gamma_1)\frac{\Delta^d_{cf}}{3}\right]^2 + \right.$$

$$\left. + \frac{8}{9}\left[\left[(\gamma_1\gamma_2)^{1/2}\Delta^p_{cf} + \left[(1-\gamma_1)(1-\gamma_2)\right]^{1/2}\Delta^p_{cf}\right]\right]^2\right\}^{1/2}$$

where $E_o(\Gamma_6)$ and $E_{1,2}(\Gamma_7)$ are as indicated in fig. (VI-15), after ref.(84K1), and where

$$\lambda_o = \lambda_1 = \frac{1}{2}\{\frac{\Delta^p_{so}}{3} - E - |\frac{\Delta^d_{so}}{3}|\} + \frac{1}{2}\{\left[\frac{\Delta^p_{so}}{3} + E + \frac{|\Delta^d_{so}|}{3}\right]^2 + 4M^2\}^{1/2}$$

$$\lambda_2 = \frac{1}{2}\{-\frac{2}{3}\Delta^p_{so} - E - \frac{2}{3}|\Delta^d_{so}|\} + \frac{1}{2}\{\left[\frac{2}{3}\Delta^p_{so} + E - \frac{2}{3}|\Delta^d_{so}|\right]^2 + 4M^2\}^{1/2}$$

$$\lambda_3 = \frac{1}{2}\{-\frac{2}{3}\Delta^p_{so} - E - \frac{2}{3}|\Delta^p_{so}|\} - \frac{1}{2}\{\left[-\frac{2}{3}\Delta^p_{so} + E - \frac{2}{3}|\Delta^d_{so}|\right]^2 + 4M^2\}^{1/2}$$

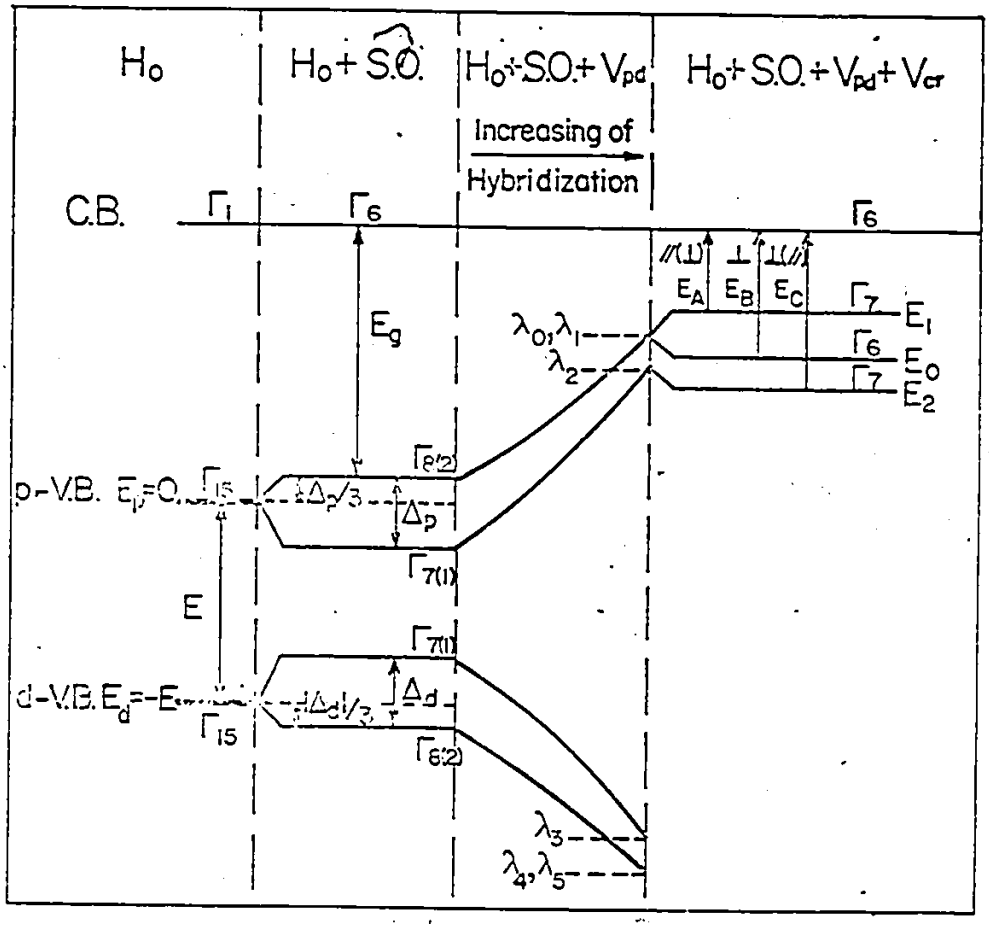

Fig. VI-15 Energy band structure at the Γ-point of a chalcopyrite crystal derived from the Γ_{15} (p) and Γ_{15} (d) bands of a zincblende crystal, after reference 84K1.

$$\lambda_4 = \lambda_5 = \frac{1}{2}\left\{\frac{\Delta^p_{so}}{3} - E - \frac{|\Delta^d_{so}|}{3}\right\} - \frac{1}{2}\left\{\left[\frac{\Delta^p_{so}}{3} + E + \frac{|\Delta^d_{so}|}{3}\right]^2 + 4M^2\right\}^{1/2}$$

$$\gamma_0 = \gamma_1 = 1/\{1+M^2/(\lambda_1 + E + \frac{|\Delta^d_{so}|}{3})^2\}$$

$$\gamma_2 = 1/\{1+M^2/(\lambda_2 + E - \tfrac{2}{3}|\Delta^d_{so}|)^2\} \qquad \text{(VI-7)}$$

$$\gamma_3 = 1 - 1/\{1+M^2/(\lambda_2 + \tfrac{2}{3}\Delta^p_{so})^2\}$$

$$\gamma_4 = \gamma_5 = 1 - 1/\{1+M^2/(\lambda_5 - \frac{\Delta^p_{so}}{3})^2\}$$

The YWS model was applied to a large number of I-III-VI_2 compounds (84Y1), and it was found that for all of the I-III-VI_2 compounds and alloys, appropriate values for the deformation potentials are $b_p = -0.8 \pm 0.2$ eV and $b_d = -4.3 \pm 1.5$ eV. Also, it was found that the dimensionless ratio E/M determines the fractional d character in the valence band of these I-III-VI_2 compounds (84Y1). Thus, for a decrease in the value of E/M there is a corresponding increase in the d character of the valence band.

The analysis of the present experimental data using the YWS model was carried out in collaboration with

Kajornyod Yoodee, who dealt with most of the computation work and participated in all of the discussions.

In the analysis of the present experimental data using the YWS model of p-d hybridization valence band, the values of Δ^{p}_{so} , Δ^{d}_{so}, as given by eq. (VI-2) and (VI-3), and the variation of Δ^{p}_{cf} and Δ^{d}_{cf}, from eqs. (II-5) and (II-6) were the same as used in the Hopfield analysis case. The values of b_p and b_d used here, were taken from the original work of K. Yoodee et. al..

From equations (VI-5), (VI-6) and (VI-7), equations for $E_1 - E_o$ (= $E_B - E_A$) and $E_o - E_2$ (= $E_B - E_C$) as a function of the two unknown M and E may be obtained. Thus, with the above parameters, values for E/M as a function of composition and temperature can be calculated from eqs. (VI-5), (VI-6) and (VI-7).

When the above calculations were made, for a given sample at a given temperature, using the values of b_p =-0.8 eV and b_d=-4.3 eV and using the range of values for E and M obtained for the compounds in the original reference (84K1), it was found that in some instances solutions for $E_1 - E_o$ and $E_o - E_2$ could not be found. Thus to continue the analysis further, it was decided to introduce in the calculations a range of error for b_p of ± 0.2 eV and for b_d

of ± 1.5 eV, as well as a range of experimental error in the energy gap values which was estimated to be of about ±4 meV. The value of b_p was varied between 0.6 and 1.0 eV in steps of 0.05eV, and b_d was varied between 2.8 and 5.8 eV in steps of 0.75eV, while the energy gap values were varied in steps of 2meV. When this was done, the minimum and maximum values of the ratio E/M at each temperature were obtained, and in fig. (VI-16), the variation of E/M as a function of temperature for $CuGaSe_2$, y=0.65 and $CuGaS_2$ respectively are shown. The values of E/M as a function of composition at 20K are presented in fig. (VI-17).

It is seen in fig.(VI-16a) that the value of E/M for the sample $CuGaS_2$ is constant with temperature. However for the other end of this pseudobinary section, i.e. $CuGaSe_2$, it can be seen from fig.(VI-16c) that, within the scatter of the data, the values of E/M increase as the temperature increases and the variation may be taken as linear. Thus, it appears from these results that there is a small variation with composition of the slope given by these curves of E/M as a function of temperature.

Referring to the variation of E/M with composition, it can be seen in figure (VI-17) that the behavior of E/M Vs y is linear, and the same result was observed at all temperatures.

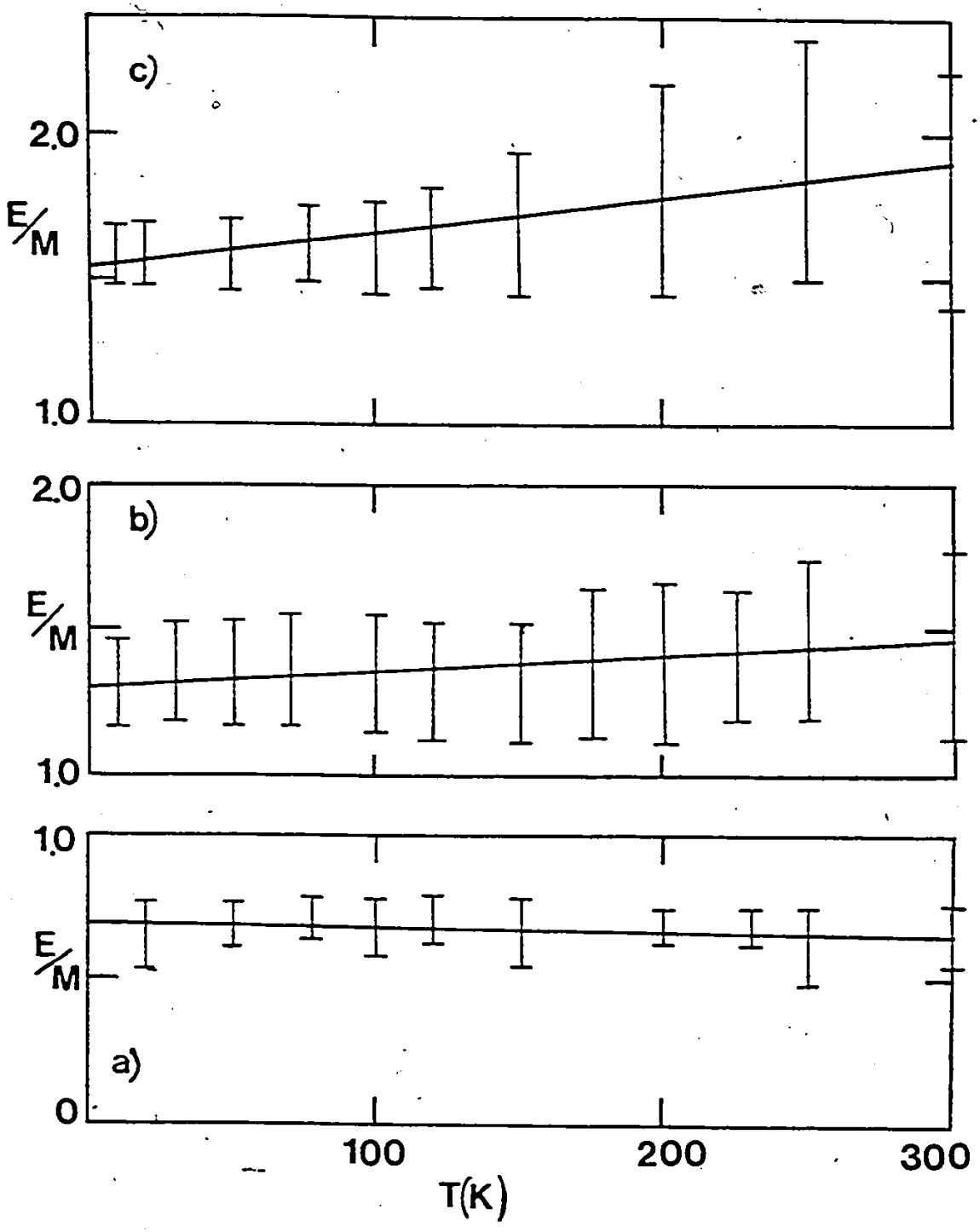

Fig. VI-16 $CuGa(S_{1-y}Se_y)_2$. Variation of the ratio E/M with temperature T for: a) y=0, b) y=0.65 and c) y=1.0.

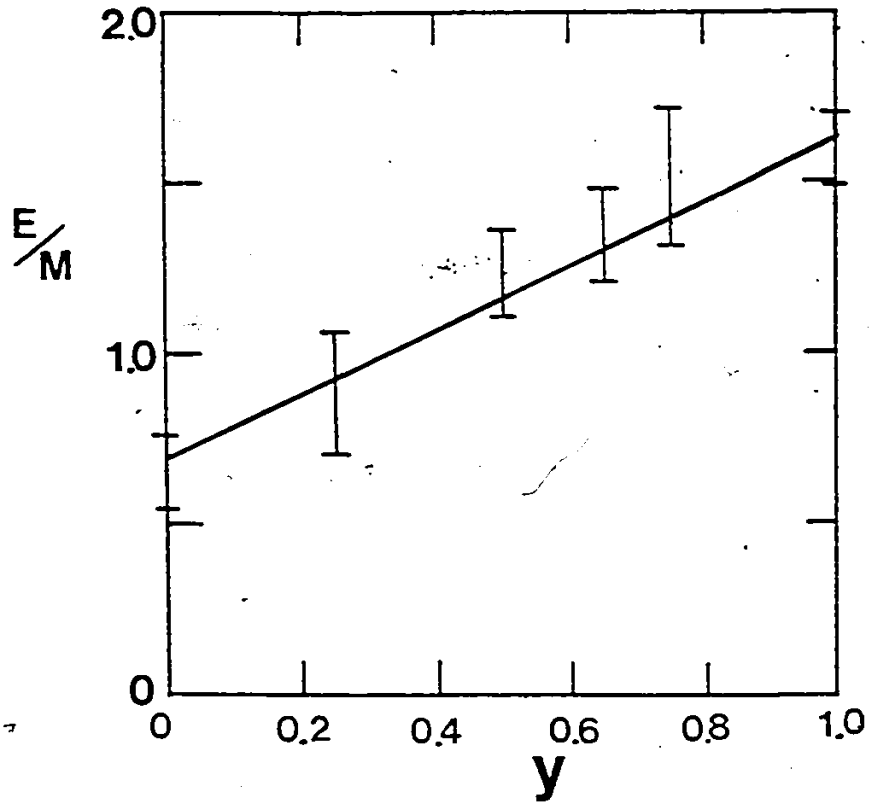

Fig. VI-17 $CuGa(S_{1-y}Se_y)_2$. Variation of the ratio E/M with composition y at 20K.

VI-4 DISCUSSION

With regard to the Hopfield analysis, it was indicated above that a poor fit to the experimental value of Δ_{cf} was obtained when the reported values of β for these samples were used in the analysis. When b_d and β were treated as adjustable parameters, it was found that for the coefficient β a negative value was obtained whereas the experimental value of β from X-ray work was positive. It seems therefore that some part of this analysis is invalid. Hopfield's equations (II-1) and (II-2) was developed for a p-like valence band and may not be applicable when the valence band has a high percentage of d character. Equations (II-3) to (II-6) assume that the total spin-orbit and crystal field splittings can be written as a linear sum of the p and d contributions and this is an assumption which may not be correct.

In the YWS model, the p-d interaction has been included in the calculations from the beginning. It was indicated above that, in this model, the ratio E/M determines the fractional d character in the valence band. With regard to the variation of E/M in the present work, it can be seen that the value of E/M at 20K for $CuGaS_2$ is smaller than that of $CuGaSe_2$ by an amount of about 1. It

has been suggested (85Y1) from the atomic energy level values for Cu d-states, S p-states and Se p-states, that the energy separation E between p and d levels for sulphur rich materials is smaller than that of selenium rich samples. Thus, in the case of sulphur rich materials the p-d interaction will be strong and hence the ratio E/M will be small in this case. Thus the fractional d character in the valence band will be greater for the sulfide rich than for the selenium rich materials. This explains the variation of the ratio E/M with composition for the present alloys shown in fig.(VI-17).

Referring to the variation of E/M with temperature, it was indicated that within the scatter of the present results, the slope of the E/M curves shows a small variation with composition, being 0 and 0.0011/K for $CuGaS_2$ and $CuGaSe_2$ respectively. The value of the slope for y=0 indicates that dE/dT and dM/dT have the same sign, and the value of the slope for y=1 indicates that these values of dE/dT and dM/dT are negative. A negative value for these parameters will correspond to a decrease in either M or E as the temperature is increased. The decrease in M, when the temperature is increased, is in agreement with earlier experimental studies (79Y1) which showed that in these I-III-VI_2 materials the anions gradually move away from the I cation and come relatively

nearer to the III cation as the temperature is increased. This indicates that the overlap between anions p states and copper d orbital will decrease as the temperature is increased, thus the matrix interaction M between p and d levels decreases as the temperature is increased.

VI-5 SUMMARY AND CONCLUSIONS

The preparation of these $CuGa(S_{1-y}Se_y)$ alloys by the iodine vapor transport method does not present problems. In all the cases, it was found that the surface of the samples was parallel to the (112) crystallographic plane.

The variations of the three transitions E_A, E_B and E_C with composition and temperature are typical of these alloys. The energy gap values of these transitions with temperature were very well fitted by a simple Manoogian-Leclerc equation.

The present experimental data were analyzed using two model viz., the Hopfield p-like valence band model (60H1) and the YWS model of p-d hybridization in the valence band (84Y1).

With the values of the crystal field and

spin-orbit interactions obtained using the Hopfield model, it was not possible to find a good fit to the values of Δ_{cf} for most of the samples investigated here. When β was taken as an adjustable parameter, a negative value was found for this coefficient, in contradiction to the value from X-ray work.

The variation of E/M with composition obtained from the YWS analysis was explained in terms of atomic energy differences between anions p states and Cu d levels. The value of E/M with temperature appeared to be constant for alloys with low values of y. However, for samples with high values of y there is a small variation of E/M with temperature. It was found from these results that the coefficients dE/dT and dM/dT have negative values. The variation of M with temperature is attributed to the decrease of the overlap between anions p orbitals and copper d levels as the temperature is increased.

CHAPTER VII

LATTICE PARAMETER AND OPTICAL-ENERGY GAP VALUES FOR THE $Cd_{2x}(CuIn)_y Mn_{2z} Te_2$ and $Cd_{2x}(AgIn)_y Mn_{2z} Te_2$ SYSTEMS

VII-1 INTRODUCTION

The name diluted magnetic semiconductor (DMS) or simply semi-magnetic semiconductor alloys (SMSA) has been applied to materials obtained by substituting, at random, a paramagnetic ion on the cation sub-lattice, e.g. for atoms that belong to group II, of the II-VI compounds. These semi-magnetic alloys have been the subject of attention because the presence of this paramagnetic ion causes considerable differences in the semiconducting behavior in a magnetic field from that of normal semiconductors and also introduces interesting magnetic behavior.

One of the most interesting aspects of these semimagnetic alloys is the presence of the partly-filled 3d levels, e.g. half-filled in the case of the manganese ions. It has been generally assumed that the $3d^5$ electrons are localized, and that their magnetic moments interact via exchange interaction (7962) (8201). These concepts of localization and exchange interaction have been applied in

order to explain most of the experimental data available for these materials, for example, assignment of some optical structures, other than those due to valence and conduction bands, observed in different types of optical experiments, formation of spin correlated clusters, spin-glass phase at low temperatures, as well as other magnetic effects (78G1) (82F1) (82O1). Studies of some magnetic properties on the materials under investigation will be described in the next chapter.

Most of the work on these (II-VI)-(Mn-VI) alloys has been carried out on pseudo-binary systems of the type $Cd_{1-z}Mn_zTe$, $Zn_{1-z}Mn_zTe$, etc.. Recently (83B1) the work done on such pseudobinary alloys has been extended to the pseudoternary alloy $Cd_xZn_yMn_zTe$ $(x+y+z=1)$.

Another possible extension of these SMSA would be to include the chalcopyrite compounds derived from the II-VI compounds. Some work has been done on the pseudobinary systems involving a II-VI compound and a $I-III-VI_2$ chalcopyrite compound. Robbins et. al.(75R1) has made crystallographic studies on pseudo-binary systems such as $Cd_{2(1-y)}(CuIn)_yS_2$, etc.. Woolley and Williams (66W1) determined the extent of solid solution, lattice parameter and optical energy gap values in the $Cd_{2(1-y)}(AgIn)_yTe_2$ and $Cd_{2(1-y)}(CuGa)_yTe_2$, but little information is available on the

$Cd_{2(1-y)}(CuIn)_y Te_2$ pseudobinary system. For this system Chernyavsky (62C1) reported complete solid solution, but no lattice parameter and energy gap values are available in the literature. However, with regard to SMSA involving chalcopyrite compounds and Mn as the paramagnetic ion, no work has as yet been reported on such materials. One possible type of pseudobinary chalcopyrite alloy involving manganese would be systems such as $(CuIn)_{1-z} Mn_{2z} Te_2$ and $(AgIn)_{1-z} Mn_{2z} Te_2$ discussed here. Thus systematic studies of the crystallographic, optical and magnetic properties of these alloys are of interest. Also these (Mn-VI)-(I-III-VI_2) pseudobinary systems can be extended to pseudoternary form by alloying with II-VI compounds to give such alloys as $Cd_{2x}(CuIn)_y Mn_{2z} Te_2$ and $Cd_{2x}(AgIn)_y Mn_{2z} Te_2$, etc.

The objective of the present chapter is to study the introduction of the paramagnetic ion Mn into some pseudo-binary systems of the type (II-VI)-(I-III-VI_2) to form pseudoternary alloys such as $Cd_{2x}(CuIn)_y Mn_{2z} Te_2$ and $Cd_{2x}(AgIn)_y Mn_{2z} Te_2$. Ranges of solid solution in both the cubic and chalcopyrite phase have been determined. Optical absorption measurements were made on samples in the single phase range at room temperature. The energy gap results show an interesting behavior as compared with those for the II-VI derived SMSA such as $Cd_x Zn_y Mn_z Te$(83B1). It is suggested that this difference in the results is due to ordering of the Mn on the cation sub-lattice with a body centered cubic (b.c.c.) arrangement (84W1).

VII-2 THE $Cd_{2x}(CuIn)_y Mn_{2z} Te_2$ SYSTEM

The alloy system $Cd_{2x}(CuIn)_y Mn_{2z} Te_2$ $(x+y+z=1)$ can be conveniently represented by a triangle as shown in fig.(VII-1) with the ternary compound at one vertex and the CdTe and MnTe at the other corners of the triangle. The pseudobinary section $Cd_{1-z}Mn_z Te$ already reported (83B1) forms one edge, and the pseudobinary systems $Cd_{2(1-y)}(CuIn)_y Te_2$ and $(CuIn)_{1-z} Mn_{2z} Te_2$, for which no informations are available, form the other two edges of this triangle. The range of sample composition investigated in this work is also shown in fig.(VII-1), the compositions being chosen so that parameter values along lines of constant z and of constant x:y ratio could be compared.

VII-2a SAMPLE PREPARATION AND EXPERIMENTAL MEASUREMENTS

Polycrystalline samples of the alloys were produced by the same technique as described in chapter III. But, in the case of the semimagnetic alloys investigated in this chapter, it was found necessary to carbonize the quartz tubes in order to prevent the manganese attacking the quartz at high temperatures. After melting, the samples were annealed at 600°C. It was found

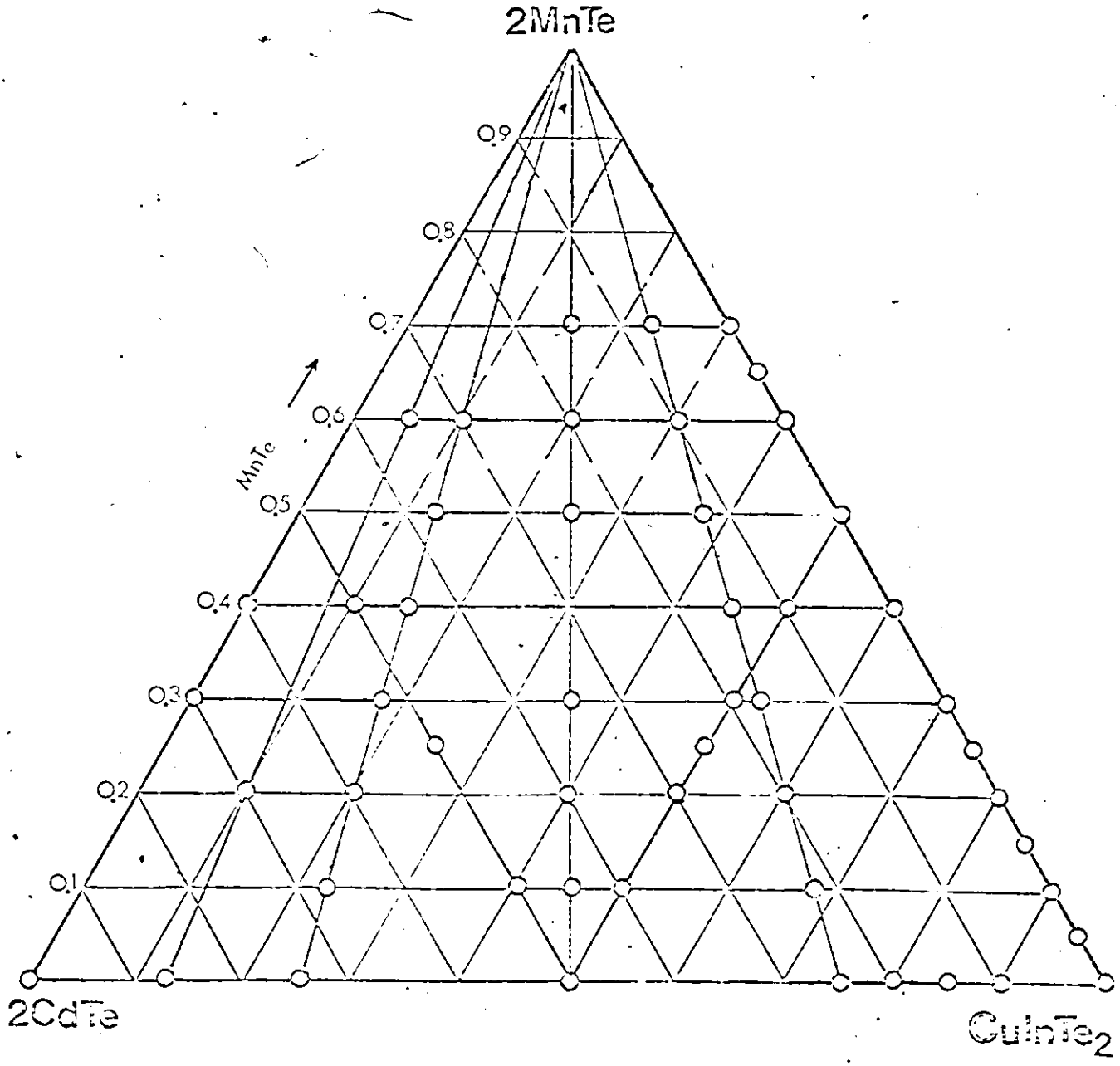

Fig. VII-1 $Cd_{1-x}(CuIn)_{x}Mn_{1-x}Te_{2}$. Composition diagram. The solid circles show the samples used in this investigation.

that an annealing period of between twenty to thirty days gave good equilibrium conditions. The Debye-Scherrer powder x-ray technique was used to check the equilibrium condition of each sample and to determine whether a single phase solid solution was obtained. In the case of high values of the composition parameter y, i.e. compositions close to $CuInTe_2$, a chalcopyrite structure with c/a=2 was found. For the rest of the composition diagram, the alloys were found to have a cubic structure with some ordering lines being observed. This work will be discussed later. Again the Nelson-Riley (45N1) extrapolation method was used to obtain accurate lattice parameter values.

Alloys showing single phase of either chalcopyrite or cubic structure were sliced and polished down to thickness in the range 30 to 150μm to provide samples for optical absorption measurements. The method of preparation of the samples for this optical work was the same as described in chapter IV. After the transmision measurement was carried out, the absorption coefficient was calculated and corrected as described in chapter IV.

VII-2b X-RAY RESULTS AND ANALYSIS

Figures (VII-2) and (VII-3) show the variation of the lattice parameter values for this system, fig.(VII-2) giving the variation of a with y for constant z and fig.(VII-3) the variation of a with z for several different x:y ratios. It can be seen from these figures that except in the composition range of high y, the parameter a varies linearly with the composition variable. In the latter composition range, the variation of a with y and z deviates from the linear behavior shown for the rest of the alloys. In this region of high values of y, chalcopyrite structure with c/a=2 was obtained. From the form of the non-linear behavior shown in figs.(VII-2) and (VII-3) and from the analysis of the ordering lines present in these films, the range of chalcopyrite phase was determined and the estimated region of chalcopyrite phase boundary is shown in fig.(VII-4).

Turning to the alloys inside the composition triangle, i.e. outside the chalcopyrite field, these were found to have a cubic structure, the main X-ray lines of which analyzed as zincblende. However as was indicated in section VII-2a, these alloys showed some degree of ordering. From the intensity of the ordering lines observed in these samples, it was found that the degree of

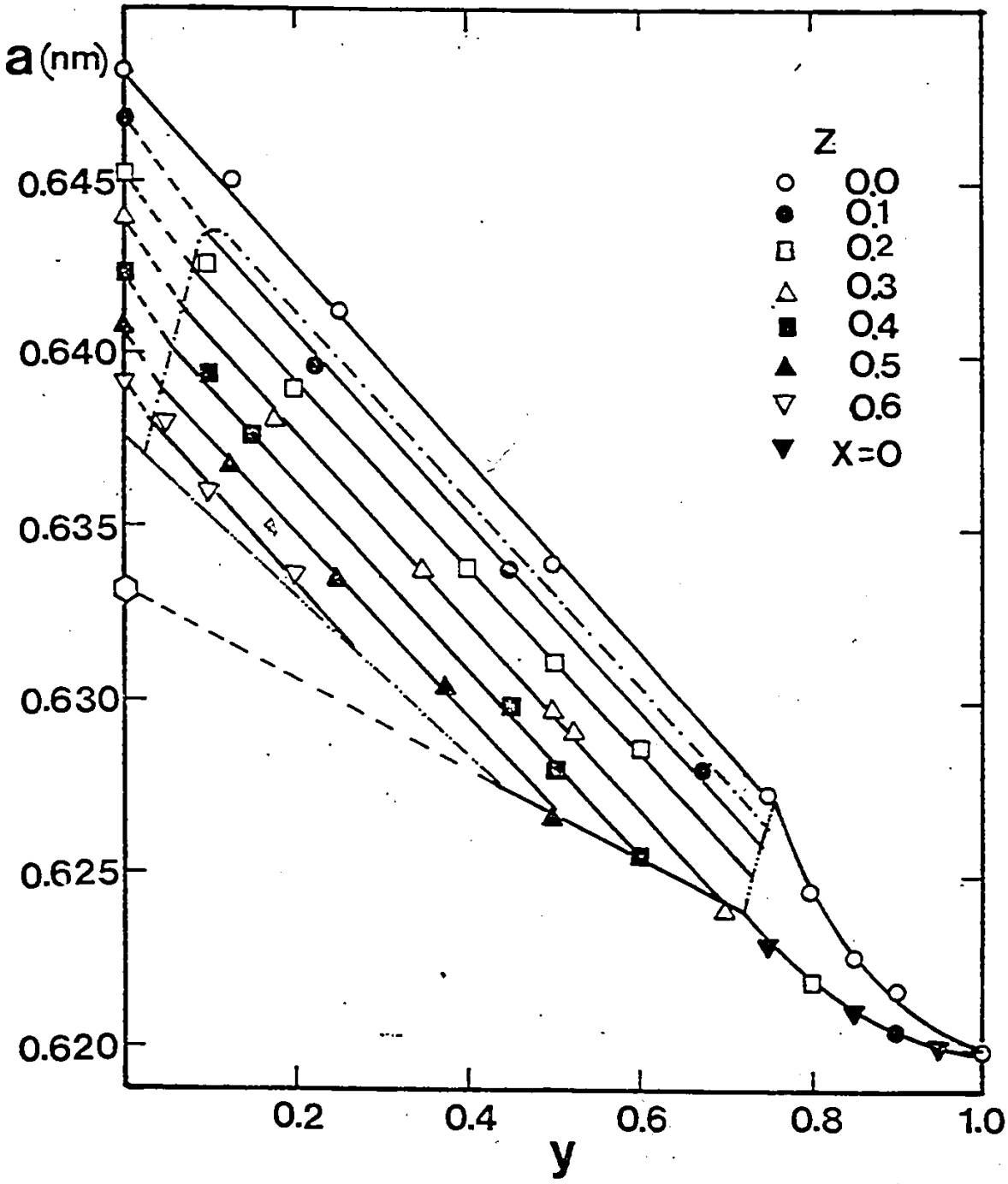

Fig. VII-2 $Cd_{2x}(CuIn)_y Mn_{2z} Te_2$. Variation of lattice parameter a with composition y for various constant values of z. The dash-double-dotted lines indicate the phase boundaries. The dashed lines are extrapolation curves. The dash-dotted line indicates the estimate limit of the ordered field.

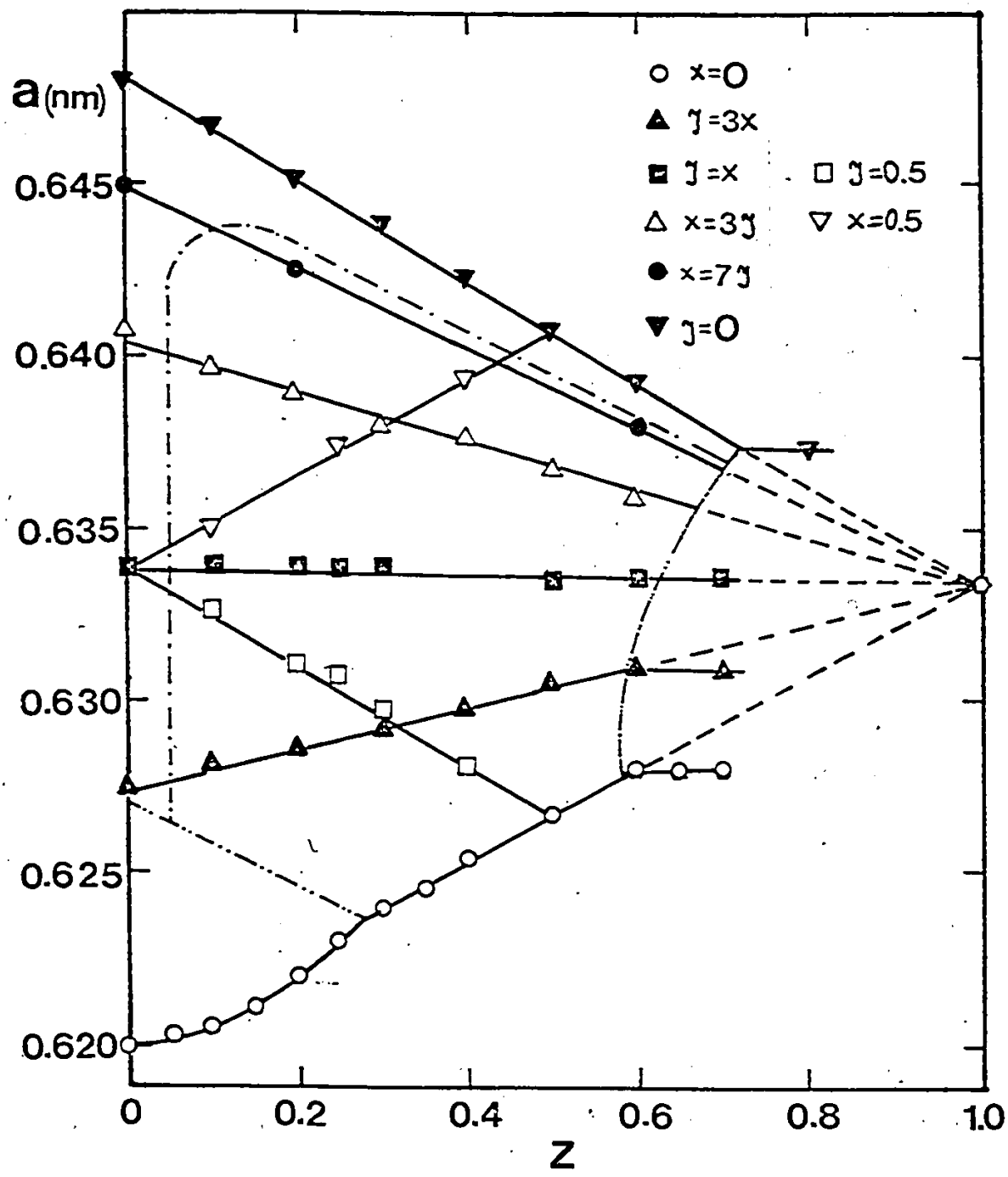

Fig. VII-3 $Cd_{2x}(CuIn)_y Mn_{2z} Te_2$. Variation of lattice parameter a with z for several different x:y ratios. The dash-double-dotted lines are phase boundaries. The dashed lines are extrapolation lines. The dash-dotted line indicates the limit of the ordered field.

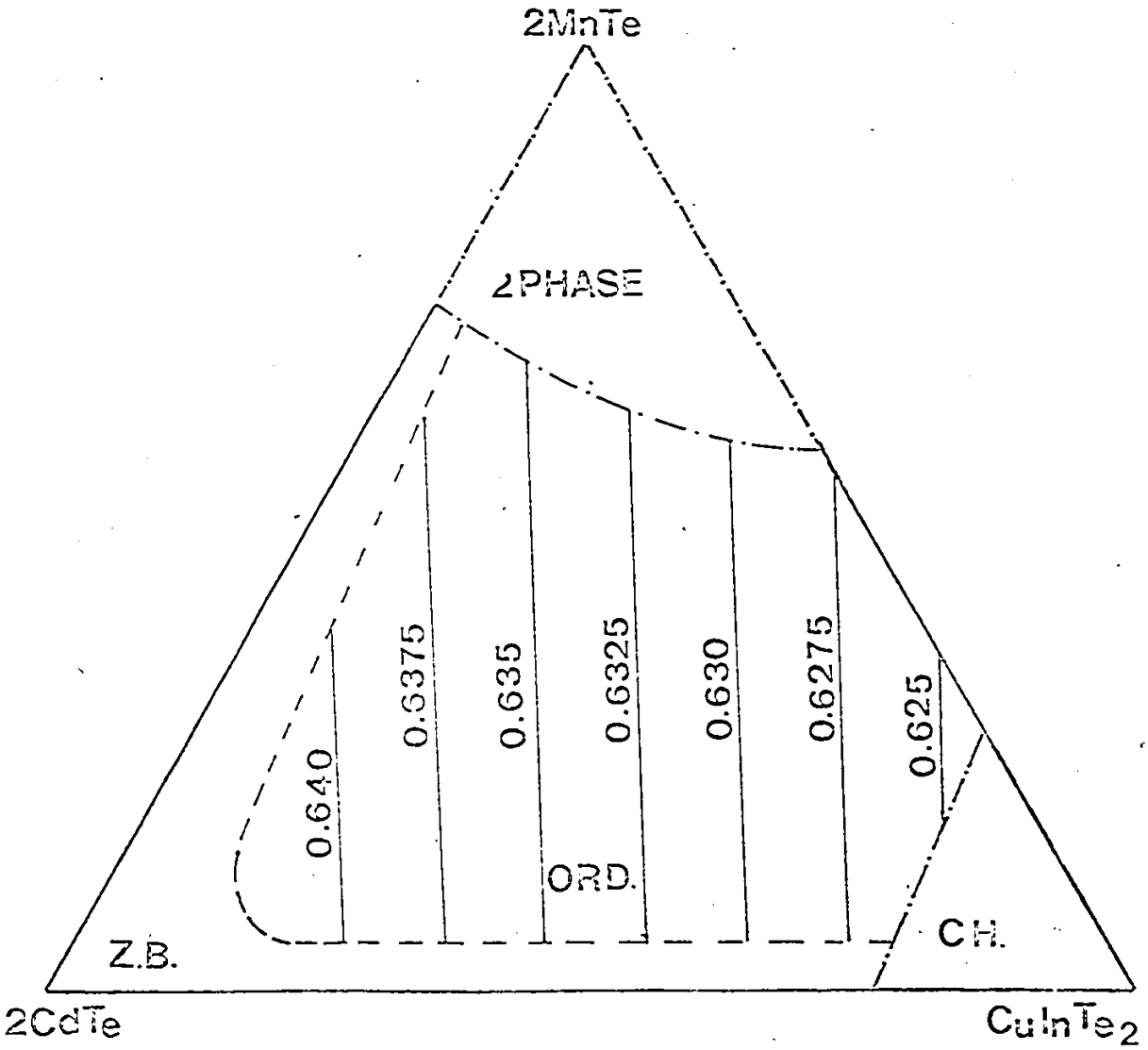

Fig. VII-4 Cd_{2x} $(CuIn)_x$ Mn_{2x} Te_2 - Isothermal section for samples annealed at 600°C and quenched to room temperature. The dash-dotted lines indicate the phase boundaries. The dash dot line indicate the limit of the ordered phase field. The solid lines indicate the contours of constant a, values indicated in nm.

ordering varied appreciably with composition. Thus no ordering lines were observed in the $Cd_{2(1-y)}(CuIn)_y Te_2$ and $Cd_{1-z} Mn_z$ Te pseudo-binary edges. Also, it was observed that the degree of ordering reaches a maximum at z-0.2 and then decreases as the concentration of manganese ions is further increased. In the initial work on these alloys (84W1) the ordering behavior was investigated in the line y=0.5 of the present system and also of the systems $Cd_{2x}(AgIn)_y Mn_{2z} Te_2$ and $Cd_{2x}(AgGa)_y Mn_{2z} Te_2$. Analysis of the data for those lines indicates the ordering is due to the manganese and that the manganese atoms order on the cation sublattice to give a body centered cubic structure with lattice parameter 2a where a is the parameter of the original zincblende structure (84W1). Because of the variation in the degree of ordering with composition it was not possible to determine the limits of the ordered range from the present X-ray data. However, as will be shown in the next section, energy gap values for this alloy system are found to give a good indication of the limits of the ordered range.

In fig.(VII-2), outside the chalcopyrite phase field, the lines of a Vs y at constant z are parallel to each other, while in fig.(VII-3) the lines for six different x:y ratios (values of a for the line y=0 taken form ref.(83B1)) all extrapolated at z=1 to a single value

a=0.633nm which represents the lattice parameter that MnTe would have in this cubic phase. The limits of single-phase solid solution can be seen for several lines in fig.(VII-3) and the approximated form of the single-phase boundary is illustrated in fig.(VII-4). Further analysis of the present X-ray results for the ordered alloys will be given below.

VII-2c ENERGY GAP RESULTS AND ANALYSIS

Optical absorption measurements were carried out at room temperature on most of the single-phase samples, and absorption edges were determined as indicated above. Initially, curves of $(\alpha h\nu)^2$ were plotted as a function of the photon energy for most of the samples investigated. In the case of CdTe the $(\alpha h\nu)^2$ Vs $h\nu$ curve was found to be linear indicating that the optical transition involved in this sample is direct allowed. But, for the rest of the alloys, it was observed that these graphs of $(\alpha h\nu)^2$ Vs $h\nu$ did not give the good linear variation expected for a material in which the energy gap involved is direct allowed..

Hence curves of $(\alpha h\nu)^n$ Vs $h\nu$ for n=2, 1.6, 1.3, 1, 2/3 and 1/2 were plotted for some of the alloys, and in figs.(VII-5) to (VII-7) the results for n=2, 2/3 and

1/2 for several samples of this system are shown, compositions being labeled on the graphs. With reference to these figures, it was found that as the parameter n decreases the experimental data tend to be better described by a linear variation, and the values n=2/3 and 1/2 giving the best linear fit to the absorption data. As was indicated in chapter IV, n=1/2 corresponds to an indirect allowed transition at the band edge, while n=2/3 is for a direct forbidden transition. This analysis of the present experimental data would seem to indicate that one or the other applies in the present materials.

Consider first the possibility that the n=1/2 results indicate ah indirect gap for these materials. In previous work on photovoltage measurements on rectifying Au-$CuInTe_2$ contacts (73P1), it was suggested that since the results correspond to the $(\alpha h\nu)^{1/2}$ Vs $h\nu$ form the fundamental band gap is apparently indirect. However, investigations on $AgGaS_2$, $CuGaSe_2$ and other I-III-VI_2 ternary compounds (74S1) lead to the conclusion that these materials have a direct band gap at the Γ-point of the chalcopyrite Brillouin zone. This can be illustrated simply from embedding the chalcopyrite Brillouin zone into the zone of the analogous zincblende as is illustrated in figs.(II-4) and (II-5). In the case of the ordered alloys, the body center cubic Brillouin zone was embedded into a

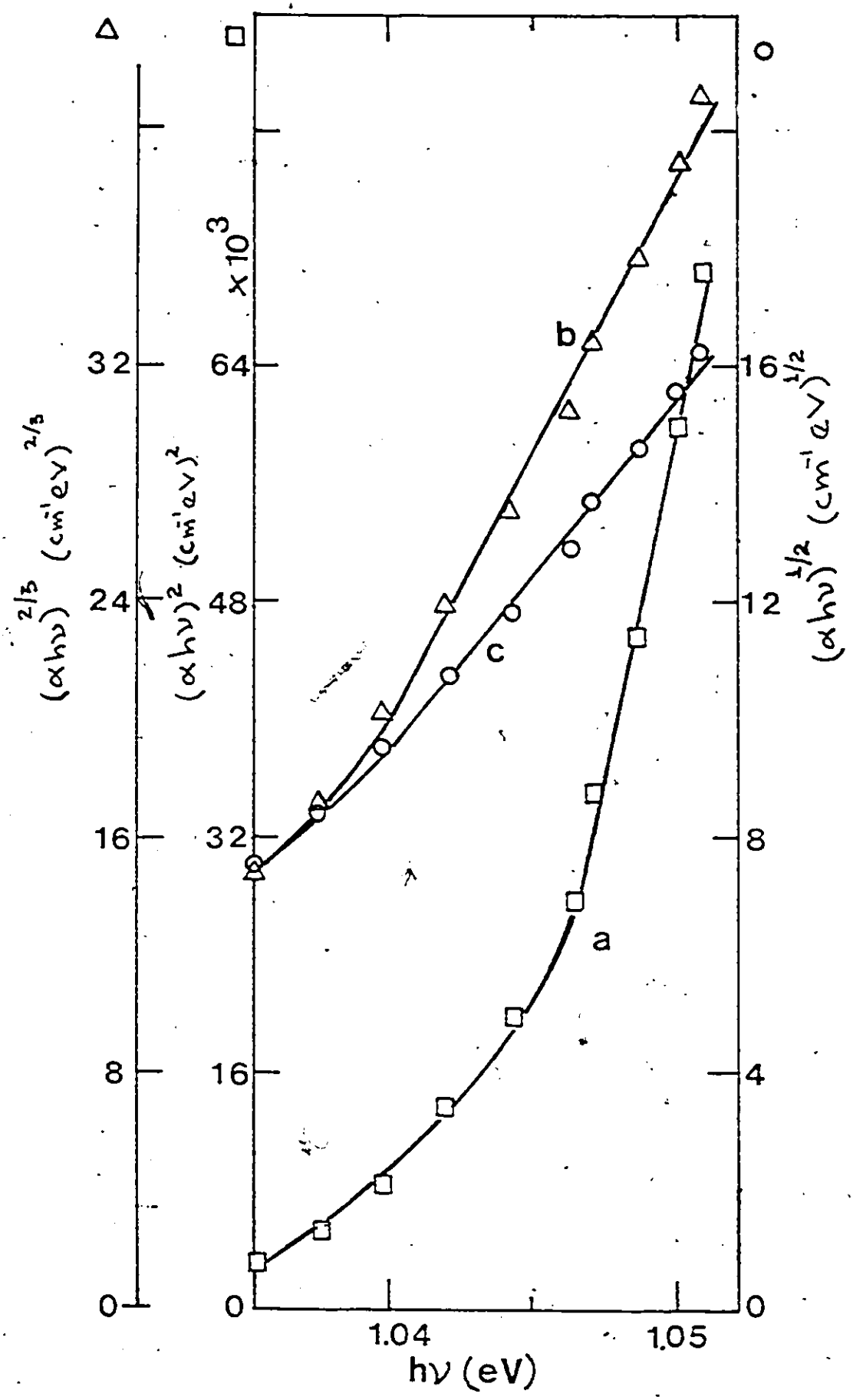

Fig. VII-5 $Cd_{2x}(CuIn)_yMn_{2z}Te_2$. $(\alpha h\nu)^n$ curves for the sample y=0.75 z=0.25. a) n=2. b) n=2/3. c) n=1/2.

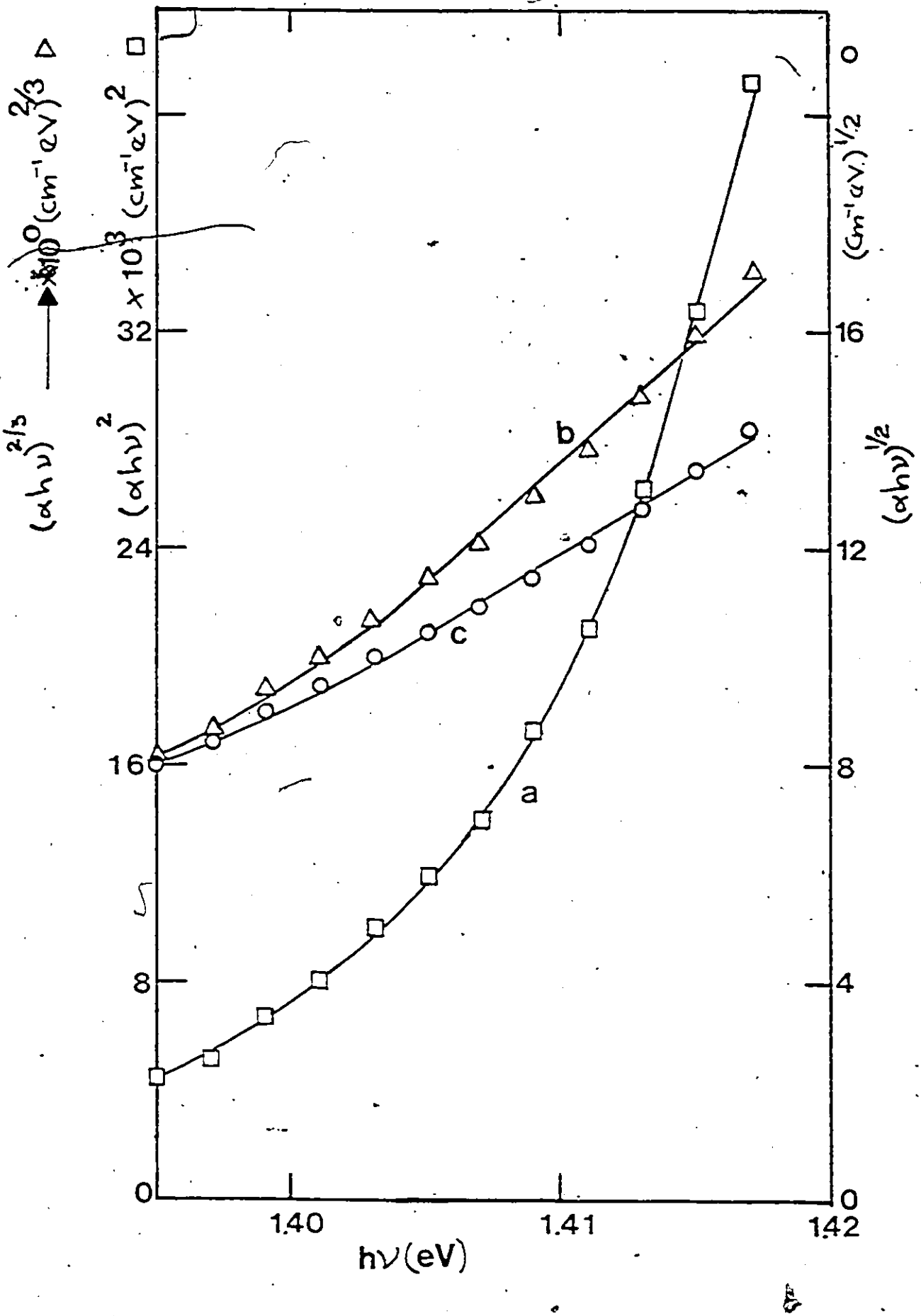

Fig. VII-6 $Cd_{2x}(CuIn)_yMn_{2z}Te$. $(\alpha h\nu)^n$ curves for the sample y=0.375 z=0.5. a) n=2. b) n=2/3. c) n=1/2.

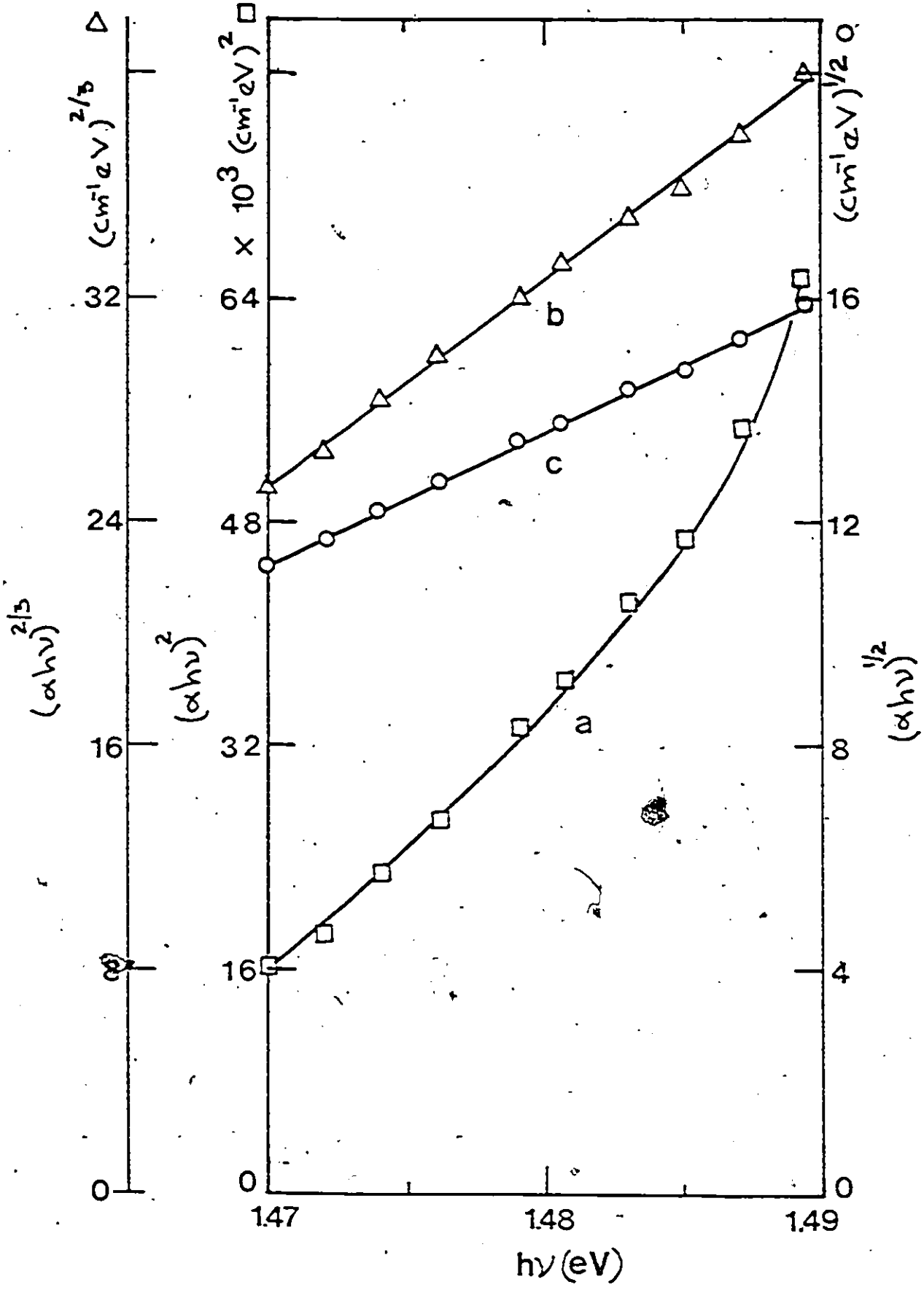

Fig. VII-7 $Cd_{2x}(CuIn)_yMn_{2z}Te_2$. $(\alpha h\nu)^n$ curves for the sample y=0.25/0.5. a) n=2. b) n=2/3. c) n=1/2.

reciprocal zone of a zincblende sample indicating that for these alloys also the transition involved is probably direct at the Γ-point.

Turning to the case n=2/3, this would indicate that the transition is direct but forbidden. Such a result appears feasible when the d character of the valence band is considered. As was shown in chapter VI for the $I-III-VI_2$ compounds and alloys, the noble metal d levels are close in energy to the valence band so that hybridization occurs and the valence band can have up to 35% d character. In the case of the alloys containing manganese a similar effect may occur (8202). The 3d states of Mn acquire some degree of p character and become delocalized, while the valence bands acquire some degree of d character. Although no estimates have, as yet, been made of the percentage d character in the valence bands, it is likely to be similar to the values for the chalcopyrite compounds.

Since d--->s represents a forbidden atomic transition, the d character of the valence band would cause the band gap transition to be forbidden to some extent. However, a study of the analysis of the value of the absorption coefficient α in the general case shows that if both p and d character are present in the valence band the total α will be the sum of the p and d

contributions. Since close to the Γ-point the value of α for p character is much greater than that of the d, it appears that even with a large fraction of d character being present, the variation of α should nevertheless show square law behavior. On this basis, it appears unlikely that the results represent a forbidden transition. One point to be remembered is that in the alloys band tailing can occur and this could result in the observed form of the $(\alpha h\nu)^n$ graphs. Thus it is not possible with the present results to come to any definite conclusion about the form of the absorption edge, for that analysis very thin samples would be required.

Hence in the present work graphs with n=2 have been used to give the energy gap values for all of the alloys investigated. In any given case, the value of E_o determined from the lines with n=2/3 were consistently 20 to 30 meV lower than for the n=2 line so that the form and variation of the present results will be practically not affected by the criterion used to obtain the energy gap data.

The resulting variation of E_o with x, determined as indicated above, for various constant values of z, and E_o Vs z for the several x:y ratios (values of E_o for the pseudobinary edge y=0 were taken from ref. (83B1), except

the samples x=1, 0.3, 0.4 which were analyzed by optical absorption in the present work) are shown in fig.(VII-8) and (VII-9). It is seen from these figures that the variation of E_o with a composition variable for the pseudobinary edge $Cd_{1-z}Mn_z$ Te (line y=0) is linear and extrapolate at z=1 to a value of 2.8 eV which represents the value of E_o that MnTe would have in the zincblende form, in agreement with previous results on the pseudoternary system $Cd_x Zn_y Mn_z$ Te(83B1). However the specimens inside the composition triangle and outside the chalcopyrite field, i.e. samples that are ordered, show a different form with all the lines for different x:y ratios aiming at a single value of 1.9 eV at z=1 which represents the energy gap value that MnTe would have in the ordered phase field. The chalcopyrite samples of the pseudobinary edge x=0 extrapolate to z=1 in a third point 1.36 eV which represents in this case the value of E_o that MnTe would have in the chalcopyrite phase. The limits of the ordered range can now be easily determined by considering the intersection between the lines with aiming point 2.8 eV with those lines with aiming point 1.9 eV. This is illustrated in figs.(VII-8) and (VII-9), and the approximate form of the ordered phase boundary so obtained is shown in figs.(VII-4) and (VII-8).

With regard to the lattice parameter values in the

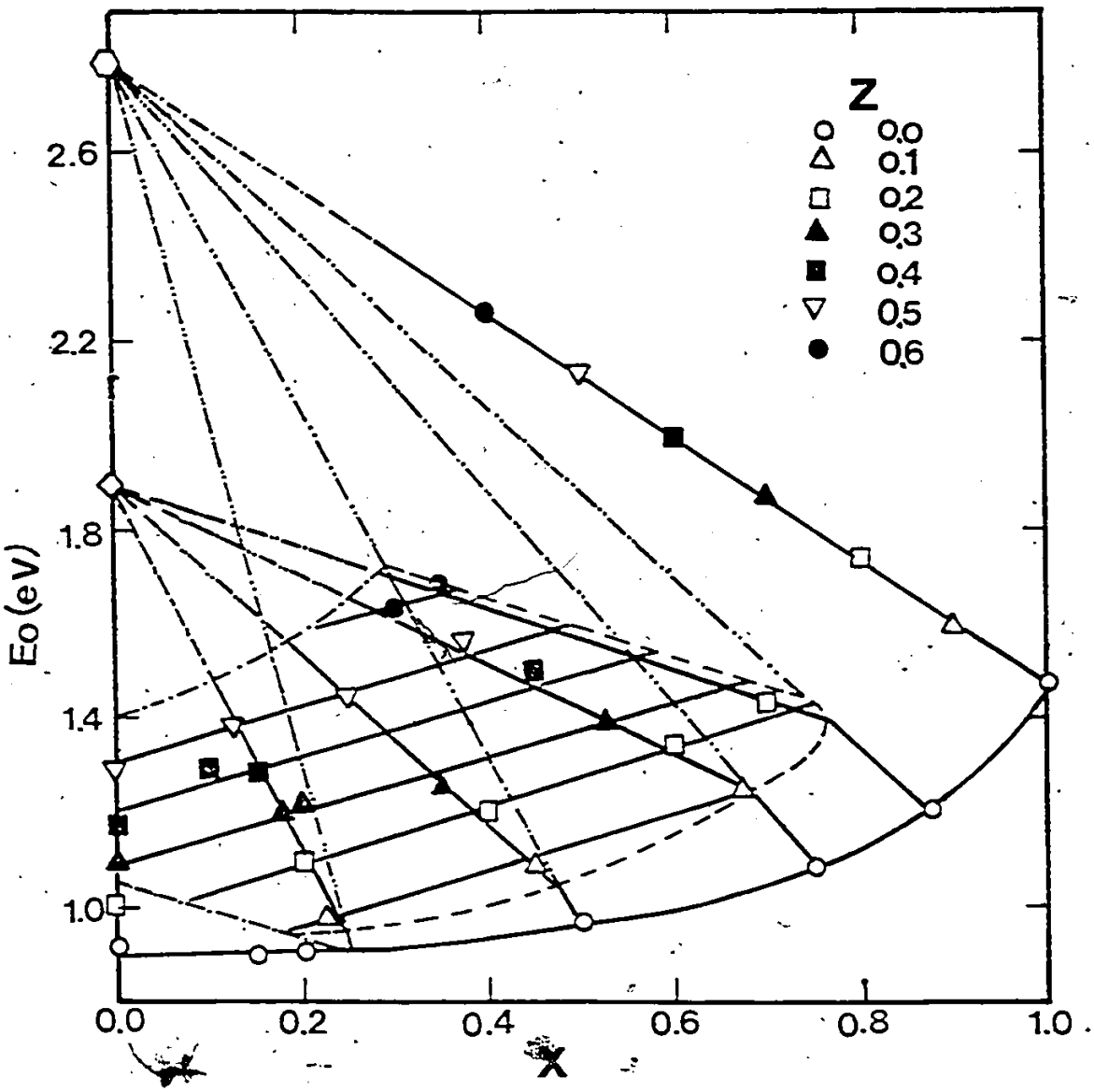

Fig. VII-8 $Cd_{2x}(CuIn)_y Mn_{2z} Te_2$. Variation of energy gap E_o at 300K with x for various constant values of z, for samples showing single phase behavior. The dash-dotted lines indicate the phase boundaries. The dash-double-dotted lines are extrapolation lines. The dash line indicate the limit of the ordered range.

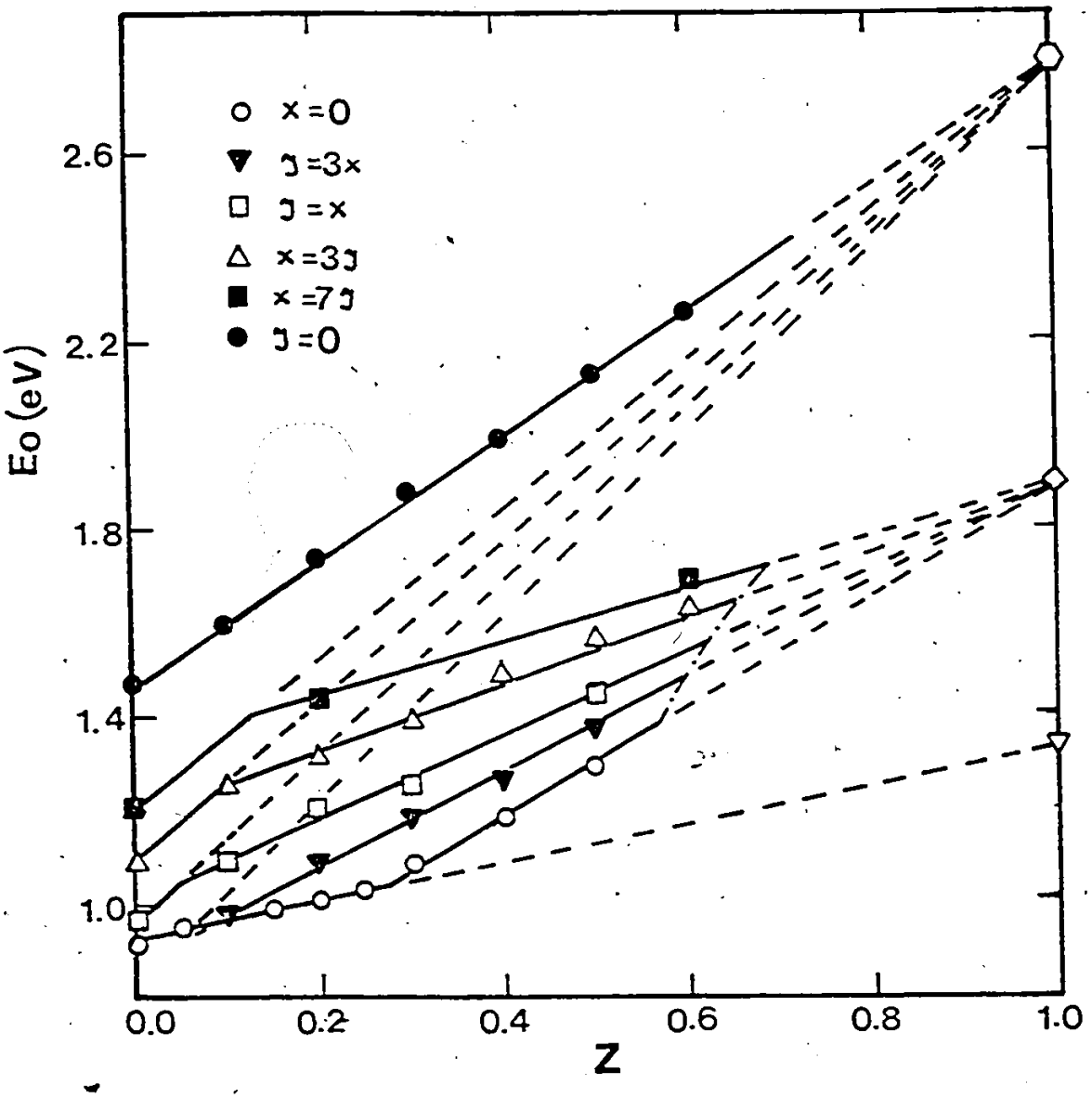

Fig. VII-9 $Cd_{2x}(CuIn)_yMn_{2z}Te_2$. Variation of energy gap E_o at 300K with z for various x:y ratios. Dash-dotted lines indicate the phase boundary. The dashed lines are extrapolation lines.

ordering phase field, an empirical equation describing the variation of a with composition may be developed. Since as is seen from figs.(VII-2) and (VII-3), all the lines of a Vs. a composition variable are straight and the lines for different constant values of z are parallel, a general expression for a in the ordered phase field can be written as

$$a=A+Bx+Cy. \qquad \text{(VII-1)}$$

Values of a' for 29 compositions in the ordered range were fitted to the above equation. The resulting relation was found to be:

$$a=0.6333+0.01416x-0.01281y \qquad \text{(VII-2)}$$

and the standard deviation of the fitted points was σ =0.0002nm. From equation (VII-2) lines of constant a can be determined and these are shown in fig.(VII-4)

VII-3 THE $Cd_{2x}(AgIn)_y Mn_{2z} Te$ ALLOY SYSTEM

The range of composition used to investigate this alloy system is shown in fig.(VII-10), again the compositions were chosen in the same way as before by reason of comparison with the pseudo-ternary systems already investigated, viz. $Cd_{2x}(CuIn)_y Mn_{2z} Te_2$, $Cd_x Zn_y Mn_z Te$ (83B1).

V-3a SAMPLE PREPARATION AND EXPERIMENTAL MEASUREMENTS

The method used to produce polycrystalline samples of this alloy system was the same as that described in chapter III. The samples were annealed at 600°C with periods of twenty to thirty days of annealing giving good equilibrium conditions. Again the Debye-Scherrer powder X-ray technique was used to determine the equilibrium condition of the alloys and to check whether a single-phase solid solution was obtained. In the region of high values of the composition parameter y, the alloys were found to have a chalcopyrite structure with $c/a<2$. For this region of $c/a<2$, the method of internal calibration with silicon, chapter IV, was used to determine accurate lattice parameter values. For the rest of the semimagnetic alloys, a cubic structure was found

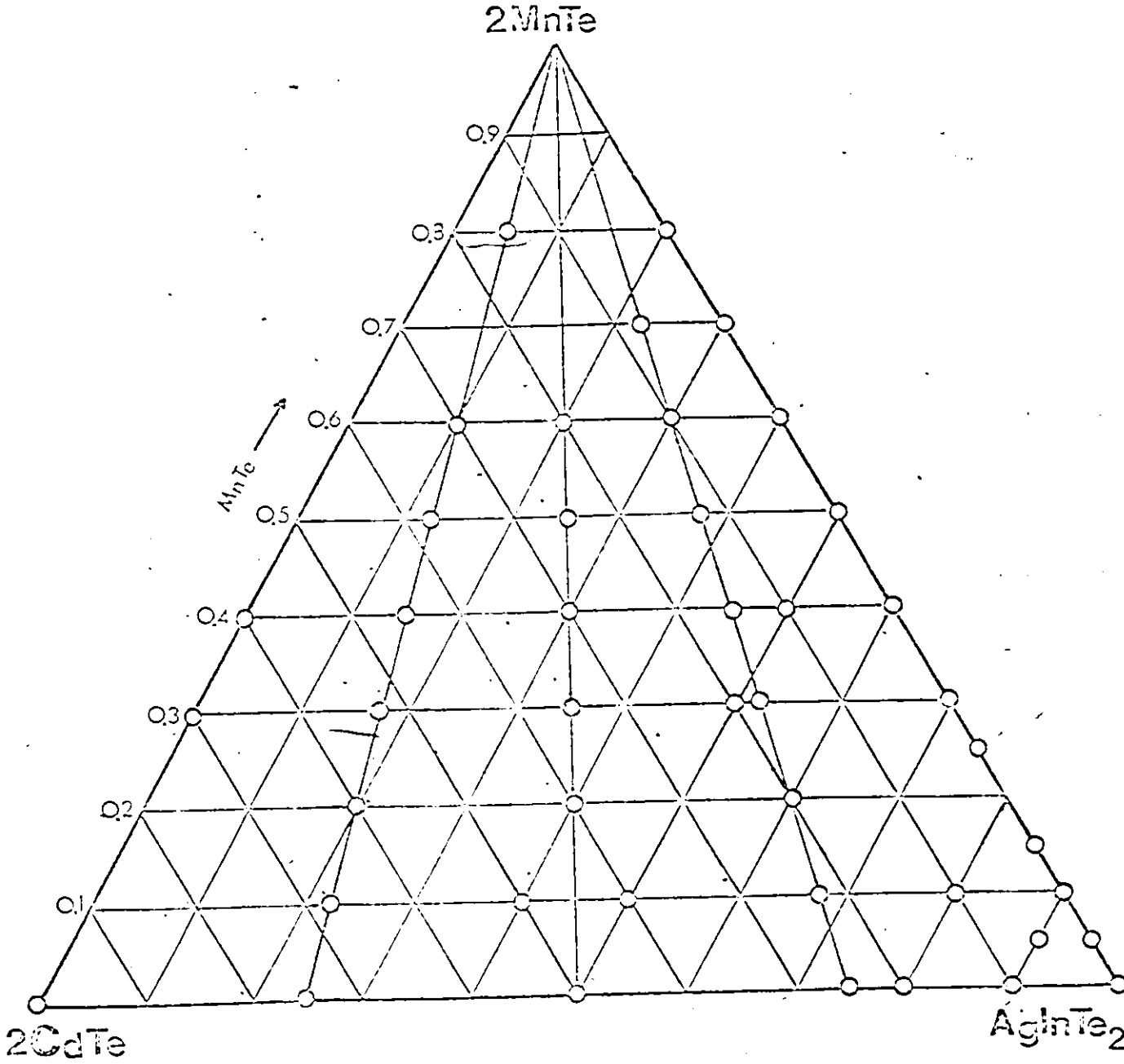

Fig. VII-10 Cd_{2x} $(AgIn)_y$ Mn_{2z} Te_2. Composition diagram. The solid circles show the samples used in this investigation.

and again the presence of some degree of ordering was observed in the X-ray powder films. The Nelson-Riley extrapolation method was used to obtain accurate lattice parameter values for these cubic samples.

The optical absorption work involved in these alloys was the same as in section VII-2a. Again, each specimen was polished down to a thickness between 30 and 150 μm. The absorption coefficient was determined and corrected for background effects as described in chapter IV.

VII-3b X-RAY RESULTS AND ANALYSIS

In the case of the present semimagnetic system $Cd_{2x}(AgIn)_y Mn_{2z} Te_2$, samples with high values of the composition parameter y, $AgInTe_2$, were found to have a chalcopyrite structure with c/a<2. Hence values of a and c were calculated for each specimen. The method of internal calibration, with silicon as standard, was used to obtain accurate lattice parameter values for these samples with c/a<2. For the rest of the composition diagram a cubic structure was obtained. Figure (VII-11) shows for all single phase samples the variation of a as a function of y for various lines of constant z. Figure (VII-12) shows the variation of a with z for five different x:y ratios.

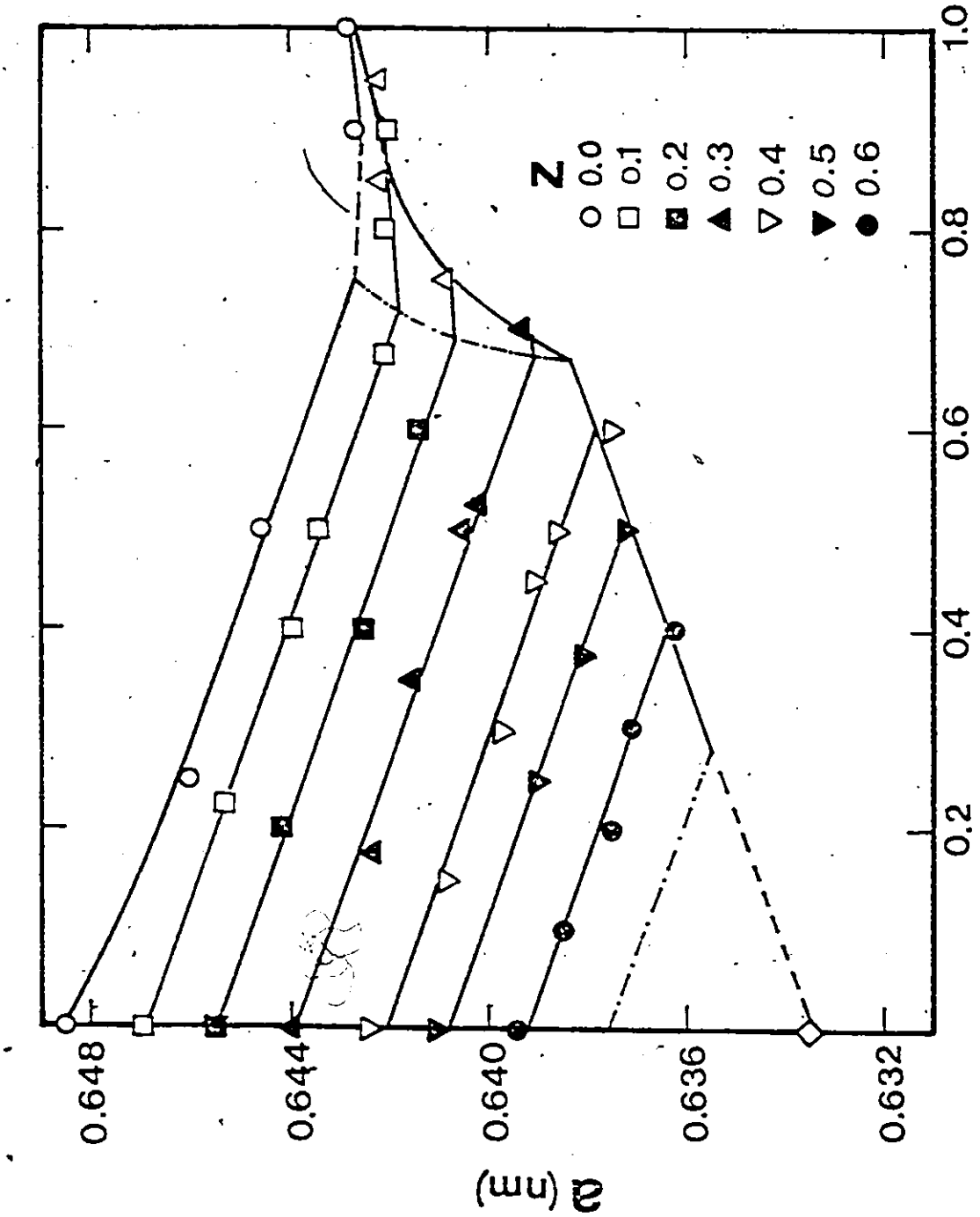

Fig. VII-11 $(AgIn)_y Mn_{2z} Te_2$. Variation of lattice parameter a with y for various constant values of z. Dash-dotted lines are phase boundaries. Dashed line is an extrapolation line.

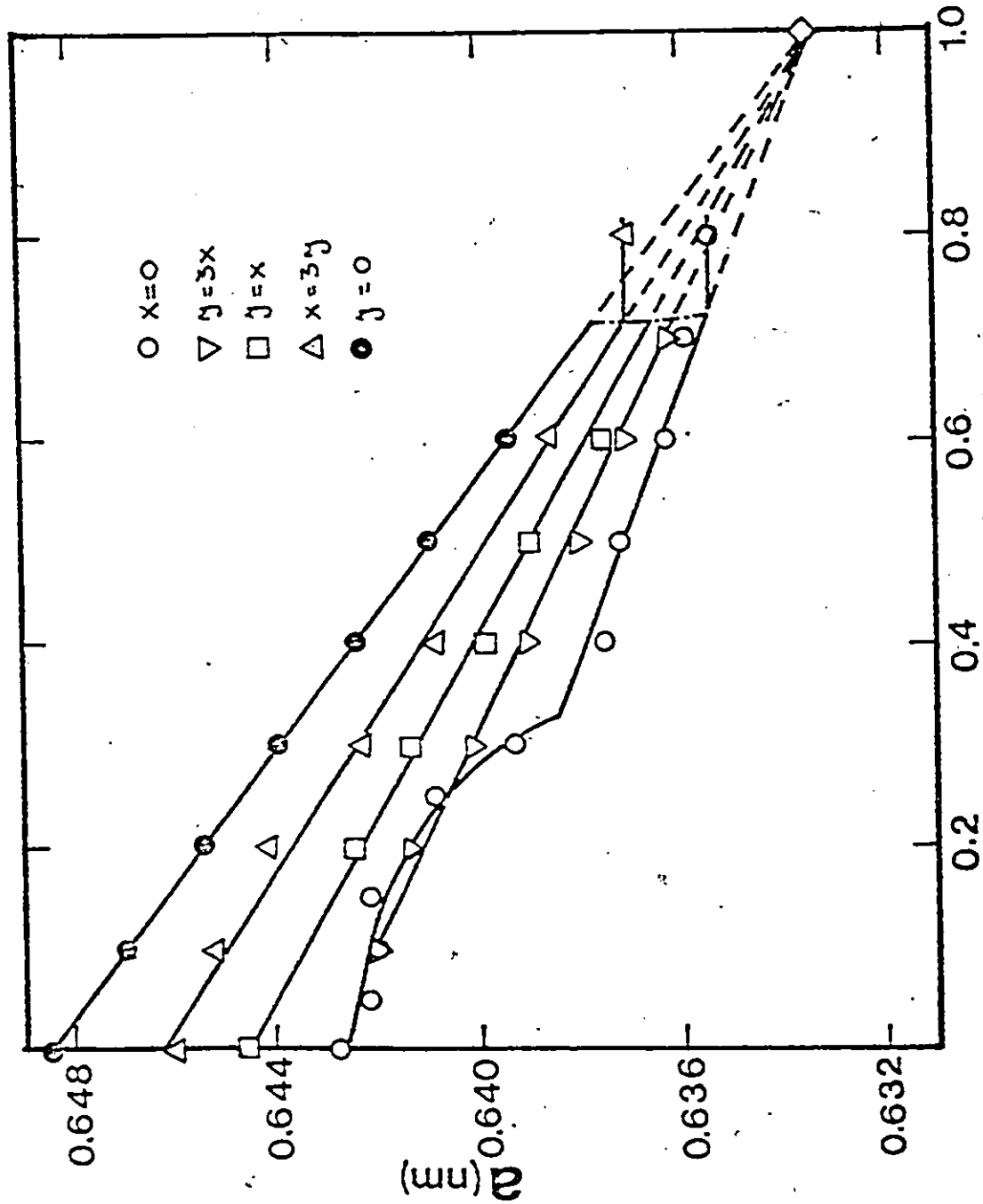

Fig. VII-12 $Cd_{2x}(AgIn)_y Mn_{2z} Te_2$. Variation of lattice parameter a with z for several different x:y ratios. Dash-dotted line is the limit of single phase solution. Dashed lines are extrapolation lines.

As in the case of the $Cd_{2x}(CuIn)_yMn_{2z}Te_2$ system, it is seen that the variation of a with a composition variable is linear up to the limits of the chalcopyrite phase where the variation appears to be non-linear. The limits of chalcopyrite single phase can be determined by considering the c/a values obtained for the chalcopyrite samples. This is illustrated in figs. (VII-13a), (VII-13b) and (VII-13c); (VII-13a) and (VII-13b) show the variation of c/a with z for the two lines x=0 and x=z respectively, and (VII-13c) the variation of c/a with x for the line z=0.1. Drawing a curve through these points, the limits of chalcopyrite phase are taken at the intersection of these lines with the horizontal line through an effective c/a=2 line representing the samples of the cubic phase. These values are then used to draw the limits of chalcopyrite single phase shown in fig. (VII-14).

With regard to the pseudo-binary edge z=0, viz. $Cd_{2(1-y)}(AgIn)_y Te_2$, from y=0 to 0.74, the alloys were single phase with zincblende structure. However the y=0.75 and 0.8 alloys were two phase, one zincblende and one chalcopyrite, while the y=0.9 sample was chalcopyrite single phase. In spite of the longer annealing time given to these two-phase samples (60 days), they showed blurred X-ray lines, and were difficult to analyze. This two phase field on the line z=0 is indicated approximately in the

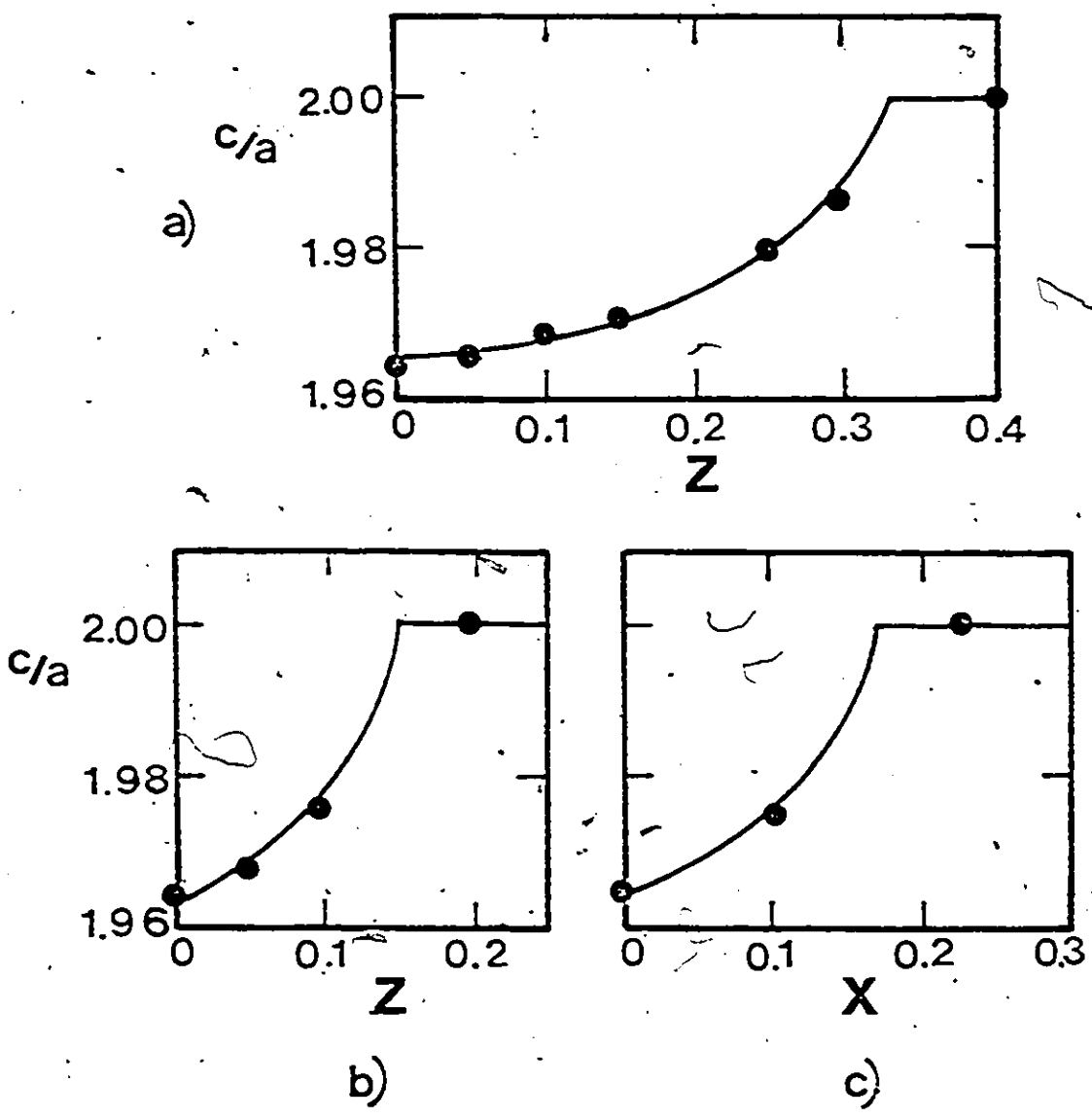

Fig. VII-13 $Cd_{2x}(AgIn)_yMn_{2z}Te_2$. Variation of the ratio c/a with composition for several sections: a) x=0, b) x=z and c) z=0.1.

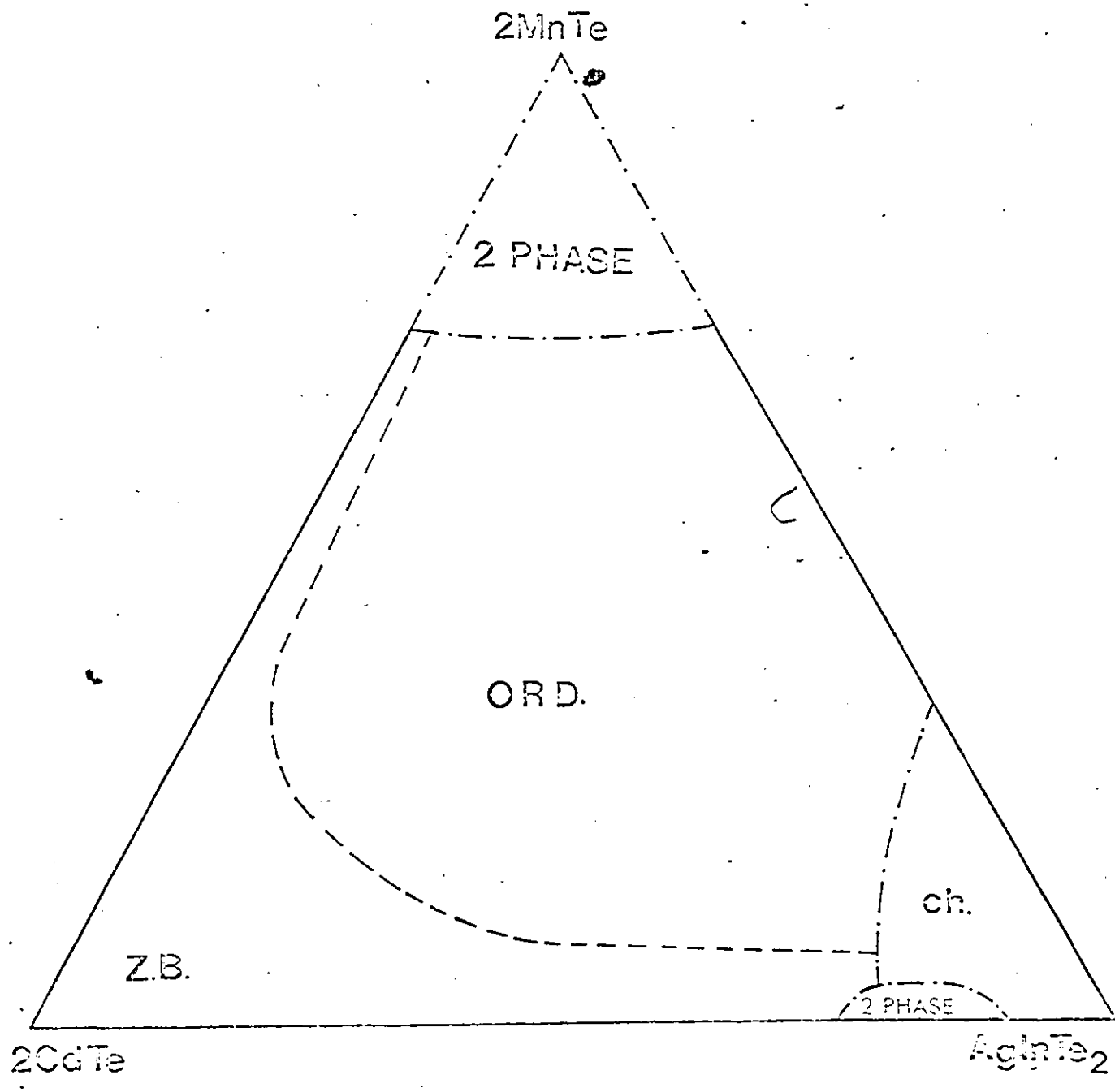

Fig. VII-14 $Cd_{2x}(AgIn)_{1-x}Mn_{1-x}Te_2$. Isothermal section for samples annealed at 600°C and quenched to room temperature. Dash-dotted lines indicate phase boundaries. Dash-dot line indicates the limit of the ordered field.

composition triangle, fig.(VII-14).

As in the case of the $Cd_{2x}(CuIn)_y Mn_{2z} Te_2$, some degree of ordering was observed for samples inside the composition diagram, the intensity of the ordering lines decreases as the z increases. Again, the range of ordered alloys could not be determined accurately from the X-ray results presented here, but could be found from the optical absorption measurements. This will be discussed in the next section.

It can be seen in fig.(VII-12) that the lines for five different x:y ratios all extrapolate at z=1 to a single value a=0.633 nm as in the case of the $Cd_{2x}(CuIn)_y Mn_{2z} Te_2$ system, representing the lattice parameter that MnTe would have in the ordered cubic phase. The limits of single phase solid solution, can be determined in the usual way and the values taken from fig.(VII-12) are used to draw the limits of solid solution shown in fig.(VII-14).

VII-3c ENERGY GAP RESULTS AND ANALYSIS

Energy gap values were determined as described above for most of the samples. Curves of $(\alpha h\nu)^2$ Vs $h\nu$ were drawn as with the Cu alloys. In fig.(VII-15) to (VII-17),

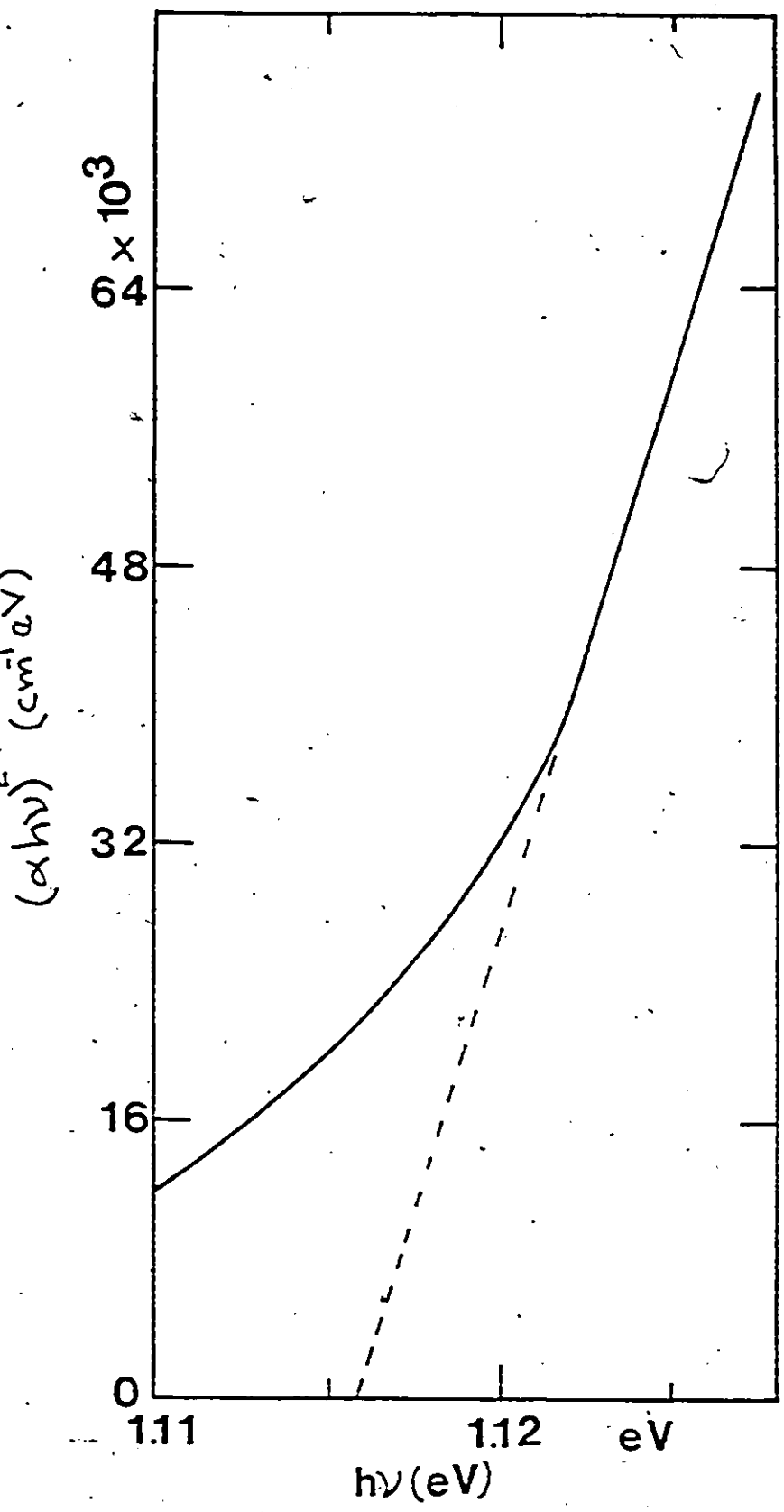

Fig. VII-15 $Cd_{2x}(AgIn)_yMn_{2z}Te_2$. $(\alpha h\nu)^2$ vs. hν curve for the sample y=0.85 z=0.15.

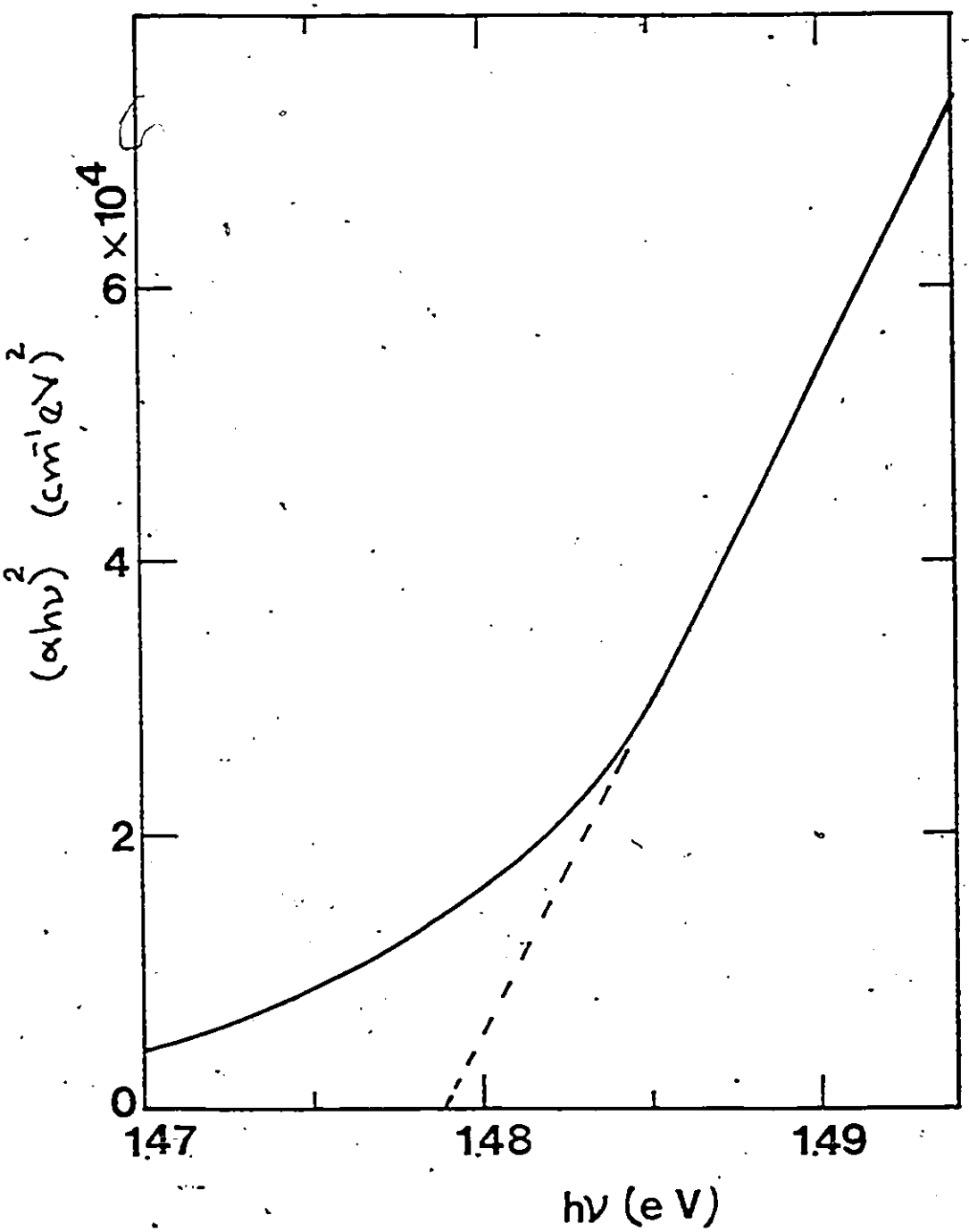

Fig. VII-16 $Cd_{2x}(AgIn)_y Mn_{2z} Te_2$. $(\alpha h\nu)^2$ vs. hν curve for the sample y=0.375 z=0.5.

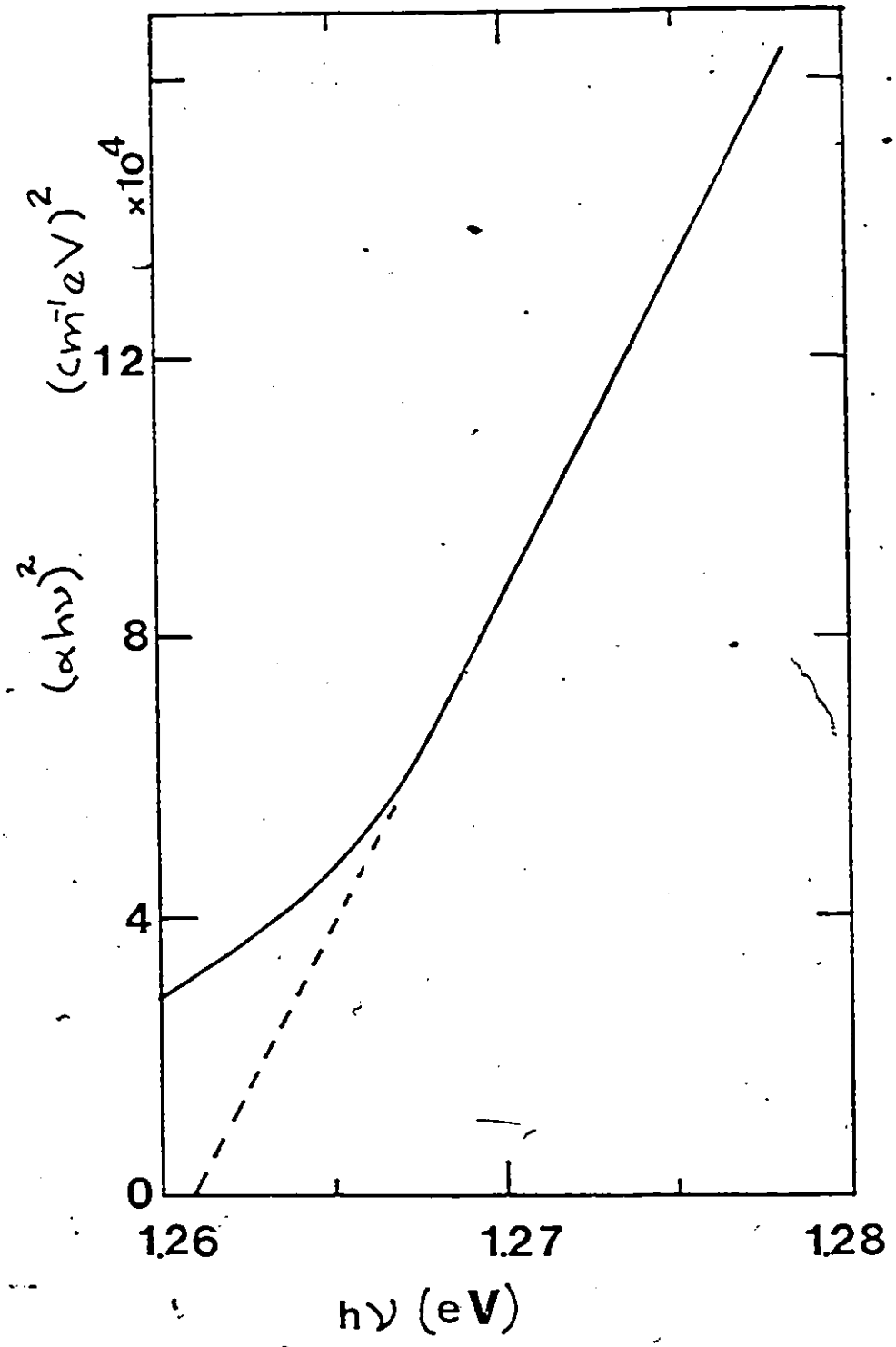

Fig. VII-17 $Cd_{2x}(AgIn)_y Mn_{2z} Te_2$. $(\alpha h\nu)^2$ vs. $h\nu$ curve for the sample y=0.4 z=0.2.

the absorption results for some typical samples of this system are shown, compositions being labeled on these graphs.

Figures (VII-18) and (VII-19) show the variation of the fundamental energy gap of this alloy system. Fig. (VII-18) giving the variation of E_o with x for constant z and fig.(VII-19) the variation of E_o with z for five different x:y ratios. It is seen in these figures that the lines for four x:y ratios, viz., x=0, y=3x, x=y, and x=3y intersect in a single point 1.9 eV at z=1, while the line y=0 extrapolates to a value of 2.8 eV at z=1. Also, it is seen in fig.(VII-19) that the chalcopyrite values of the line x=0 aim at a value of 1.35eV at z=1. As was done in the $Cd_{2x}(CuIn)_y Mn_{2z}Te_2$ case, the limits of the ordered phase field can be determined by considering the intersection between the lines that aim at 2.8 eV with those that aim at 1.9 eV. This is shown in figs.(VII-18) and (VII-19) and the approximate form of the ordered phase boundary is shown in figs.(VII-14) and (VII-18).

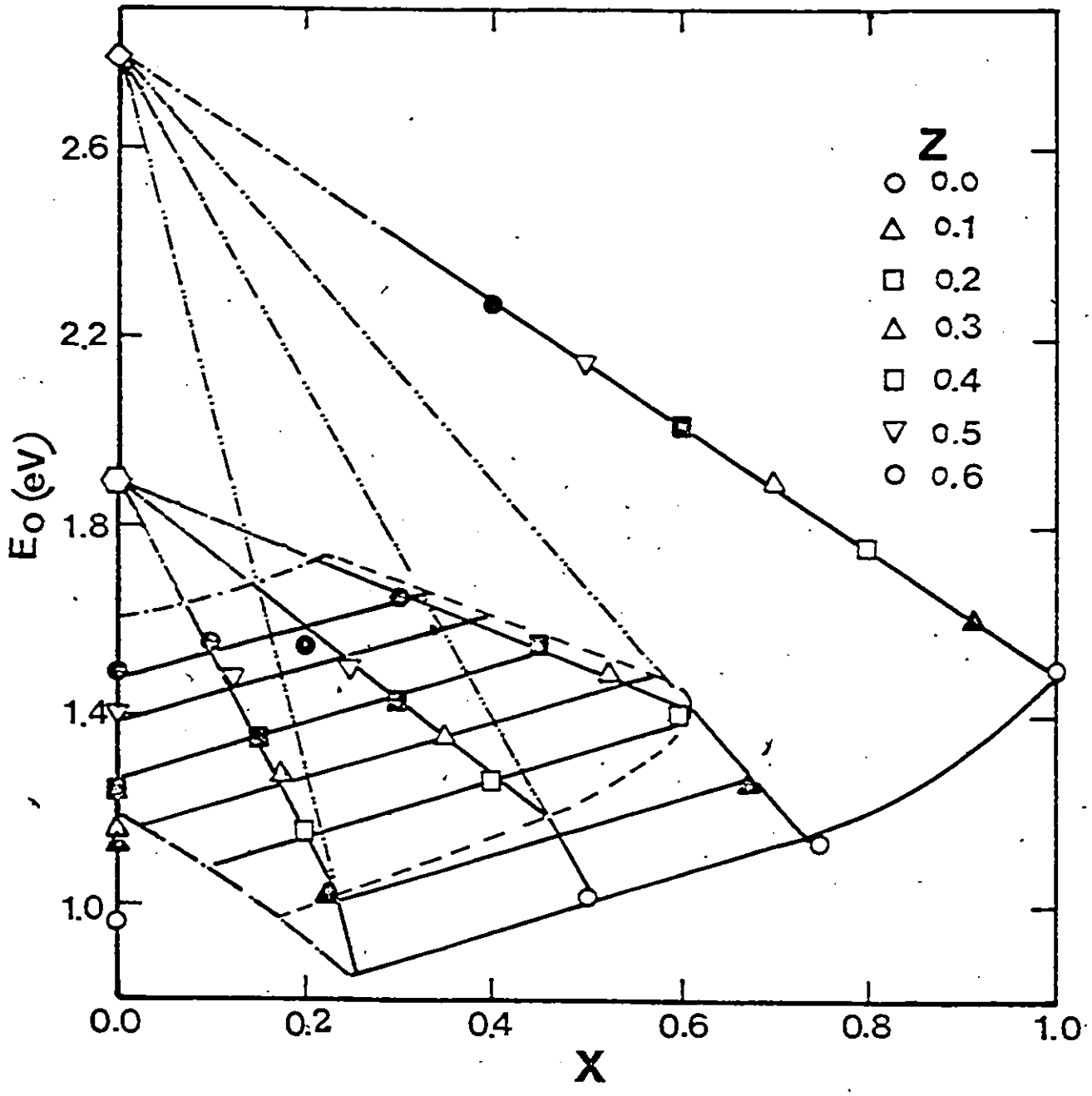

Fig. VII-18 $Cd_{2x}(AgIn)_yMn_{2z}Te_2$. Variation of E_o at 300K with x for various constant values of z, for samples showing single phase behavior. Dash-dotted lines are phase boundaries. Dash-double-dotted lines are extrapolation lines. Dash line indicates the limit of the ordered field.

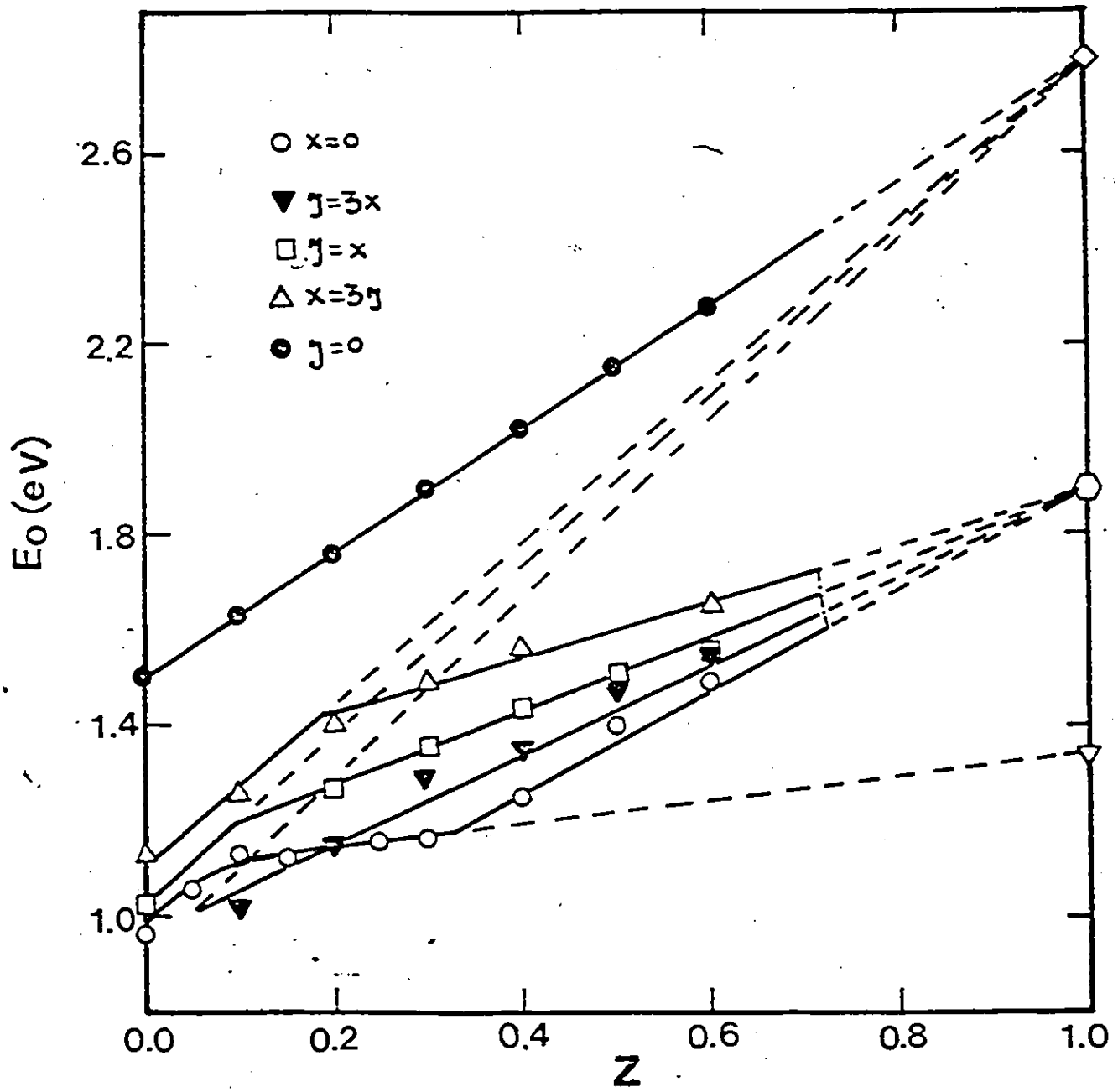

Fig. VII-19 $Cd_{2x}(AgIn)_yMn_{2z}Te_2$. Variation of E_o at 300K with z for various x:y ratios. Dash-dot line indicates the limit of single phase behavior. Dashed lines are extrapolation lines.

VII-4 DISCUSSION

Referring to the behavior of the variation of E_o vs composition for both systems, it can be seen in fig.(VII-8), (VII-9), (VII-18) and (VII-19) that the alloys inside the composition diagrams have a different aiming point from that of the pseudobinary edge $Cd_{1-z}Mn_zTe$ and the pseudoternary system $Cd_xZn_yMn_zTe$(83B1). It is considered unlikely that this difference of 0.9 eV between these two values is due to the presence of the noble metal d levels in these materials. This is illustrated in figs.(VII-9) and (VII-19), where it is seen that the energy difference between the values of E_o for $Cd_{1-z}Mn_zTe$ edge and the lines for several x:y ratios increases as the amount of Cu and/or Ag decreases. The contribution from the Mn d states to the valence band can not be the origin of that behavior, since the paramagnetic Mn ion is already involved in the pseudobinary edge y=0.

It has been shown in these $Cd_{2x}(CuIn)_yMn_{2z}Te_2$ and $Cd_{2x}(AgIn)_yMn_{2z}Te_2$ that the paramagnetic Mn ion orders in the cation sublattice giving b.c.c symmetry with a lattice parameter twice that for a zinc-blende structure (84W1), this is discussed further below, see figs.(VIII-13) and (VIII-14) of chapter VIII. Hence, the volume of the first

Brillouin zone of this ordered b.c.c structure will be four times smaller than that of the Brillouin zone of the zinc-blende f.c.c. structure. These changes, in structure and in size of the Brillouín zone of the ordered alloys as compared with the $Cd_{1-z}Mn_z$ Te alloys which have the zincblende structure, could affect the band structure, these changes being the origin of this observed reduction in the fundamental energy gap.

VII-d SUMMARY AND CONCLUSION

The variation of the lattice parameter with composition is typical of alloys of this type (83B1). The curved form of the pseudobinary edges x=0 and z=0 as well as the scattering of the data for the Ag system in the high y region probably has its origin in deviations from the ideal stoichiometric. The limits of single phase solid solution and of chalcopyrite phase were determined by X-ray diffraction. These powder X-ray results show that in each of the alloy systems investigated here, there is a phase field of ordered samples (b.c.c.). However, for both systems, the variation of the lattice parameter with composition gives a smooth curve across the complete composition range and hence the limit of the ordered field could not be determined from the variation of the lattice parameter values.

The form of the fundamental absorption edge of these semimagnetic alloys needs more investigation. To carry out the analysis of the type of transition occurring in these alloys further, thinner samples are required, so that higher values of the absorption coefficient can be obtained. The probable error in E_o, due to the lack of thinner specimens, is estimated to be around 50meV, thus the variation of the energy gap values with composition for these alloy systems will not be appreciably different from that presented here.

The range of the ordered field was well shown by the variation of the energy gap E_o with composition. This field occurs because in these alloys the paramagnetic Mn ion orders on the cation sublattice to give rise to a b.c.c. structure. It is to be noted that the ordered field extends to near the $Cd_{1-z}Mn_z$ Te edge so that more experimental work is required near this pseudobinary edge to determine the exact position of the boundary of the field. By observing the lines that extrapolate to the different aiming points at z=1.0, more information on this ordered phase range for these pseudoternary semimagnetic semiconductor alloys would be obtained.

The general composition diagram for the alloys

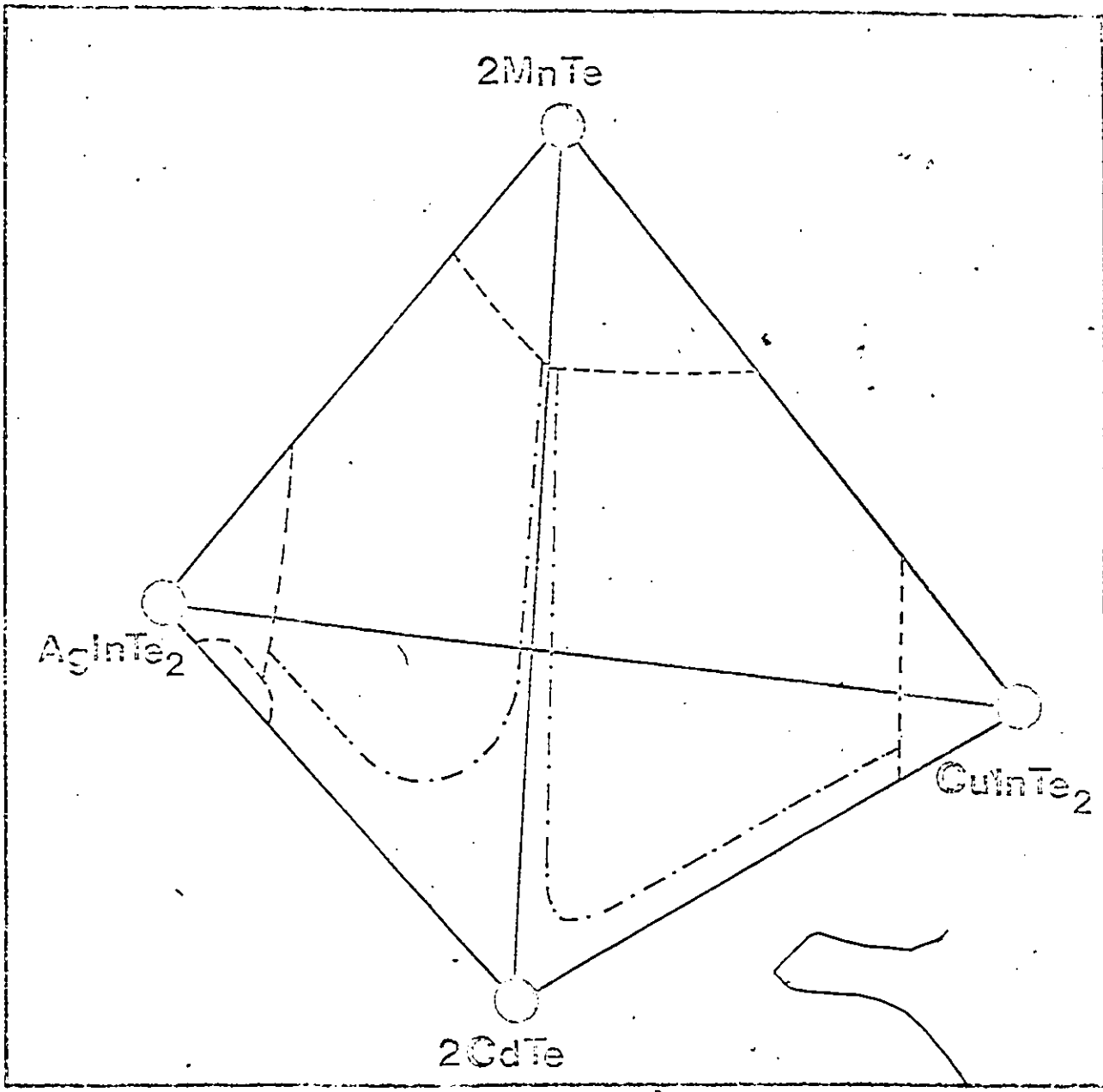

Fig. VII-20 CdTe-$CuInTe_2$-$AgInTe_2$-MnTe. General composition diagram for the alloys involved in this work. Dashed lines are phase boundaries. Dashed-dotted lines indicate the limits of the ordered phase for each system.

involved in this work is shown in fig.(VII-20). The dash-dotted line represents the phase boundaries and the dashed line represents the ordered phase field. To complete the work on this general composition diagram, the triangular system $Cu_xAg_yIn_{x+y}Mn_{2z}Te_2$ and as well as various sections such as the section $2(CdTe)_{2x} - (CuAgIn_2Te_4)_y - 2(MnTe)_{2z}$ inside of the diagram need to be investigated. This work will be carried out as a joint program between members of the department of physics of U.L.A (Merida) and the research group of U.O. (Ottawa).

CHAPTER VIII

MAGNETIC PROPERTIES IN $Cd_{2x}(CuIn)_y Mn_{2z} Te_2$ AND $Cd_{2x}(AgIn)_y Mn_{2z} Te_2$

VIII-1. INTRODUCTION

During the past two decades there has been a great deal of activity, both theoretical and experimental in regard to the magnetic properties of alloy semiconductors in which paramagnetic atoms are introduced into the material. Experimental studies on these materials showed the alloys to have typical spin-glass behaviour, so that at low temperatures the spins become locked in a random configuration. One experimental consequence of this is the observation of a sharp cusp in the low-field susceptibility at a temperature T_g, but no corresponding discontinuity in the magnetic specific heat.

Earlier measurements (80G1) (84D1) showed this type of behaviour for the pseudobinary edge y=0. Similar magnetic results have been found for a number of SMSA already investigated. Examples of such materials are $Zn_{1-z}Mn_zTe$, $Hg_{1-z}Mn_zTe$, $Cd_{1-z}Mn_zSe$, $Zn_{1-z}Mn_zSe$, $Cd_{1-z}Mn_zS$, $Zn_{1-z}Mn_zS$, etc.. For the

$(II-VI)_2-(Mn-VI)_2-(I-III-VI_2)$ alloys investigated here, at the present time, there are no published results on their physical properties. These materials are expected to have magnetic properties similar to those of the (II-VI)-(Mn-VI) alloys with respect to the characteristics of the cusp observed in the susceptibility data described above. Thus it is of interest to make magnetization measurements on these SMSA, so that data will be available and some insight into the type of exchange interaction between the Mn ions can be obtained.

In the present chapter, low field measurements of susceptibility χ that have been made as a function of temperature in the range 4 to 100K are reported. Values of T_g and θ, the spin-glass transition temperature and Curie-Weiss constant respectively, have been obtained, and the values of T_g are analyzed in terms of an equation proposed by Escorne et. al.(81E1).

VIII-2 EXPERIMENTAL MEASUREMENTS AND RESULTS

The experimental measurements of magnetic susceptibility were made in the laboratory of "Low Temperature physics" of the department of physics. The cryostat and experimental system used in these measurements was designed and built by Dr. Gilles Lamarche. In the present work, a small contribution to this system was made by improving the method of handling the data.

The susceptibility χ was measured with a superconducting quantum interference device (SQUID) magnetometer at a steady magnetic field in the range of 1 to 2.5 mT when the temperature was varied between 4 and 100K. The value of the magnetization at a given temperature was measured by passing the sample placed in a cylindrical copper container several times through a pair of oppositely wound coils and taking the appropriate average.

Measurements were made on the same polycrystalline samples as were used in chapter VII. A well defined cusp in the susceptibility measurements as a function of the temperature was observed for specimens having $z>0.2$. For

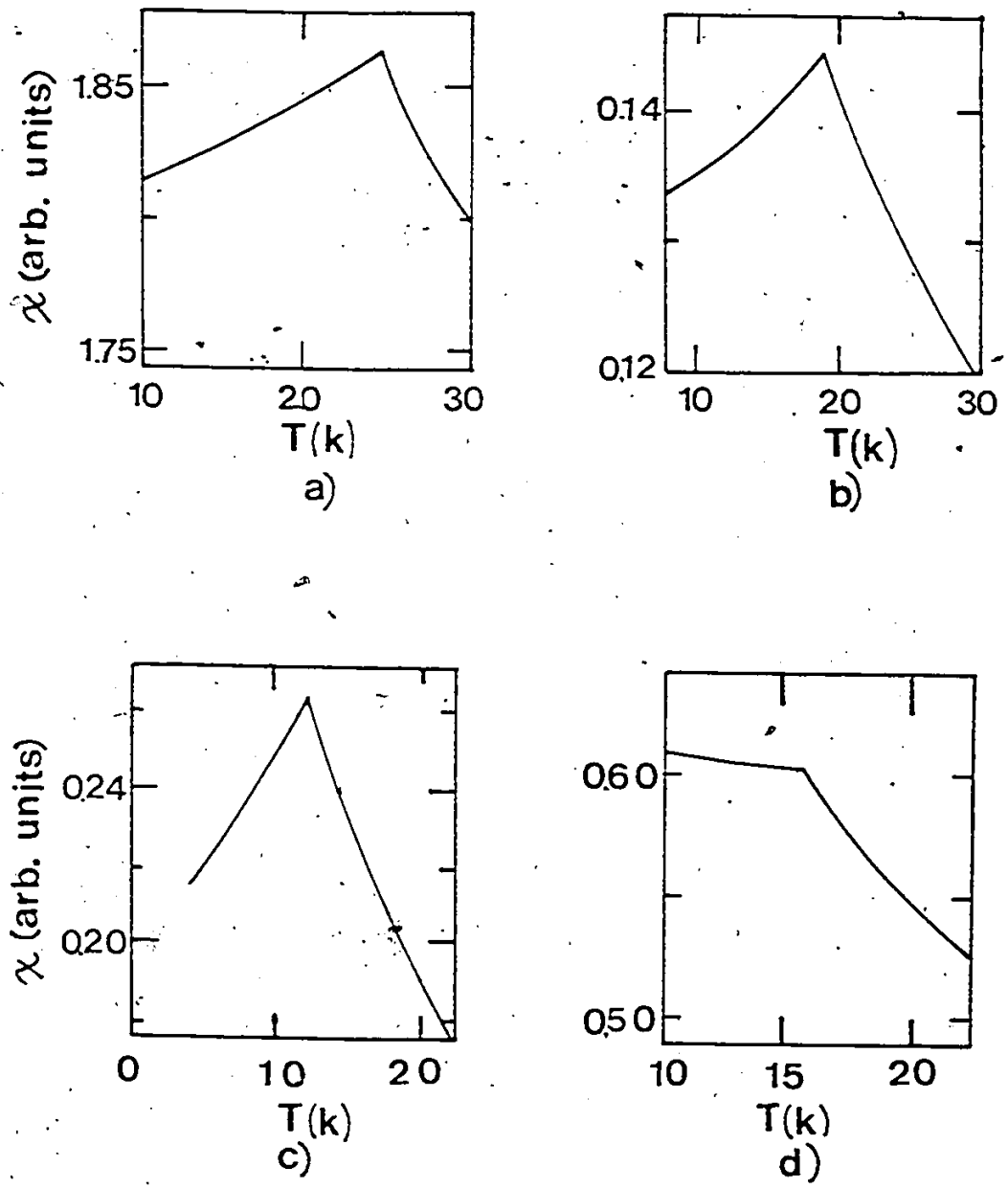

Fig. VIII-1 $Cd_{2x}(CuIn)_y Mn_{2z}Te_2$. Variation of the magnetic susceptibility χ with temperature T for several samples with x=0. a) y=0.5 z=0.5. b) y=0.6 z=0.4. c) y=0.7 z=0.3. d) y=0.75 z=0.25.

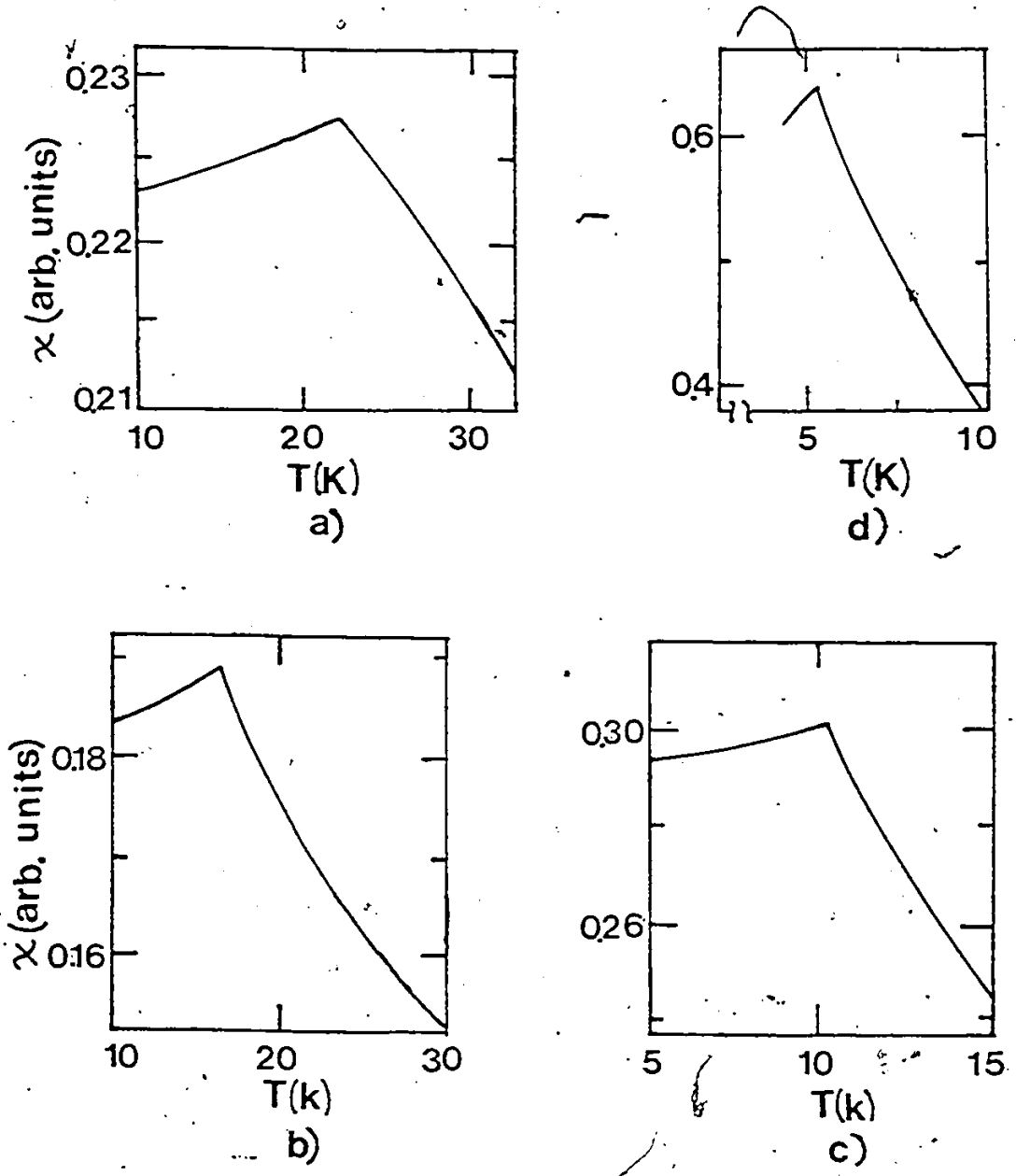

Fig. VIII-2 $Cd_{2x}(CuIn)_y Mn_{2z}Te_2$. Variation of the magnetic susceptibility χ with temperature T for several samples with y=3x. a) y=0.375 z=0.5. b) y=0.45 z=0.40. c) y=0.525 z=0.3. d) y=0.6 z=0.2.

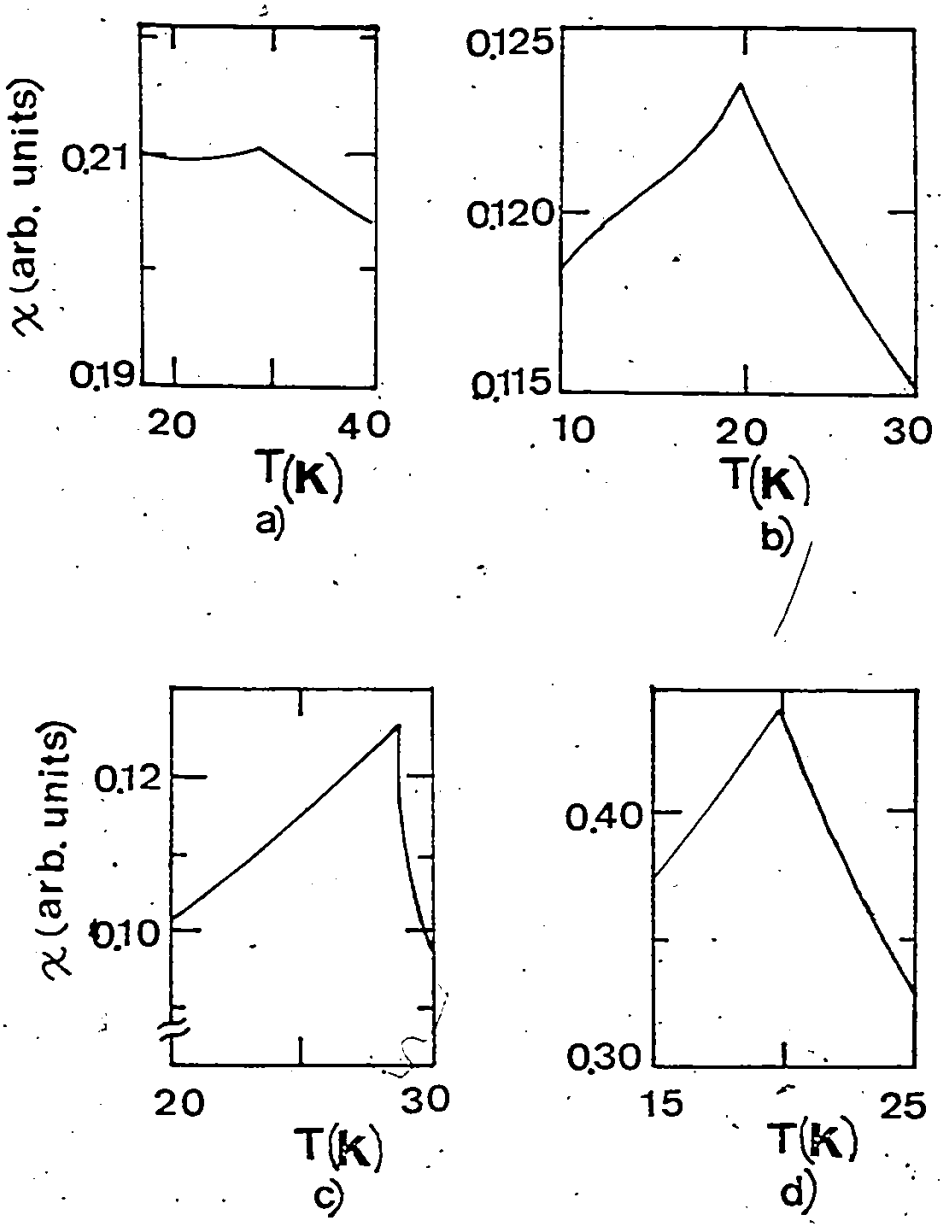

Fig. VIII-3 $Cd_{2x}(AgIn)_y Mn_{2z} Te_2$. Variation of the magnetic susceptibility χ with temperature T for several samples with x=0. a) y=0.4 z=0.6. b) y=0.5 z=0.5. c) y=0.7 z=0.3. d) y=0.75 z=0.25.

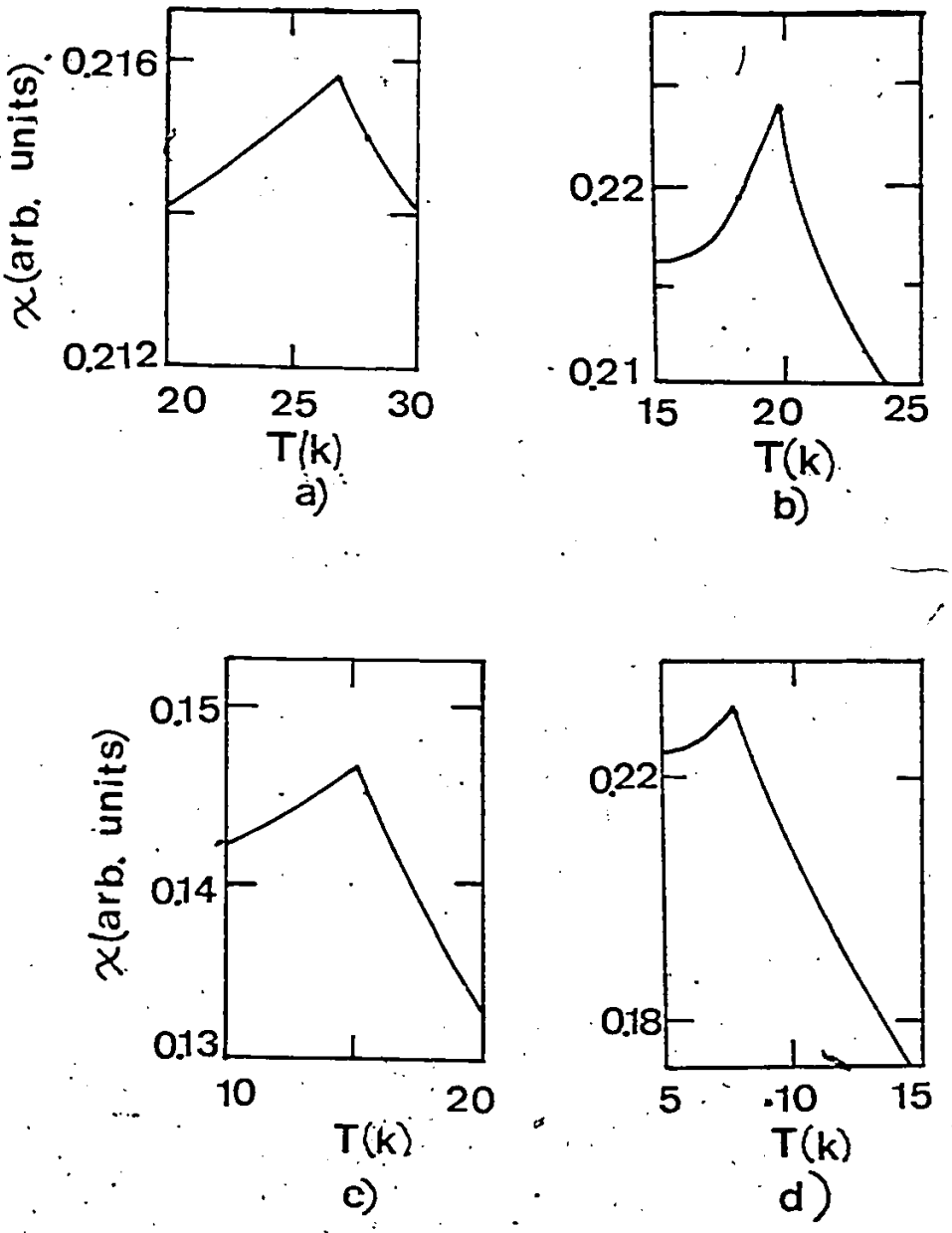

Fig. VIII-4 $Cd_{2x}(AgIn)_y Mn_{2z} Te_2$. Variation of the magnetic susceptibility χ with temperature T for several samples with $y=3x$. a) $y=0.3$ $z=0.6$. b) $y=0.375$ $z=0.5$. c) $y=0.45$ $z=0.4$. d) $y=0.525$ $z=0.3$.

samples with $z < 0.2$, no cusp was observed in the temperature range investigated here, thus no transition temperature could be observed for these low manganese composition samples. In figs.(VIII-1), (VIII-2), (VIII-3), and (VIII-4), typical results of magnetic susceptibility of some of the samples lying on the lines x=0 and y=3x respectively for both systems are presented. From these figures, it can be seen that the magnetic susceptibility shows a discontinuity at a well defined temperature T_g which increases with increasing Mn concentration and that at the higher values of z the variation of the magnetic susceptibility in a temperature range of ± 10K around the peak is very small, being about 2%. In general, most of the samples showed differences between the susceptibility measurements for the zero field cooled samples (ZFC) and those of cooled in a magnetic field (FC). For samples of composition $z>0.5$ these hysteresis effects were present both above and below T_g extending up to about $2T_g$, but for samples with $z<0.5$ the temperature hysteresis was observed only below T_g. This is illustrated in figs.(VIII-5) and (VIII-6).

The variation of T_g with the composition variable y for lines of constant z is plotted in figs.(VIII-7) and (VIII-8) for the $Cd_{2x}(CuIn)_y Mn_{2z} Te_2$ and $Cd_{2x}(AgIn)_y Mn_{2z} Te_2$ systems respectively. It is seen that T_g varies slightly

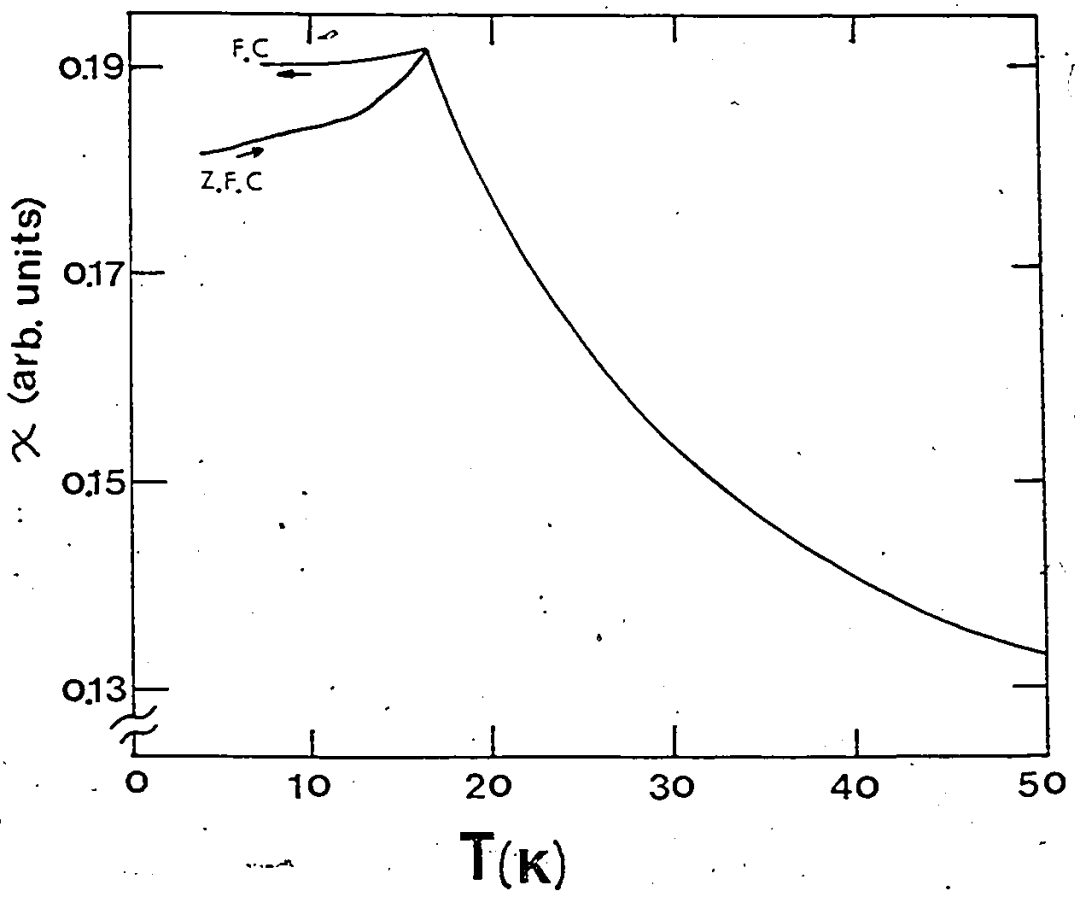

Fig. VIII-5 $Cd_{2x}(CuIn)_y Mn_{2z} Te_2$. Variation of magnetic susceptibility χ with temperature T for a typical sample y=0.45 z=0.40. The zero field cooled and field cooled effects are shown.

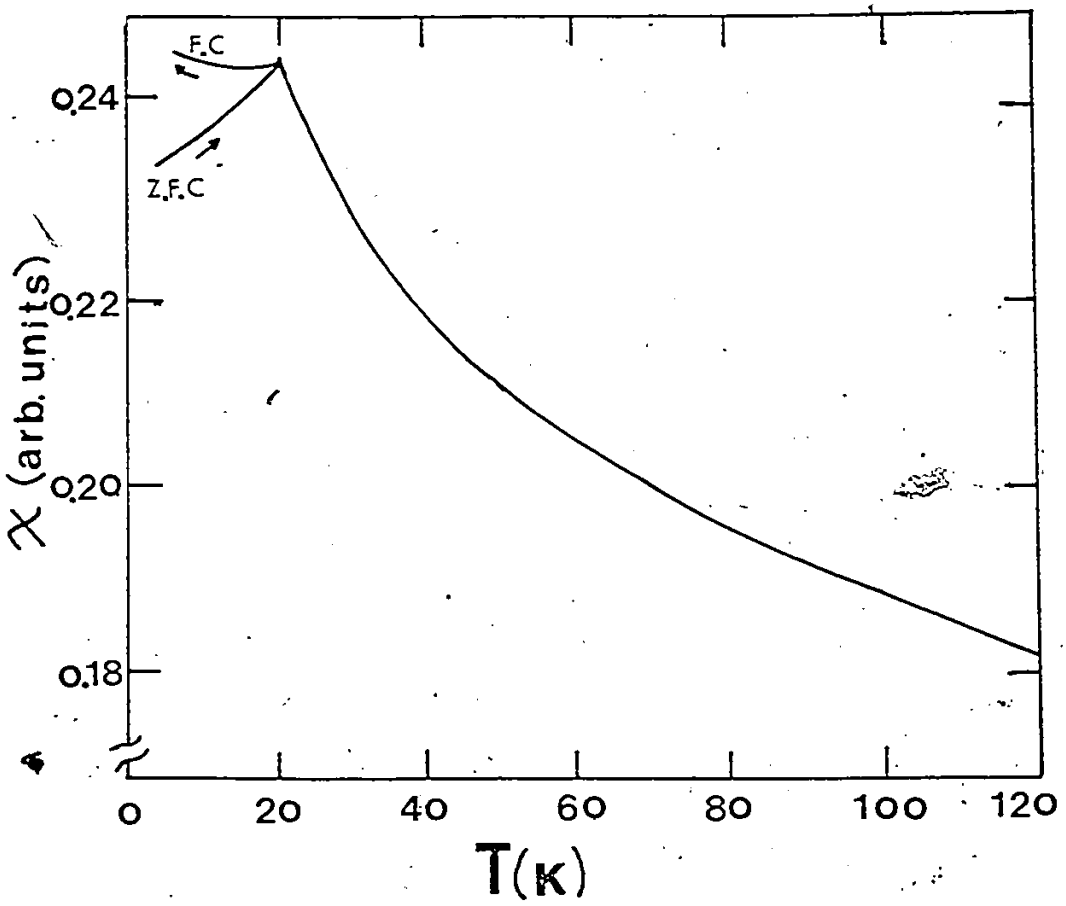

Fig. VIII-6 $Cd_{2x}(AgIn)_y Mn_{2z} Te_2$. Variation of magnetic suscetibility χ with temperature T for a typical sample y=0.25 z=0.50. The zero field cooled and field cooled effects are shown.

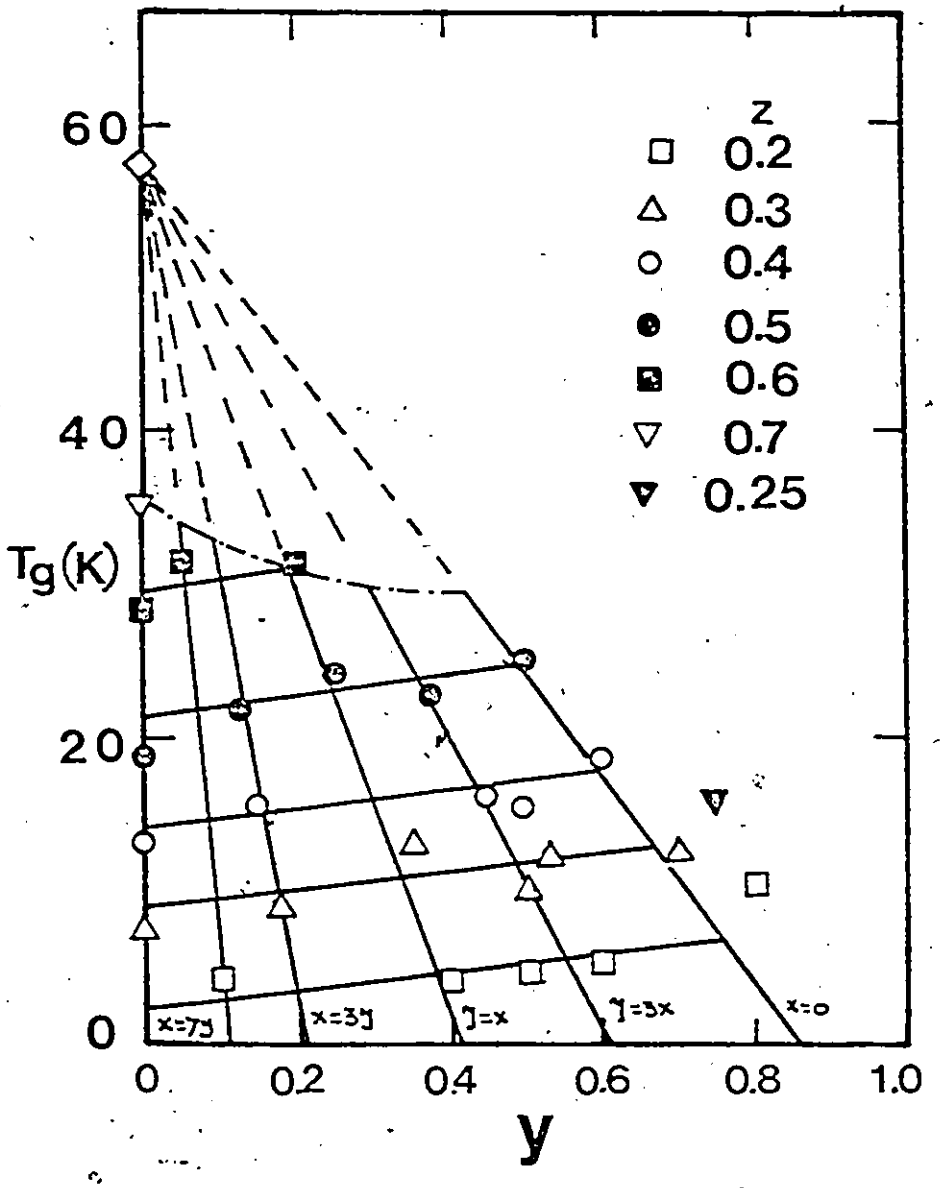

Fig. VIII-7 $Cd_{2x}(CuIn)_y Mn_{2z} Te_2$. Variation of the transition temperature T_g with y for various constant values of z.

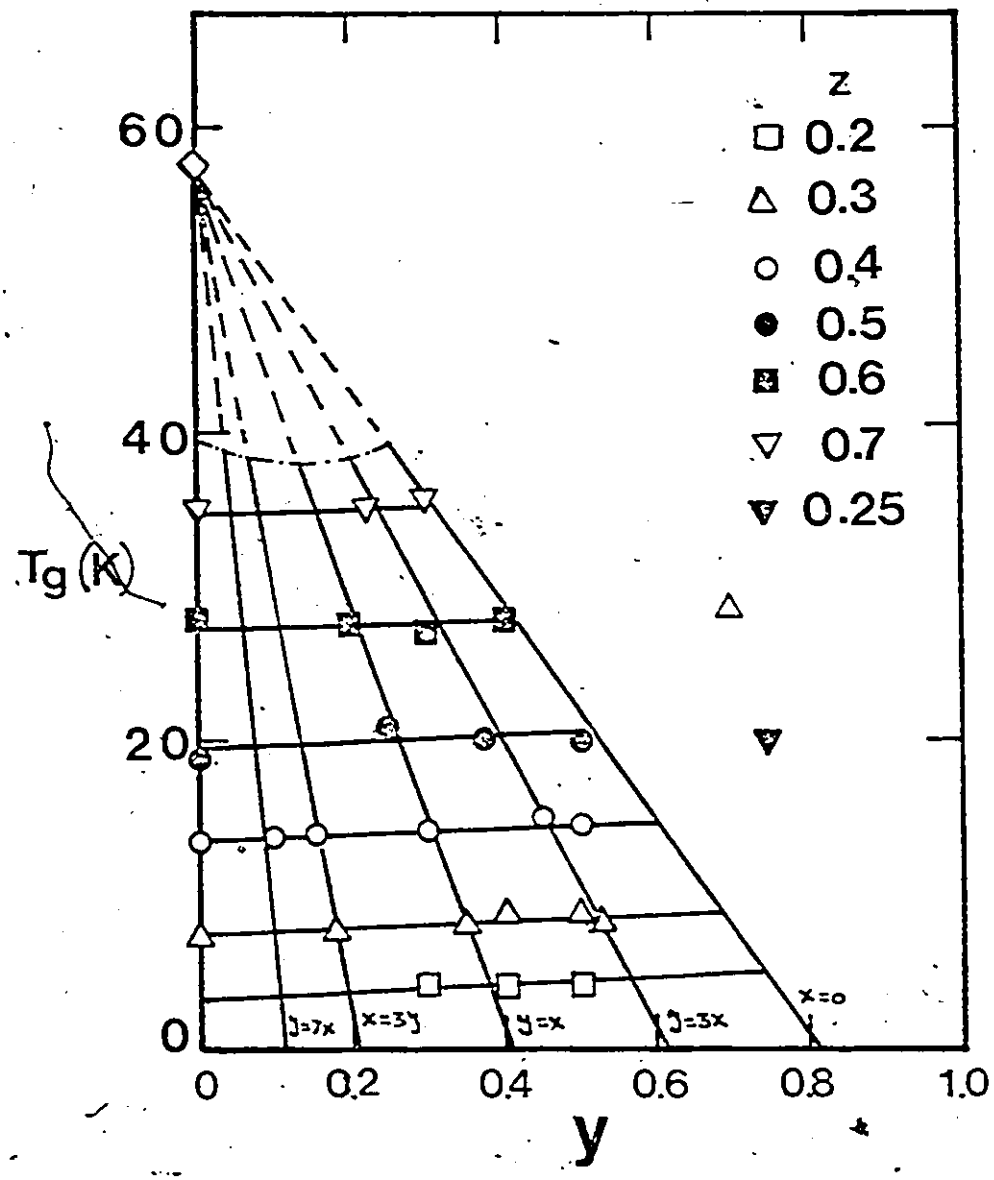

Fig. VIII-8 $Cd_{2x}(AgIn)_yMn_{2z}Te_2$. Variation of the transition temperature T_g with y for various constant values of z.

as y is varied at constant z, this variation is small and is almost masked by experimental fluctuations in T probably due to annealing conditions and small deviation from stoichiometry which are present in these materials. However in these figures, it is seen that straight lines drawn through the composition points corresponding to the pseudo-binary lines $x=0$, $3x=y$, $x=y$ and $x=3y$ intercept the y axis at a value of $z(=1-x-y)$ of about 0.18 0.01, hence suggesting this value is the nearest neighbour percolation limit for both of the systems. This percolation limit can also be observed in figs.(VIII-9) and (VIII-10) where T_g is plotted against z for all of the specimens of each system, the extrapolation of T_g to zero gives the value z=0.18. This result is in agreement with that of Donofrio et. al.(85D1) obtained on $Cd_x\ Zn_y\ Mn_z\ Te$, and in general with those for a series of semimagnetic semiconductor alloys of the type referred to above, i.e. $Hg_x\ Cd_y Mn_z Te$, $(Cd_{1-x}\ Mn_x)(Se_{1-y}Te_y)$, etc., which at the present time are being investigated in this laboratory.

In figs.(VIII-11) and (VIII-12), the variation of the inverse of the susceptibility $1/\chi$ is shown as a function of temperature for typical samples of these systems. The Curie Weiss of the equation $\chi=C/(T-\theta)$ was obtained for the various alloys by extrapolating the higher temperature part back to zero $1/\chi$, hence the

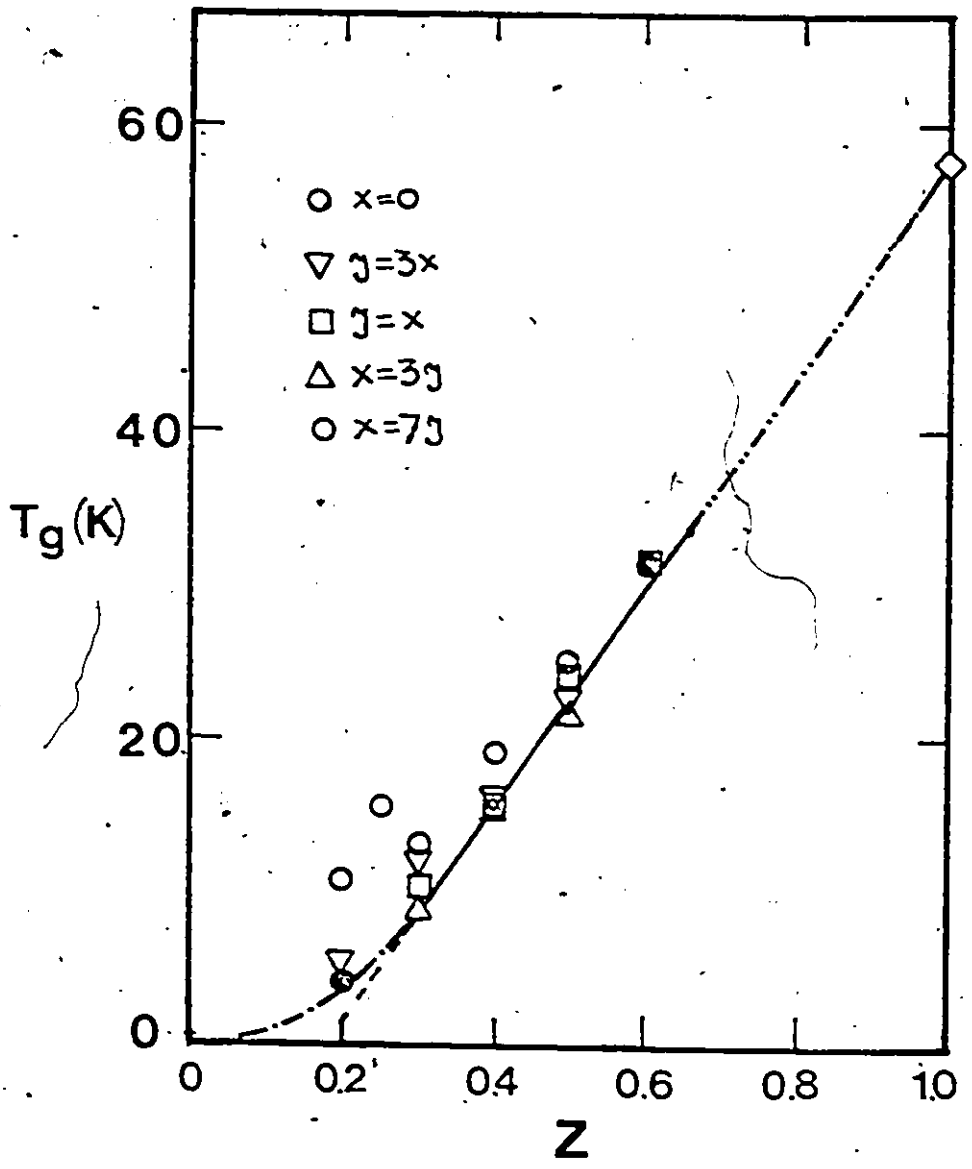

Fig. VIII-9 $Cd_{2x}(CuIn)_yMn_{2z}Te_2$. Variation of the transition temperature T_g with z for various x:y ratios. The dash-dotted line is obtained by fitting the data in the range $0.25<z<0.6$ with eq. (VIII-6).

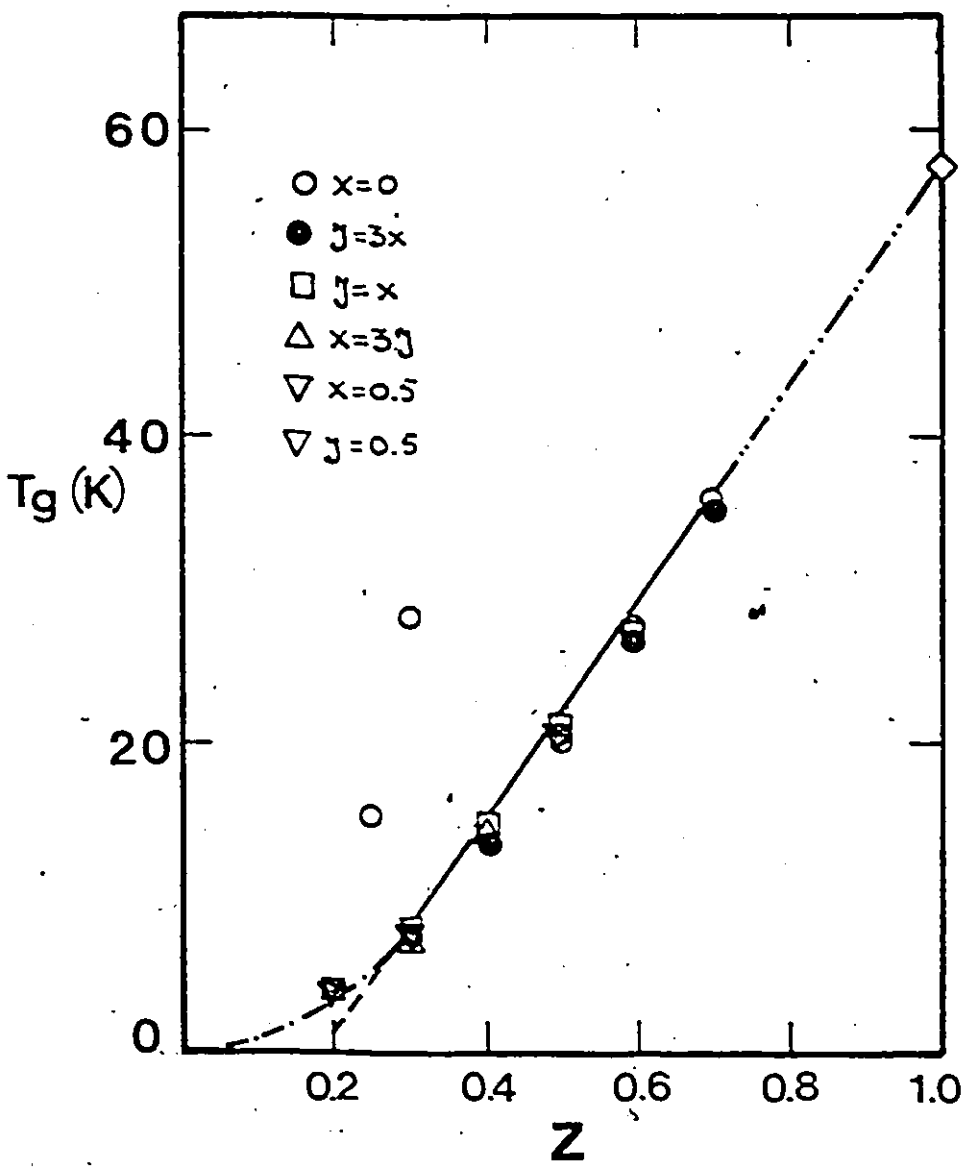

Fig. VIII-10 $Cd_{2x}(AgIn)_y Mn_{2z} Te_2$. Variation of the transition temperature T_g with z for various x:y ratios. The dash-dotted line is obtained by fitting the experimental data for $z>0.25$ with eq. (VIII-6).

intersection of this extrapolated line with the temperature axis gave values for θ . For both systems, $1/\chi$ was found to intersect the negative axis, i.e. θ is negative, indicating that the dominant interaction is antiferromagnetic over all the compositions measured. The values of θ for various y at constant z so found showed larger scatter than was the case for T_g, so that any systematic variation of θ with y was completely masked. It should be noted that the accuracy of these long extrapolations in temperature is not too high, particularly since deviations from Curie-Weiss linear form occur at temperatures well above T_g . It has been suggested that this deviation is due to superparamagnetic behavior of magnetic clusters which begin to align as the temperature is lowered from higher values(84D1). To facilitate future comparison with new experimental results and theoretical developments, the observed values of θ are listed in tables 1 and 2 together with the values of T_g for both systems.

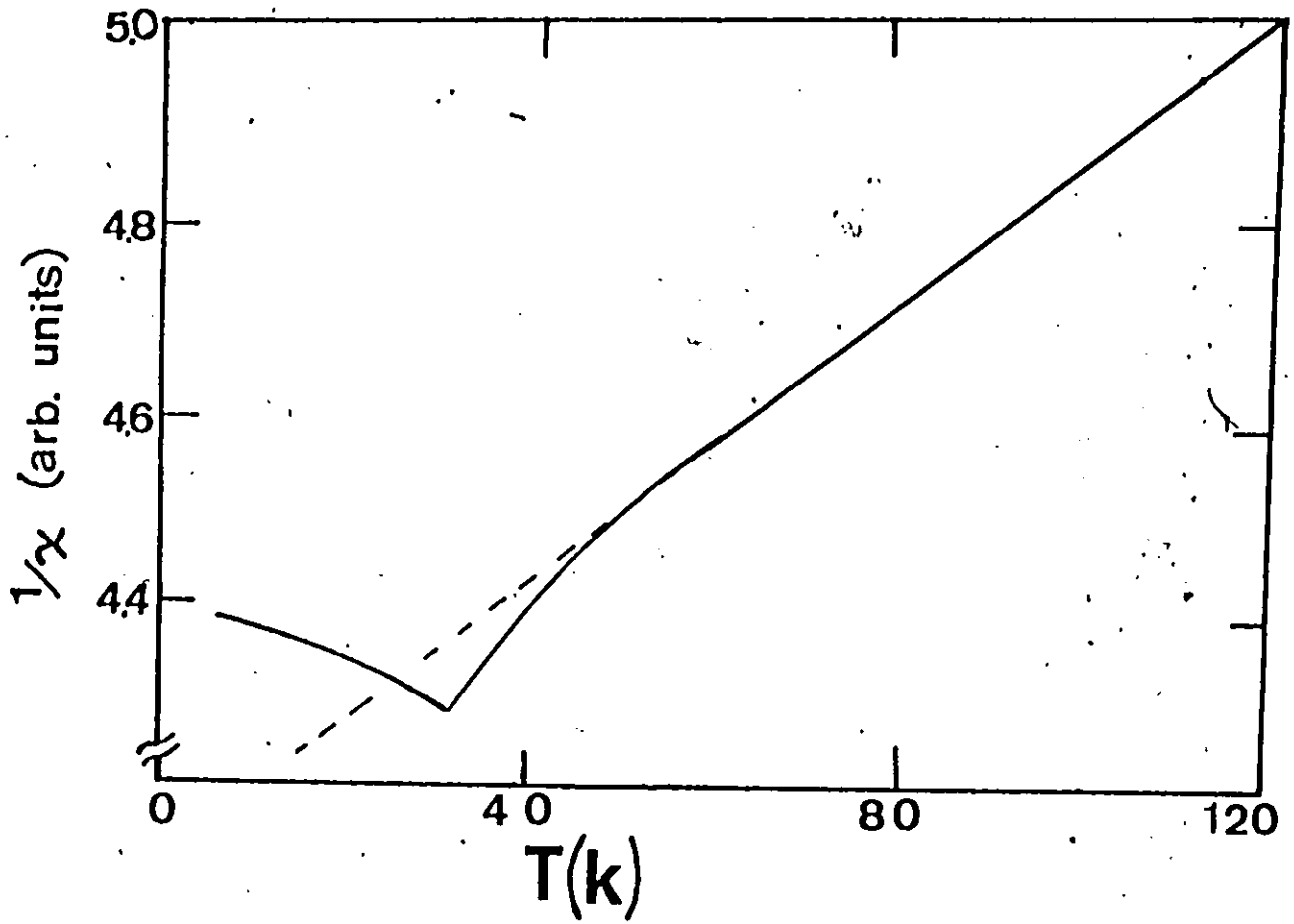

Fig. VIII-11 Cd_{2x} $(CuIn)_y$ Mn_{2z} Te_2 . Typical variation of the inverse of the susceptibility $1/\chi$ with temperature. The sample y=0.2 z=0.6 for which T =32 K and θ =535.7 K.

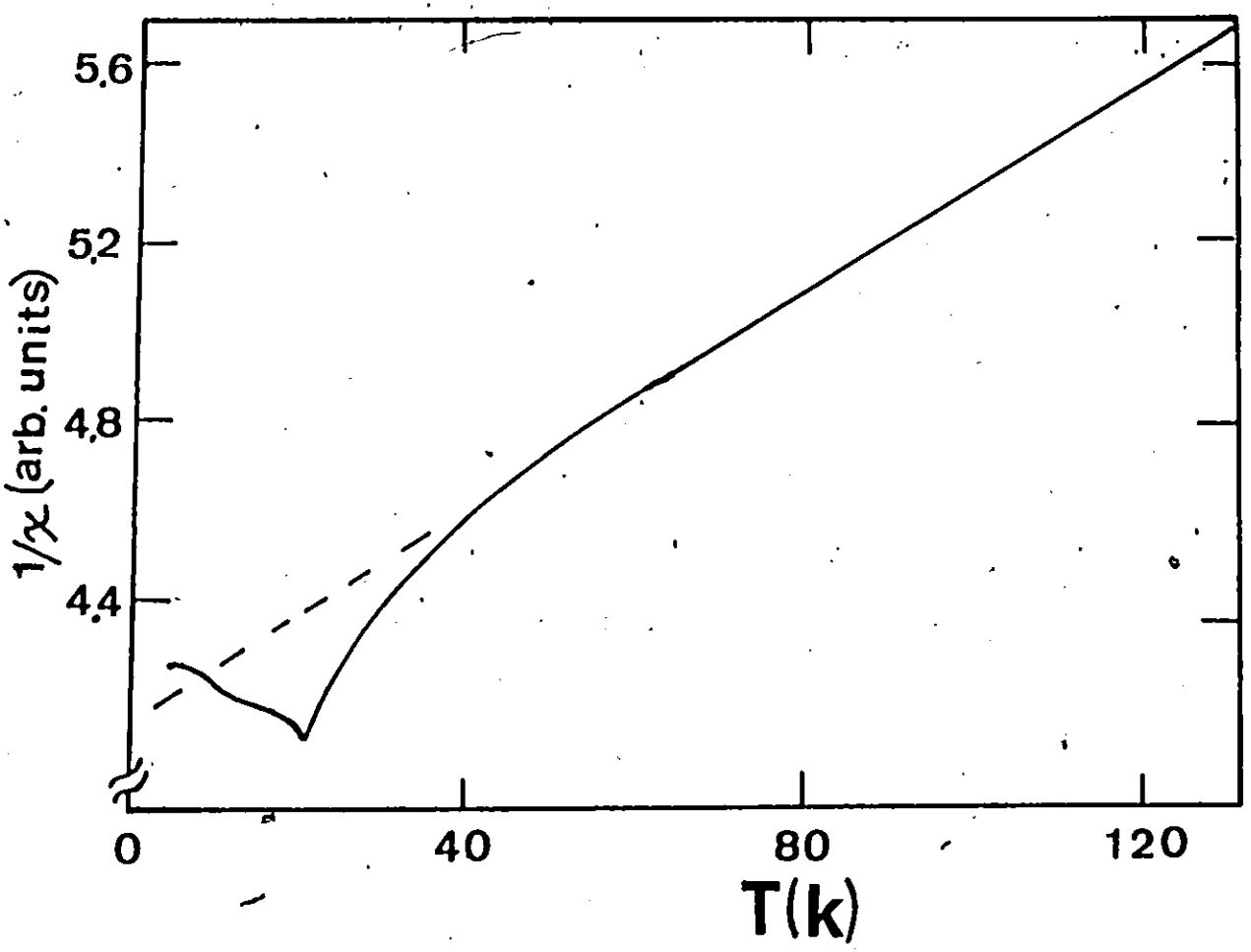

Fig. VIII-12 Cd_{2x} $(AgIn)_y$ Mn_{2z} Te_2 . Typical variation of the inverse of the susceptibility $1/\chi$ with temperature. The sample y=0.25 z=0.5 for which T =22 K and $^{\theta}$ =370.5 K.

Table VIII-1. Values of the transition temperature T_g and the Curie-Weiss θ for various alloys.

$$Cd_{2x}(CuIn)_y Mn_{2z} Te_2$$

y/z	T_g (K)	θ (K)
0.80/0.20	10.50	
0.75/0.25	15.60	
0.70/.030	12.50	
0.60/0.40	18.50	200.00
0.50/0.50	25.00	379.00
0.60/0.20	5.05	8.50
0.525/0.30	10.20	32.36
0.45/0.40	16.30	130.99
0.375/0.50	22.50	183.13
0.40/0.20	<4.20	
0.35/0.30	10.30	113.50
0.25/0.50	24.10	
0.20/0.60	31.30	535.70
0.175/0.30	8.75	71.00
0.15/0.40	15.50	170.30
0.125/0.50	21.50	294.74
0.05/0.60	31.30	
0.10/0.20	<4.20	26.75

TABLE VIII-2. Values of the temperature transition T_g and the Curie-Weiss θ for various alloys.

$Cd_{2x}(AgIn)_y Mn_{2z} Te_2$

y/z	T_g (K)	θ (K)
0.75/0.25	20.00	
0.70/0.30	28.80	
0.50/0.50	20.00	347.17
0.40/0.60	27.70	
0.525/0.30	7.50	82.68
0.45/0.40	15.00	114.34
0.375/0.50	20.05	
0.30/0.60	27.10	
0.40/0.20	<4.00	
0.35/0.30	8.00	73.30
0.25/0.50	20.90	370.5
0.20/0.60	27.50	
0.175/0.30	7.45	61.90
0.15/0.40	13.50	

VIII-3 DISCUSSION

The nature of the exchange interaction between Mn-Mn ions in these SMSA is not well known. It may be seen that the direct exchange interaction via Mn-Mn is unlikely because of the large distances involved between manganese ions. Superexchange interaction using atomic wave functions of anion valence electrons can be ruled out because of the total delocalization of the p electrons of anion atoms which form the valence bands of these materials. With regard to the SMSA under consideration, several descriptions of the exchange interaction via conduction electrons have been made in terms of band theory and corresponding one-electron Bloch function (79B1). On this basis, when there is a large number of free carriers, as in the case of narrow gap semiconductors, the exchange interaction is described by the well known oscillating RKKY function (54R1) (79B1), but these conditions do not apply here. In the case of open gap semiconductors, which are of direct concern in this discussion, the experimental results have been analyzed by using an empirical equation proposed by Escorne et. al. (81E1) which will be the main subject of this discussion.

The values of T_g and the lattice parameter found in chapter VII can be used to study the type of exchange interaction between Mn ions in these SMSA. Escorne et. al. (81E1) have suggested that the exchange interaction may be written in the form,

$$J(R_{ij}) = J_o \exp(-\alpha R_{ij}) \qquad \text{(VIII-1)}$$

Also they consider that the spin system will be frozen at temperature T_g such that $J(R_o) \dashrightarrow K_B T_g$ where R_o is the mean distance between Mn ions. In the case of materials in which the Mn ions are in random configuration, the mean volume occupied by a manganese ion can be written as,

$$4/3\ (R_o/2)^3 = (V/nz) \qquad \text{(VIII-2)}$$

where V is the volume of the unit cell and n is the number of cations in a unit cell. In the case of face centred cubic materials such as zincblende $V/n=a^3/4$, where a is the lattice parameter and hence

$$4/3\pi(R_o/2)^3 = a^3/4z \qquad \text{(VIII-3)}$$

as indicated by Escorne et. al., thus

$$R_o = (3/2\pi)^{1/3} a z^{-1/3} \qquad \text{(VIII-4)}$$

In general, the mean distance R_o between a pair of cations in a structure may be written as

$$R_o = qa_e z^{-1/3} \qquad \text{(VIII-5)}$$

where $V/n=a_e^3/4$ and q is a geometrical factor which depends on the configuration of the cations in the crystal, and a_e is the effective lattice parameter of the concerned structure this leads to the general relation,

$$\text{Ln } T_g = -\alpha q a_e z^{-1/3} + \text{Ln}(J_o/K_B) \qquad \text{(VIII-6)}$$

where $q=(3/2\pi)^{1/3}$ for zincblende materials.

In the case of the present ordered alloys, at low values of z the Mn ions occupy a cation sublattice which contains six cation sites out of a total number of 32 in the unit cell. This is illustrated in fig.(VIII-13) and (VIII-14), in which a perspective drawing as well as a planar map of the b.c.c. structure in which these samples crystallize are shown. This structure is formed by four sublattices; three of these are occupied by cations, A, B and C, and one is occupied by anions which are not shown in these figures. For low values of z, i.e. $z<6/32$ the manganese ions will occupy, at random, sites on the B

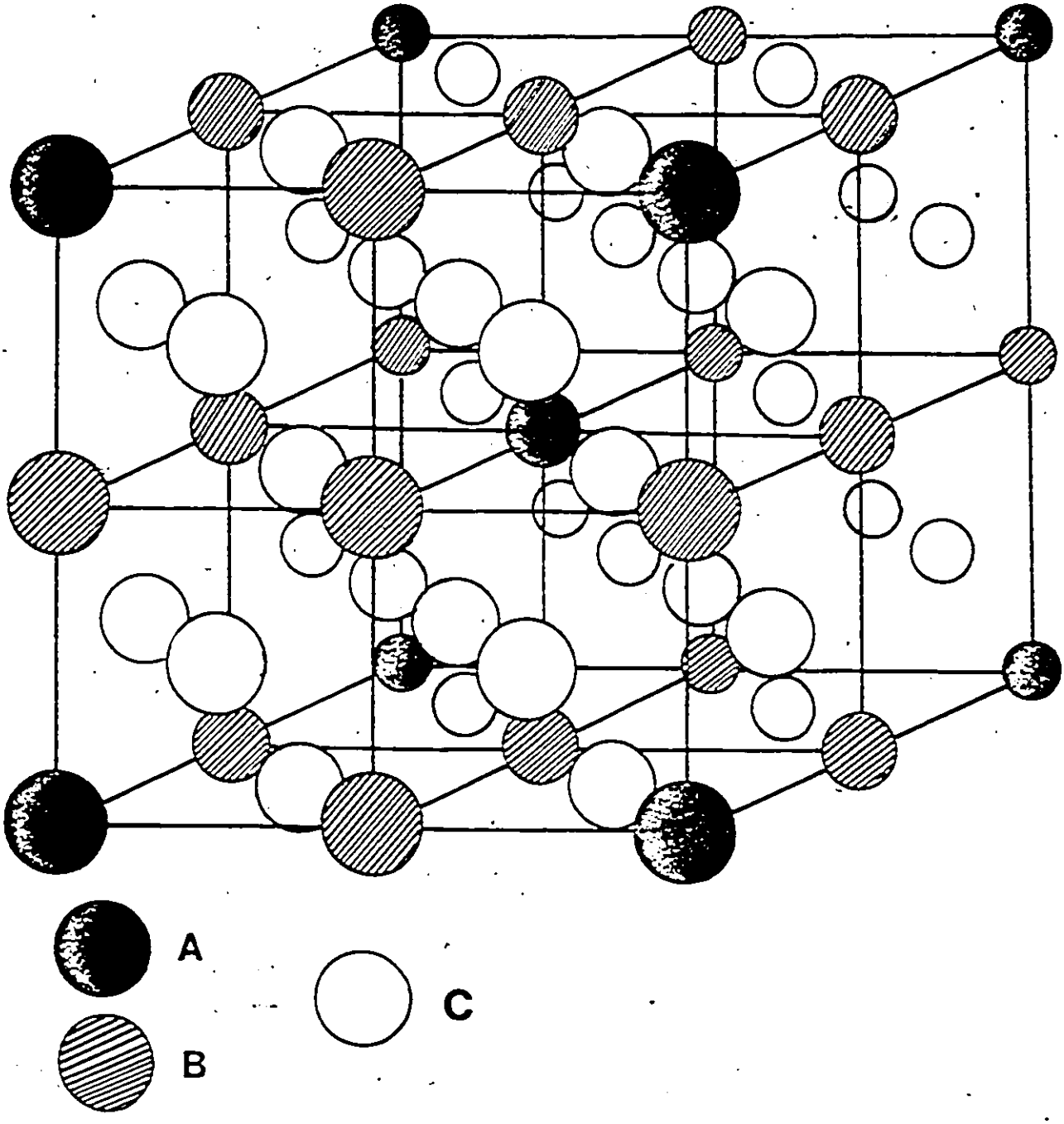

Fig. VIII-13 Perspective drawing of the b.c.c unit cell of the ordered structure. The number of cations is 32. The anions are not shown.

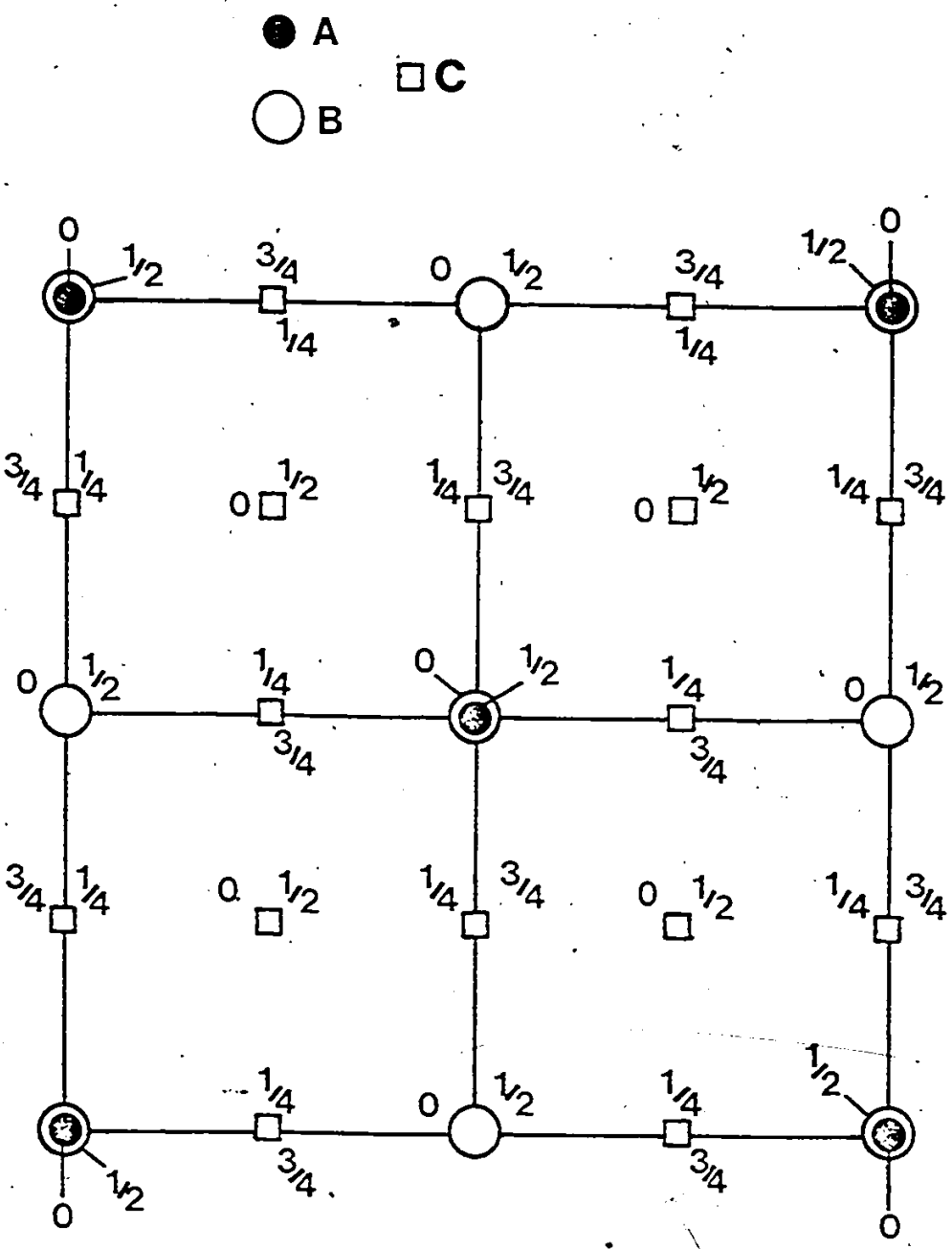

Fig. VIII-14 Ordered body centered cubic structure: projection of crystallography positions on c face.

sublattice only, and for the composition z=6/32 the Mn ions will ideally fill and occupy all of the positions on the B cation sublattice. For Mn concentrations higher than z=6/32 the manganese ions start to randomly occupy positions on the A and C cation sublattices shown in fig.(VIII-13). This proposed arrangement of the manganese ions is consistent with the variation of the intensity of the ordering lines with composition described in chapter VII. In the case of the ordered structure at z=6/32, the next nearest neighbour distance R_o between Mn ions will be equal a. With this information, the value of p for low values of z may be found using eq.(VIII-5), i.e.,

$$R_o = qaz^{-1/3} = a \quad \text{at } z=6/32$$

the value of q in this ordered condition is then given by

$$q=(6/32)^{1/3} \qquad \text{(VIII-7)}$$

and the mean distance R_o for low concentrations of manganese (i.e. z<6/32) is

$$R_o = (6/32)^{1/3} az^{-1/3} \qquad \text{(VIII-8)}$$

The values of Ln T_g as a function of $az^{-1/3}$ are plotted in fig.(VIII-15) where the values of the ordered alloys and chalcopyrite samples for both of the systems investigated in this work as well as an effective line

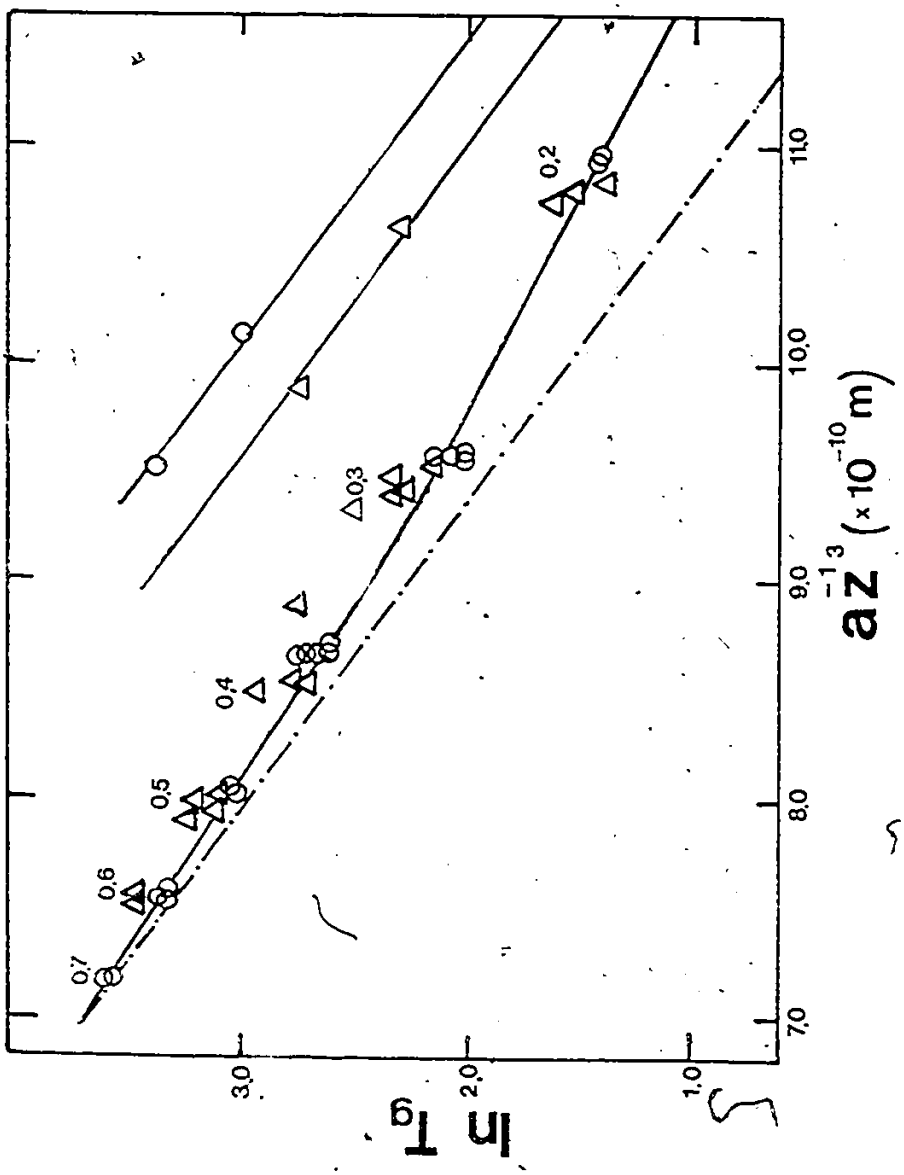

Fig. VIII-15 Plot of ln T_g vs $az^{-1/3}$ of the systems $Cd_{2x}(CuIn)_y Mn_{2z} Te_2$ and $Cd_{2x}(AgIn)_y Mn_{2z} Te_2$. Open triangles is an effective line which represents the values for the section y=0, i.e. $Cd_{1-z} Mn_z Te$.

(dash dotted line) which represents the values for the section y=0 and also for a number of zincblende and hexagonal materials in which the Mn's have random configuration (85S1) (85M1) are shown.

It can be seen in fig.(VIII-15) that for high Mn concentration the values of Ln T_g in the ordered range tend to coincide with those of the line given by the section y=0, while that for low Mn concentration the values of Ln T_g given by the ordered alloys are slightly higher than those of the line representing the section y=0. These results indicate that as the Mn concentration increases the degree of ordering in the ordered field decreases. Hence the factor q is slowly changing and in the region of high Mn concentration is approaching more closely the value $(3/2\pi)^{1/3}$ given by the section y=0.

The fact that the Ln T_g Vs $az^{-1/3}$ is a straight line shows that the exponent α is independent of composition for these random alloys. Also the line for the section y=0 is found to have the same slope as a large number of similar systems such as $Cd_xZn_yMn_zTe$, $Hg_xZn_yMn_zTe$, $Cd_xZn_yMn_zSe$, $(Cd_{1-x}Mn_x)(Se_{1-y}Te_y)$, etc.. This shows that α is independent of anion composition being constant for all of these alloys.

With regard to the chalcopyrite samples, due to the limitations of the present experimental system no measurements could be made on samples with values of $z<0.2$. However it is seen in fig. (VIII-15) that straight lines can be drawn through the two sets of values given by the chalcopyrite samples of each system and that within the experimental error these straight lines are parallel to the effective line $y=0$.

In the case of the present alloys a value of $q\alpha$ can be calculated using the value of given by the section $y=0$. The resulting straight line so obtained is found to be consistent with the experimental data for low concentration of Mn. This is illustrated in fig. (VIII-15) by the solid line drawn in the region $0.3>z>0$. For $z>0.3$ it is seen that the slope of this straight line is slowly changing and that for higher values of z the experimental points tend to coincide with that of the random alloys for these concentrations. Thus it appears probable that the value of obtained for the random alloys applies also for those partially ordered alloys.

Since as shown above the value of α is independent of crystal structure, Mn concentration, configuration of the Mn, configuration of the non-magnetic cations and anion type, it will thus be independent of any other

parameter which is composition dependent such as energy gap and effective mass. One mechanism which has been suggested to explain eq.(VIII-1) is that of Bloembergen-Rowland (55B1). However in that case the analysis would indicate α should be a function of energy gap E_o and the effective mass. Hence this mechanism does not appear to be the one involved here.

The ordinate intersection of these straight lines in fig.(VIII-15) can give information about the magnitude of the parameter J_o from eq.(VIII-6). It can be seen in fig.(VIII-15) that the extrapolation of the line representing the ordered alloys for low values of z gives an intercept on the Ln T_g axis of J_o of 0.22eV. The lines corresponding to the chalcopyrite samples give intercepts of J_o of 1.78eV and 2.27eV for the CuIn and AgIn systems respectively, while the pseudobinary section y=0 gives a value of 0.5eV for J_o.

With regard to the variation of the parameter J_o, it appears that for materials in which the configuration of the Mn is at random the parameter J_o may depend on the configuration of the non-magnetic cations. In the case of the chalcopyrite samples, the non-magnetic cations order on two cation sublattices as indicated in chapter II, and the manganese ions are distributed at random on these

sublattices. This configuration of the non-magnetic cations could be the origin of the highest J_o observed in these samples. The high values of T_g given by these chalcopyrite samples are in agreement with recently experimental measurements made on some samples of the section $(AgGa)_{1-z}\ Mn_{2z}\ Te_2$ for low values of z (84L1). It is to be noted that the samples x=0 z=0.3 and x=0 z=0.35 of the CuIn system have slightly higher values than those of the ordered samples. This may indicate that in these samples there still exist some degree of ordering of the non-magnetic cations which was not observed in the X-ray powder photographs for these specimens, i.e. there is a small degree of chalcopyrite ordering.

Also it is of interest to note that the lattice parameter values of the pseudobinary section x=0 of the $Cd_{2x}(AgIn)_y\ Mn_{2z}\ Te_2$ are higher than that of the $Cd_{2x}\ (CuIn)_y\ Mn_{2z}\ Te_2$ system. However the values of T_g given by the section x=0 for the chalcopyrite samples of the AgIn system are the highest. Hence, it appears that there is not a simple correlation between the lattice parameter and the magnitude of the exchange interaction between the Mn ions for these samples.

Turning to the case of the ordered alloys, for low concentration of Mn the value of J_o given by these samples

is the lowest as described above. For the region of high Mn concentration the value of J_o is very close to the one given by the section y=0. This indicates that for samples where the non-magnetic cations are in a random configuration, the value of J_o depends on the configuration of the Mn ions.

It is of interest to compare the effective line given by a least-squares fit to the section y=0, dash-dotted line in fig.(VIII-15), with that shown in figs. (VIII-9) and (VIII-10), where the variation of T_g with z was taken as linear. It is observed that in the composition range of the present results it is not possible within the experimental error to establish which straight line gives the best representation of the experimental data, both fitting equally well. However, the two forms must diverge at low values of z, the $\ln T_g$ Vs $az^{-1/3}$ line can be extrapolated to very low values of z, below the nearest neighbor percolation limit for which no present data are available. However, this relation predicts for the pseudobinary section y=0 a value of T_g of approximately 50mK for z=0.05 which is in reasonably good agreement with the value reported by Novak et. al. (81N1) for that concentration. Also experimental measurements made on samples z=0.15, 0.10 and 0.05 of the pseudobinary section $Cd_{1-z}Mn_z$ Se (81N2), showed these samples to have

values of T_g in the range 750 to 78 mK. Hence, this relation could be the case for very low values of z and the resulting form could be as illustrated in figs. (VIII-9) and (VIII-10). To confirm these values, measurements would have to be performed below 4K and again this is not possible with the present experimental set-up.

The above results suggest that below the nearest neighbor (n.n) percolation limit 0.18, other interactions than the n.n. interaction should be considered. Calculation (66D1)(79G) for f.c.c. lattice have shown that for second nearest neighbors the percolation concentration limit becomes 0.13 while for third nearest neighbors it is 0.06. For values in the range $z>0.2$ nearest neighbor exchange interaction will dominate, the effects of next nearest neighbors and others being much smaller. Thus the linear extrapolation effectively represents the effect of n.n.. For the composition range $z<0.2$, neighbors further than nearest neighbors become relatively more important, thus in this region of low Mn concentration the samples should show at low temperatures a spin-glass behaviour in agreement with the experimental results of Novak et. al. (81N1) (81N2) on sample of the pseudobinary systems $Cd_{1-z}Mn_zTe$, and $Cd_{1-z}Mn_zSe$. This explains the form of the T_g Vs z curve for these concentrations in figs. (VIII-9) and (VIII-10).

VIII-4 SUMMARY AND CONCLUSION

The variation of T_g with a composition variable is typical of these SMSA. The value of the nearest neighbor percolation limit for the present systems is in agreement with earlier studies (66D1). However, contributions from next nearest neighbors and others become important in the region of low Mn concentration, i.e. $z<0.2$.

The exponent α can be considered characteristic of this type of materials and thus it is independent of composition. The slope of the graph Ln T_g Vs $az^{-1/3}$ was found to depend on the Mn configuration in the unit cell of the specific material.

For the random alloys, i.e. samples where the Mn ions are distributed at random, the parameter J_o seems to depend on the configuration of the non-magnetic cations. In the case of the present cubic alloys, for low values of z, J_o would depend on the Mn configuration, and for the highest Mn concentrations it appears that the value of J_o is very close to that of the pseudobinary section y=0 reflecting the disappearance of partial order of the Mn for these regions of high concentration of the Mn ions, this is in agreement with the intensities of the ordering

lines present in the X-ray results. However it would be of interest to make further experimental measurements on the section x=0 at lower temperature, and also to investigate others SMSA such as $Cd_{2x}(AgGa)_y Mn_{2z} Te_2$, $Zn_{2z}(CuIn)_y Mn_{2z} Te_2$ $Zn_{2x}(AgIn)_y Mn_{2z} Te_2$, etc so that experimental data may be compared.

REFERENCES

1945

45N1 Nelson, J. B. and Riley, D. P., Proc. Phys. Soc., 57 , 160, 1945

1946

46B1 Brillouin L., Wave Propagation in Periodic Structures, 2nd ed., 1946

1952

52W1 Welker Z., Naturforsch, 7a , 744, 1952

1954

54R1 Ruderman M. A. and Kittel C., Phy. Rev. 96 , 99, 1954

1955

55B1 Bloembergen and Rowland, Phys. Rev., 97 , 1679, 1955

55D1 Dresselhaus G., Phys. Rev., 100 , 2, 580, 1955

1956

56C1 Cullity B. D., Elemets of X-ray Diffraction, Addison Wesley, 1956

1958

58P1 Phyllips J. C., Phys. Rev., 112 , 685, 1958

1960

60H1 Hopfield J. J., Phys. Chem. Solids 15 , 97, 1960

1962

62C1 Chernyavsky, Fizika, Leningrad, 10 , 1962

1963

63K1 Koster G. F, Dimmock J. O., Wheeler R. G. and Stats H.,

"Properties of the thirty-two point groups"., M.I.T. Press, 416-418, 1963

63Y1 Yafet Y., Sol. Stat. Phys., Edited by F. Seitz and D. Turnbull, Academic Press, N.Y 14 , 1, 1963

1964

64B1 Bonfiglioli G. and Brovetto P., Appl. Opt., 3 , 12,1417, 1964

64S1 Schafer H., Chemical Transport Reaction, Academic Press, N.Y., 1964

1966

66D1 Domb C. and Dalton N. W., Proc. Phy. Rev. 89 , 1679, 1966

66W1 Woolley J. C. and Williams E. W., Elec. Soc., 113 9,849,1966

1967

67J1 Johnson J., Semiconductors and Semimetals, Optical Properties of III-V compounds., 3 , 154, 1967

67S1 Song K. S., Ph. D. thesis, University of strasbourg, France, 1967

1968

68G1 Greenaway D. L. and Harbeke G., Optical Properties of semiconductors, Pergamon Prees, N.Y., 1968.

1969

69C1 Cardona M., Modulation Spectroscopy, Academic Press, N.Y, 1969

1971

71P1 Poplavnoi A. S. and Polygalov Y.I., Inorg. Mater.,

USSR, Z , 1527; Z , 1531, 1971

71R1 Rowe J. E. and Shay J. L., Phys. Rev., B3 , 451, 1971

1973

73L1 Lucino M. J. and Vesely C. J., Appl. Phys. Lett., 23 , 60, 1973

73P1 Parkes J. Tomlimson R. D. and Hampshire M. J., Sol. St. Electron, 16 , 773, 1973 .

1974

74K1 Kono S. and Okusawa J., Phys. Soc. Jap., 37 1301, 1974

74L1 Lax M., Symmetry Principles in Solid State and Molecular Physics, Wiley, N.Y., 1974

74S1 Shay J. L. and Wernick J. H., Ternary Chalcopyrite Semiconductors: Growth, Electronic Properties and Aplications, Pergamon, Oxford, 1974

1975

75R1 Robbins M. Phillip J. C. and Lambrecht V. G. Jr, J. Sol. State Chem. 15 , 167, 1975

75W1 Wenger L. E. and Keeson P. H., Phys. Rev. B, 13 , 4053, 1975

75W2 Wenger L. E. and Keeson P. H., Phys. Rev. B, 11 , 3497, 1975

1976

76K1 Kittel C., Introduction to Solid State Physics, 5th Ed., Wiley, N.Y., 1976

1977

77A1 Al-Alamy F. A. and Balchin A. A., J. Crys. Growth., 39

275-286, 1977

77Y1 Yamamoto N. Horinaka H. K. Okada K. and Miyauchi T., Jpn. J. Appl. Phys., 16, 1817, 1977

1978

78G1 Gaj J. A., Galazka R. R. and Nowrocki M., Sol. St. comm., 25 , 193, 1978

78W1 William C. K., Glisson T. H. Hauser J. R. and Littlejohn J., Elec. Mater., 7, 639, 1978

1979

79B1 Bastard G. and Lewiner C., Phys. Rev., B, 20 , 425, 1979

79C1 Chapman G. H., Shewchun J., Loferski J. J., Garside B. K. and Beaulieu R., Appl. Phys. Lett., 34 735, 1979

79G1 Ginter J. Kossut J. and Sewierkowski, Phys. Stat. Sol., 96, 1, 735, 1979

79G2 Galazka R. R., Physics of Semiconductors, Edite by B. L. Willson (Institute of Physics), Bristol, 1979

79Y1 Yamamoto N., Horikana K. and Miyauchi T., Jpn. J. of Phys., 18 , 255, 1979

79M1 Manoogian A. and Leclerc A. K., Can. J. Phys. 57 , 10 1979; Phys. Stat. Sol. b, 92 , K23, 1979

1980

80G1 Galazka R. R., Nagata S. and Keeson P. H., Phys. Rev. B, 22 , 3344, 1980

80G2 Goodchild G., Woolley J. C. and Gonzalez J., Jap. J. Appl. Phys., 19 , 123-128, 1980

80J1 Gaj J. A., Proc. 15th int. conf. Physics of Semiconductors, Tokyo, 1980

1981

81E1 Escorne M., Mauger A., Triboulet and Tholence J. L., Physica 107B, 309, 1981

81N1 Novak M. A., Oseroff S. and Symko O. G., Physica 107 B, 313, 1981

81N2 Novak M. A., Symko O. G., Zheng D. J. and Oseroff S., to be published.

1982

82F1 Furdina J. K., J. Appl. Phys. 53, 11, 1982

82F2 Ford P. J., Temp. Phys., 23, 141, 1982

82G1 Goodchild G., Ph. D. Thesis, University of Ottawa

82L1 Lopez-Rivera A. S., Goodchild G., Hughes O., Woolley J. C. and Pamplin B. R., Can. J. Phys., 60, 1, 10, 1982

82O1 Oseroff S. B., Phys. Rev. B, 25, 6584, 1982

82O2 Oelhafen P., Vecchi M. P. Freeouf J. L. and Moruzzi V. L., Sol. St. Comm., 44, 12, 1547-1550, 1982

1983

83A1 Avon J., Yoodee K. and Woolley J. C., Il Nuevo Cimento, 2D, 6,1859, 1983

83B1 Brun Del Re R., Donofrio T., Avon J., Majid J. and Woolley J. C., Il Nuevo Cimento, 2D, 6, 1911, 1983

1984

84A1 Avon J. E., Yoodee K. and Woolley J. C., J. Appl. Phys., 55, 524, 1984

84K1 Yoodee K., Woolley J. C. and Sa-yakanit V., Phys. Rev.

B, 30 ,10, 5904, 1984

84M1 Manoogian A. and Woolley J. C., to be published

84Q1 Quintero M., Woolley J. C., Lamarche G., Manoogian A. and Wasim S. M., to be published

84W1 Woolley J. C., to be published

1985

85D1 Donofrio Tom, Ph. D. Thesis, U. O.

85K1 Yoodee K., Ph. D. Thesis, U. O.